SPATIAL SAMPLING AND FILTERING IN NEAR-FIELD MEASUREMENTS
JOY, EDWARD BENNETT
ProQuest Dissertations and Theses; 1970; ProQuest Dissertations & Theses Global

71-13,780

JOY, Edward Bennett, 1941-
SPATIAL SAMPLING AND FILTERING IN NEAR-FIELD MEASUREMENTS.

Georgia Institute of Technology, Ph.D., 1970
Engineering, electrical

University Microfilms, A XEROX Company, Ann Arbor, Michigan

Reproduced with permission of the copyright owner. Further reproduction prohibited without permission.

SPATIAL SAMPLING AND FILTERING IN NEAR-FIELD MEASUREMENTS

A THESIS

Presented to

The Faculty of the Graduate Division

by

Edward Bennett Joy

In Partial Fulfillment

of the Requirements for the Degree

Doctor of Philosophy

in the School of Electrical Engineering

Georgia Institute of Technology

November, 1970

Reproduced with permission of the copyright owner. Further reproduction prohibited without permission.

SPATIAL SAMPLING AND FILTERING

IN NEAR-FIELD MEASUREMENTS

APPROVED:

Demetrius T. Paris
Chairman

Ronald W. Larson

A. C. Johnson

Anthony W. Boord

Date approved by Chairman 11/4/70

Reproduced with permission of the copyright owner. Further reproduction prohibited without permission.

In presenting the dissertation as a partial fulfillment of the requirements for an advanced degree from the Georgia Institute of Technology, I agree that the Library of the Institute shall make it available for inspection and circulation in accordance with its regulations governing materials of this type. I agree that permission to copy from, or to publish from, this dissertation may be granted by the professor under whose direction it was written, or, in his absence, by the Dean of the Graduate Division when such copying or publication is solely for scholarly purposes and does not involve potential financial gain. It is understood that any copying from, or publication of, this dissertation which involves potential financial gain will not be allowed without written permission.

Edward B. Joy

7/25/68

Reproduced with permission of the copyright owner. Further reproduction prohibited without permission.

AGKNOWLEDGMENTS

Dr. Demetrius T. Paris, my advisor and Director of the School of Electrical Engineering, suggested the problem, provided guidance and encouragement throughout the research, carefully reviewed and criticized the manuscript, helped provide financial support through a Scientific Atlanta Research Grant and an appointment as a Graduate Teaching Assistant, and provided liaison with the Georgia Tech Engineering Experiment Station and Scientific Atlanta, Inc.

Dr. Benjamin J. Dasher, past Director of the School of Electrical Engineering, provided me with financial support through the Schlumberger Fellowship and a NASA Traineeship.

Mr. J. Searcy Hollis, principal engineer of Scientific Atlanta, Inc., provided guidance during the experimental phase of the research and provided much of the experimental apparatus required to carry out the electromagnetic field measurements.

Dr. Richard C. Johnson, Chief of the Electronics Division of the Georgia Tech Engineering Experiment Station and member of my reading committee, provided use of the near-field measurement apparatus and far-field range.

Dr. Aubrey M. Bush served as a member of my reading committee and provided in-depth understanding of Fourier transform theory.

Dr. Ronal W. Larson served as a member of my reading committee and provided many useful discussions on scattering theory.

Dr. David M. Kerns, Scientific Consultant to the Radio Standards

Reproduced with permission of the copyright owner. Further reproduction prohibited without permission.

Engineering Division of the National Bureau of Standards in Boulder, Colorado, contributed significantly to my understanding of scattering matrix theory and the theory of plane wave expansions.

Patricia, my wife, typed the many rough drafts of the manuscript and shared with me the life of a graduate student.

To these people, I express deep appreciation and thanks.

Reproduced with permission of the copyright owner. Further reproduction prohibited without permission.

TABLE OF CONTENTS

Page

ACKNOWLEDGMENTS ii

LIST OF TABLES vi

LIST OF ILLUSTRATIONS vii

SUMMARY x

Chapter

I. INTRODUCTION 1

Brief History of Far-field Determination from Near-field Measurements
Need for a Sample Spacing Criterion and a Data Minimization Technique
Purpose of this Research

II. ANALYTICAL BASIS 8

Plane Wave Representation of Electromagnetic Fields
Sample Spacing Criterion
Near-field Data Minimization
Scattering Approach to the Two Antenna Measurement System
Far-field Measurement Equations
On-axis Polarization Ratio Measurement Equation

III. INSTRUMENTATION AND EQUIPMENT 55

Antennas and Probes
Polarization Measurement System
Probe Measurement System
Near-field Measurement System
Far-field Measurement System

IV. MEASUREMENTS AND FAR-FIELD CALCULATION 75

Polarization Ratio Measurement
Probe Measurement
Near-field Measurement
Far-field Measurement
Far-field Calculation

V. RESULTS 111

Reproduced with permission of the copyright owner. Further reproduction prohibited without permission.

TABLE OF CONTENTS (Continued)

Page

VI. CONCLUSIONS AND RECOMMENDATIONS 119

BIBLIOGRAPHY 121

VITA 124

Reproduced with permission of the copyright owner. Further reproduction prohibited without permission.

LIST OF TABLES

Table Page

1. Polarization Ratio Measurement Data. 79

2. Calculated Polarization Ratio. 79

Reproduced with permission of the copyright owner. Further reproduction prohibited without permission.

LIST OF ILLUSTRATIONS

Figure		Page
1.	Reference Coordinate System.	12
2.	Wavenumber Space	17
3.	Sample Spacing as a Function of Attenuation Level and Distance from Antenna, in Wavelengths.	21
4.	Blackman Low-pass Filter Characteristics	29
5.	Conical Far-field Sector	34
6.	Number of Post-filter Samples Required to Calculate the Conical Far-field Pattern of the First Example	37
7.	Principal Plane Sector	36
8.	Number of Post-filter Samples Required to Calculate the Principal Plane Far-field Sector of the Second Example	39
9.	Two Antenna Measurement System Schematic	41
10.	Far-Field Measurement System Schematic	46
11.	Two Antenna, On-axis, Far-field Measurement System Schematic .	50
12.	Rotated Two Antenna, On-axis, Far-field Measurement System Schematic	50
13.	Test Antennas and Probes	57
14.	Schematic Diagram of the Polarization Ratio Measurement System	59
15.	Antenna Mounts Used in the Polarization Ratio Measurement System	61
16.	Schematic Diagram of the Probe Far-field Measurement System	63
17.	Probe Far-field Measurement System	64
18.	Schematic Diagram of the Near-field Measurement System	68
19.	Near-field Measurement System	69
20.	Far-field Receiving Equipment Room and Antenna Positioner. . .	72

Reproduced with permission of the copyright owner. Further reproduction prohibited without permission.

LIST OF ILLUSTRATIONS (Continued)

Figure		Page
21.	Schematic Diagram of the Far-field Measurement System. . . .	73
22.	Measured Far-field Amplitude and Phase Patterns of the Open-ended Waveguide Probe.	84
23.	Measured Far-field Amplitude and Phase Patterns of the Small Horn Probe	85
24.	Measured Far-field Amplitude and Phase Patterns of the Large Horn Probe.	86
25.	Z-position Error of the Near-field Measurement Plane	88
26.	Near-field Measurement Area.	89
27.	X-position Error Versus Normalized Time for the XY-motion Unit	92
28.	Near-field Amplitude and Phase Patterns of the Large Test Antenna as Measured with the Open-ended Waveguide Probe.	93
29.	Near-field Amplitude and Phase Patterns of the Large Test Antenna as Measured with the Small Horn Probe.	94
30.	Near-field Amplitude and Phase Patterns of the Large Test Antenna as Measured with the Large Horn Probe.	95
31.	Near-field Amplitude and Phase Patterns of the Small Test Antenna as Measured with the Open-ended Waveguide Probe.	96
32.	Near-field Amplitude and Phase Patterns of the Small Test Antenna as Measured with the Small Horn Probe.	97
33.	Near-field Amplitude and Phase Patterns of the Small Test Antenna as Measured with the Large Horn Probe.	98
34.	Measured Far-field Amplitude Patterns of the Large Test Antenna.	101
35.	Measured Far-field Amplitude Patterns of the Small Test Antenna.	102

Reproduced with permission of the copyright owner. Further reproduction prohibited without permission.

LIST OF ILLUSTRATIONS (Continued)

Figure		Page
36.	Block Diagram of the Far-field Computation Process	104
37.	Calculated Far-field Amplitude Patterns of the Large Test Antenna.	107
38.	Calculated Far-field Amplitude Patterns of the Small Test Antenna.	108
39.	Calculated Two-dimensional Far-field Amplitude Patterns. . . .	109
40.	Principal Plane Pattern of the Large Test Antenna, Calculated from Near-field Data taken with each of the Three Near-field Probes.	110
41.	Calculated Far-field Patterns of the Large Antenna for Near-field Sample Spacings of $\lambda/3$, λ, and 2λ	112
42.	Calculated Far-field Patterns of the Small Antenna for Near-field Sample Spacings of $\lambda/3$, λ, and 2λ	113
43.	Far-field Patterns of the Large Test Antenna Calculated with 16384, 60, and 20 Post-filter Samples.	115
44.	Far-field Patterns of the Small Test Antenna Calculated with 16384, 60, and 20 Post-filter Samples.	116
45.	Comparison of Calculated and Measured Far-field Patterns of the Large Test Antenna	117
46.	Comparison of Calculated and Measured Far-field Patterns of the Small Test Antenna	118

Reproduced with permission of the copyright owner. Further reproduction prohibited without permission.

SUMMARY

It is well-known that the far-field of an arbitrary antenna may be calculated from near-field measurements. This approach to far-field determination is not new, but two important questions remain unanswered:

1. How far apart should the near-field sample points be spaced?
2. How can the amount of near-field data be reduced?

To answer these questions, certain well-established communication techniques, centered around Fourier transform theory, are applied to the near-field measurement problem in this work.

Another well-known technique used in this investigation is the expansion of an arbitrary electromagnetic field as a continuum of plane waves. If an electromagnetic field is specified over a planar surface, its amplitude is related to its plane wave wavenumber spectrum through a Fourier transform. Additionally, on a sphere of infinite radius (i.e., the far field), the same electromagnetic field is directly related to its wavenumber spectrum, but only for wavenumbers whose magnitude is less than $2\pi/\lambda$.

Using a scattering matrix approach, D. M. Kerns, Scientific Consultant to the Radio Standards Engineering Division of the National Bureau of Standards, has carefully analyzed the two antenna measurement system, and has concluded that the true wavenumber spectrum of the electromagnetic field may be found from the measured planar field if the complete

Reproduced with permission of the copyright owner. Further reproduction prohibited without permission.

electromagnetic characterization of the measuring probe is known. Then, if the electromagnetic field is measured on a plane located a finite distance from an antenna, Fourier transform techniques may be used to analyze the far-field calculation problem.

Plane waves, with wavenumbers greater than $2\pi/\lambda$, are attenuated with increasing wavenumber and with distance from the measurement plane. Once some arbitrary attenuation level and a distance from the antenna are selected, the sampling theorem from Fourier analysis can be used to choose the required sample spacing in the near field, sufficiently small to include all wavenumbers above the selected attenuation level. The sample spacing approaches an upper bound of $\lambda/2$ at infinite separation from the antenna.

Additional wavenumber limiting may be artificially effected through the use of low-pass spatial filtering of the measured near-field data. As the wavenumber limit of the low-pass filter decreases, the required post-filter sample spacing increases which, in effect, reduces the number of samples. The resulting wavenumber-limited data is found to contain all information necessary to calculate the far-field pattern of the antenna in well-defined angular sectors centered about the polar axis (the axis which is perpendicular to the measurement plane and passes through the origin of the selected system of coordinates). The angular size of these sectors is found to depend on the wavenumber limits of the low-pass filter. The far field over other sectors of interest can be found by applying wavenumber shifting (similar to the communication theory technique of frequency shifting) of the near-field data followed by the same low-pass filtering process. The number of post-filter samples

Reproduced with permission of the copyright owner. Further reproduction prohibited without permission.

needed to calculate a given sector of the far field can be predicted, and is shown to decrease monotonically with decreasing size of the sector. Even greater data minimization is possible for one-dimensional slices of the far-field pattern.

This technique has been verified experimentally as follows: First, the complex on-axis polarization ratio of a far-field probe antenna was determined through a new measurement technique from a set of three on-axis polarization ratio measurements made with two other antennas. Second, the scattering properties of three probe antennas were determined by measuring two orthogonal components of their far-field patterns in both phase and amplitude. Third, the near fields of two X-band antennas were measured using the chosen probe. The measurement apparatus consists of an automated, line-scanning mechanical positioner capable of scanning a 100" by 100" planar surface with an accuracy of five thousandths of an inch. A newly developed phase/amplitude receiver was used to measure two orthogonal components of the near field in phase and amplitude. This information was read into a digital computer for low-pass filtering, wavenumber shifting, probe correction, and far-field calculation. Fourth, the calculated far fields of the two X-band antennas were compared to far-field patterns measured on a standard antenna range.

Calculated and measured far-field patterns are shown to agree within the measurement accuracy of the far-field range.

Reproduced with permission of the copyright owner. Further reproduction prohibited without permission.

CHAPTER I

INTRODUCTION

The determination of the far-field radiation pattern of an antenna is a problem rich in history (1), both as a direct far-field measurement problem and as an electromagnetic boundary value problem.

Direct far-field measurement is well-suited for electrically small antennas, as conventional size antenna ranges can be constructed to yield accurate results. For electrically large antennas, however, the required size of the far-field antenna range becomes prohibitively large (2). Celestial bodies (3), satellites (4) and aircraft (5) have been used as sources of electromagnetic radiation to extend the size of the far-field range with only limited success.

Another method of far-field determination is the solution of Maxwell's equations subject to the boundary conditions imposed by the antenna. Solution of the electromagnetic boundary value problem is possible in closed form for only the geometrically simplest of antennas. As the shape of the antenna is complicated with feed supports, mounting structure, mechanical imprecisions and irregular surfaces, many approximations are introduced to simplify the resulting numerical problem. At best the solution is a first approximation to the true far field of the antenna.

Recently a hybrid approach to far-field determination has been attracting the attention of those faced with far-field determination of electrically large and often complicated antennas. The hybrid approach

Reproduced with permission of the copyright owner. Further reproduction prohibited without permission.

includes both measurement and calculation. The electromagnetic field near an antenna is measured on a specified surface enclosing the antenna and the far field is calculated from the measured near-field data. The hybrid approach has the dual advantages of eliminating the need for a large far-field range and of being applicable to arbitrary antennas.

Brief History of Far-Field Determination from Near-Field Measurements

Early work in near-field measurements attempted to directly implement Huygens' principle of secondary spherical waves (6-9). Use of Huygens' principle required measurement of both the tangential electric and magnetic fields on a near-field surface. As the magnetic field was difficult to measure with accuracy, it was assumed to be directly proportional to the measured electric field as in a plane wave.

Huygens' principle also required knowledge of the direction of propagation of the field at each point of the measurement surface. As the unknown direction of propagation could not be determined directly, it was assumed to be normal to the measurement surface.

The near-field measuring probe was assumed to be ideal, measuring exactly the undistorted tangential electric field. The near-field measurement spacings were chosen to obtain smooth near-field measurement graphs on a trial and error basis. The amount of near-field data was usually very large and almost no data minimization was used.

Experimentally, early work in near-field measurement was directed toward development of an ideal near-field measuring probe. Richmond and Tice (10) stated that an ideal probe should possess the following four qualities:

Reproduced with permission of the copyright owner. Further reproduction prohibited without permission.

(1) The probe should not distort the field being measured.

(2) The probe should be small enough to essentially measure the field at a point.

(3) The probe should be linearly polarized.

(4) The probe should provide the measuring equipment with an adequate signal.

Two general classes of probes were developed to measure the tangential electric field. The first class provided a direct sample of the field. The second class provided an indirect sample of the field by measuring the backscattering from a small probe located on the measurement surface.

Whiteside and King (11), Borts (12), and Woonton (13) worked with direct measurement probes and developed small dipole probes which closely approximated the ideal probe at low frequencies. Richmond and Tice (10) developed small dielectrically loaded waveguide probes which were useful in the microwave region and provided a good estimate of the field without probe correction.

Justice and Rumsey (14), Harrington (15) and Plonsey (16) developed near-field scatterers and scattering systems which measured the near field indirectly. The significance of this method of measurement is that the probe size can be greatly reduced, reducing the distortion of the field due to the presence of the probe.

In all of these early near-field measurement systems, measurement of the relative phase of the electromagnetic field was time-consuming and usually inaccurate.

Although sophisticated probes and measuring systems were developed,

Reproduced with permission of the copyright owner. Further reproduction prohibited without permission.

many unjustifiable assumptions concerning the properties of the field being measured remained, until Booker and Clemmow (18) reformulated the far-field deterimination problem in terms of plane wave expansions. They showed that only two components of the tangential electric field were required to determine the complete far field and that knowledge of the direction of propagation at each near-field measurement point was not required.

Brown (19) and Jull (20-22), working with line sources and using cylindrical wave expansions of the electromagnetic fields, also showed that only two components of the tangential electric field needed to be measured and that the direction of propagation of the measured field was not needed. They also made an important first step in correcting the calculated far-field patterns for the effect of the measuring probe. Sample spacing and data minimization, however, were not treated.

Kerns (23) and Dayhoff (24), working with arbitrary antennas, and using plane wave expansions of the electromagnetic fields, characterized the two antenna measurement system by means of a scattering matrix of plane waves. For the special case of no multiple reflection between the two antennas, they were able to correct the calculated far-field patterns of an arbitrary antenna for the effects of an arbitrary, near-field measuring antenna, if the scattering parameters of the measuring antenna were known a priori. They also carried out the near-field measurements and far-field calculations and demonstrated that sample spacings as large as one wavelength could be used in certain cases, but reached no general conclusions concerning sample spacing for an arbitrary antenna. Some of their measured near-field data was eliminated by using statistical significance tests, but the amount of data minimization was minimal.

Reproduced with permission of the copyright owner. Further reproduction prohibited without permission.

Near-field measurements can now be performed quickly and easily through the use of newly developed phase/amplitude receivers.

Need for a Sample Spacing Criterion and a Data Minimization Technique

Through the years the hybrid approach to far-field determination has become more exact with the elimination of many unjustifiable assumptions and has become more practical with the advent of modern phase and amplitude measurement equipment. Two important questions concerning the validity and practicality of the hybrid approach, however, remain unanswered:

1. How far apart should the near-field sample points be spaced?
2. How can the amount of near-field data be reduced?

The trial and error approach to sample spacing of the past required many redundant measurements and calculations to iteratively arrive at a suitable sample spacing for a given antenna. The iterative process must then be repeated for each new antenna. Large sample spacings are preferable as smaller amounts of measurements and data are associated with the larger sample spacings for a given size antenna.

Thus, an a priori sample spacing criterion is needed which will specify the largest sample spacing permissible for a given antenna and for a given distance from the antenna to the near-field plane of measurement.

Near-field measurement presents a unique data collection and computation problem. As each point of the far-field radiation pattern

Reproduced with permission of the copyright owner. Further reproduction prohibited without permission.

depends on the entire near-field data, all the measured data must be stored for computation, usually in the memory of a digital computer. The storage capacity of even the largest digital computer is easily exceeded with the data storage requirement of electrically large antennas.

Thus, a data minimization technique is needed to reduce the amount of near-field data required to calculate a given angular sector of a far-field pattern. Data minimization may occur at the near-field measuring site or internal to the computer as a series operation which processes the data as it is read into the computer.

Through the use of data minimization, the requirement for a digital computer can often be eliminated as in the determination of the principal plane far-field patterns.

Purpose of this Research

The purpose of this research is to further develop the near-field measurement technique for determination of antenna far-field patterns. Specifically, this research has a threefold objective:

First, to establish a sample spacing criterion for near-field measurements made on a planar surface near an arbitrary antenna. This criterion should specify the spacings between near-field samples and the location of each sample within the measurement plane. The planar surface is preferred because a great reduction in the far-field computation process occurs for planar near-field surfaces. For a planar, near-field surface the far field can be related to the near field through a Fourier transform (25), allowing use of the Fast Fourier transform technique (26) to greatly reduce computer calculation time.

Reproduced with permission of the copyright owner. Further reproduction prohibited without permission.

Second, to develop a near-field data minimization technique to significantly reduce the amount of data needed to calculate a given angular sector of the far-field radiation pattern.

Third, to experimentally demonstrate the feasibility and practicality of far-field determination from near-field measurements. Use of the sample spacing criterion and the data minimization technique are included as part of this investigation.

Reproduced with permission of the copyright owner. Further reproduction prohibited without permission.

CHAPTER II

ANALYTICAL BASIS

A great amount of insight may be gained about the nature of an electromagnetic field on a plane near a radiating structure, if it is decomposed into a continuum of plane waves. Specification of the complex amplitude of the continuum of plane waves takes the form of a two-dimensional Fourier transform of the complex two-dimensional electromagnetic field. As the plane wave amplitude spectrum so obtained is directly related to the far-field pattern of the antenna, a Fourier transform relationship is seen to exist between the two-dimensional near field and the radiated far field. Thus the well known results of Fourier analysis (27,28) may be applied to the problem of far-field determination from near-field measurements. The familiar one-dimensional time and frequency Fourier transform domains of linear system theory are replaced with the two-dimensional space and wavenumber domains of electromagnetic theory.

The first application of the results of Fourier Analysis is used to arrive at a sample spacing criterion for two-dimensional near-field measurements. Cast in terms of the domains of electromagnetic theory, the sampling theorem of Fourier analysis (29) states that a two-dimensional electromagnetic field, whose plane wave wavenumber spectrum has finite dimensions in the wavenumber domain, may be sampled at equally spaced intervals in each of the two spatial dimensions. The size of the two spatial intervals is determined from the magnitude of the two maximum wavenumber dimensions of the wavenumber spectrum. For large wavenumbers

Reproduced with permission of the copyright owner. Further reproduction prohibited without permission.

the amplitude of the wavenumber spectrum decays exponentially as the distance between the source of the electromagnetic field and the near-field measurement plane is increased. Thus, as the near-field measurement plane is moved away from the antenna, the wavenumber spectrum of the two-dimensional electromagnetic near field becomes essentially wavenumber limited and the Fourier sampling theorem may be applied.

In addition to the wavenumber limiting process observed with increasing distance from the antenna, another result of Fourier analysis may be applied to further limit the wavenumber spectrum of the measured near field. As the spatial sampling intervals are inversely proportional to the wavenumber limits of the wavenumber spectrum, decreasing the wavenumber limits increases the sampling intervals; this process, in effect, decreases the amount of near-field data. Familiar low-pass filtering (28) used, for example, in circuit theory to limit the frequency spectrum of a time signal, can be used in the electromagnetic domains as well. In the electromagnetic domains a two-dimensional, low-pass filter can be used to limit the wavenumber spectrum of a two-dimensional electromagnetic field. The electromagnetic field is first sampled in accordance with the sampling criterion resulting in a two-dimensional array of measured values. The array of measured values is then low-pass filtered and re-sampled in accordance with the sampling theorem; however, in this case, the wavenumber limits of the measured data have been reduced by the low-pass filter, increasing the post filter sample spacings. The result is a smaller array of measured near-field data. As the far-field pattern is directly proportional to the wavenumber spectrum, wavenumber limiting the wavenumber spectrum is equivalent to limiting the far-field

Reproduced with permission of the copyright owner. Further reproduction prohibited without permission.

pattern. Thus, great reductions in measured near-field data are possible when small regions of the far-field pattern are to be determined. Principal plane far-field patterns are typical of small regions of the complete far-field pattern as they are equivalent to a one-dimensional slice of the two-dimensional wavenumber spectrum.

To accurately determine the far-field radiation pattern from near-field measurements, the effect of the presence of the near-field probe must be understood and taken into account. Using plane wave expansions of the electromagnetic field, Kerns (23) has shown that the true wavenumber spectrum of an antenna's two-dimensional near-field may be found from near-field measurements if the wavenumber spectrum of the near-field probe is known. Thus, the first step in the measurement procedure is the determination of the wavenumber spectrum of the near-field probe. As the near-field probe is designed to be electrically small, direct measurement of its far field is easily accomplished. The wavenumber spectrum of the probe is determined from the measured complex far-field pattern. In this connection it should be noted that the complex, on-axis polarization ratio of the far-field measuring antenna must be known a priori to correct the measured far-field patterns of the near-field probes.

Having determined the complex polarization ratio of the far-field measuring antenna, the far field of the near-field probe may be measured and its wavenumber spectrum determined. The two-dimensional near field of an arbitrary antenna may then be measured with the near-field probe and its true wavenumber spectrum determined. The end result, the far-field pattern of the arbitrary antenna, may be readily determined from the corrected wavenumber spectrum of the measured near-field data.

Reproduced with permission of the copyright owner. Further reproduction prohibited without permission.

Plane Wave Representation of Electromagnetic Fields

It is well known that an electromagnetic field may be expanded as an infinite sum of plane waves (25). The electric field of each of the plane waves has the form

$$\vec{E}(x,y,z,t) = \vec{A}(\vec{k})\, e^{j(\omega t - \vec{k}\cdot\vec{r})} \tag{2-1}$$

where ω is the angular frequency, $\vec{k}$ specifies the wavenumber, and $\vec{r}$ is the radius vector from the origin of the reference coordinate system shown in Figure 1. The vector $\vec{k}$ may be written in rectangular coordinates as

$$\vec{k} = k_x\vec{a}_x + k_y\vec{a}_y + k_z\vec{a}_z \tag{2-2}$$

The electric field of each plane wave must satisfy the wave equation (25)

$$\nabla^2\vec{E}(x,y,z,t) - \left(\frac{2\pi}{\lambda}\right)^2 \vec{E}(x,y,z,t) = 0 \tag{2-3}$$

where λ is the free space wavelength. Substituting the plane wave expression, Equation (2-1), into the wave equation, Equation (2-3), results in a restriction on the magnitude of the vector wavenumber $\vec{k}$

$$k_x^2 + k_y^2 + k_z^2 = \left(\frac{2\pi}{\lambda}\right)^2 = k_o^2 \tag{2-4}$$

Thus, in an unbounded medium, any two of the three wavenumber rectangular components may be chosen independently to specify the direction of propagation for a plane wave.

Reproduced with permission of the copyright owner. Further reproduction prohibited without permission.

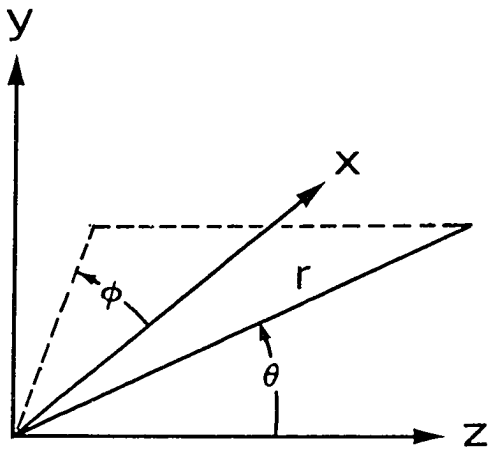

Figure 1. Reference Coordinate System

It is often convenient to write the rectangular components of the vector wavenumber $\vec{k}$, with magnitude k_o, in terms of the spherical angles θ and Φ of Figure 1 as

$$k_x = k_o \sin\theta \cos\Phi \tag{2-5}$$

$$k_y = k_o \sin\theta \sin\Phi \tag{2-6}$$

$$k_z = k_o \cos\theta \tag{2-7}$$

Then, obviously, Equation (2-4) is satisfied automatically.

In general, the complex vector $\vec{A}$ is a function of the direction of propagation $\vec{k}$. If the direction of propagation is known, only two of the three spatial vector components of $\vec{A}$ are needed to specify its spatial orientation as the third component may be found from the plane wave condition (25)

Reproduced with permission of the copyright owner. Further reproduction prohibited without permission.

$$\vec{E} \cdot \vec{k} = 0 \qquad (2\text{-}8)$$

With the choice of k_x and k_y to specify the direction of propagation, and the x and y vector components to specify the spatial orientation of the plane wave electric field, a shorthand notation is adopted for the complex vector amplitude of a plane wave:

$$\bar{A}(k_x, k_y)$$

Here the bar above the letter A represents the transverse (x and y) vector components.

The amplitude of the continuum of plane waves which specify the transverse components of an electric field is given at any point on a plane by the well known relation (29)

$$\bar{A}(k_x, k_y) = \frac{1}{2\pi} \int_{-\infty}^{\infty} \int_{-\infty}^{\infty} \bar{E}(x,y,0)\, e^{-j(k_x x + k_y y)}\, dxdy \qquad (2\text{-}9)$$

where the $z = 0$ plane has been chosen without loss of generality and the time dependence of $\vec{E}$ has been dropped. Equation (2-9) is recognized as a two-dimensional Fourier transform of the transverse components of the two-dimensional electric field. Thus the inverse Fourier relationship reconstructs the electric field from its complex plane wave amplitude spectrum and is given by

$$\bar{E}(x,y,0) = \frac{1}{2\pi} \int_{-\infty}^{\infty} \int_{-\infty}^{\infty} \bar{A}(k_x, k_y)\, e^{j(k_x x + k_y y)}\, dk_x dk_y \qquad (2\text{-}10)$$

Reproduced with permission of the copyright owner. Further reproduction prohibited without permission.

The transverse electric field may also be reconstructed at any value of (x,y,z) in terms of the plane wave amplitude spectrum specified at the $z = 0$ plane as (30)

$$\bar{E}(x,y,z) = \frac{1}{2\pi}\int_{-\infty}^{\infty}\int_{-\infty}^{\infty} \bar{A}(k_x,k_y)\, e^{j(k_x x + k_y y + \sqrt{k_o^2 - k_x^2 - k_y^2}\, z)}\, dk_x dk_y \tag{2-11}$$

which in essence represents a superposition of simpler waves of the form of Equation (2-1). In general, this integral is difficult to evaluate; however, in the limit as the radius approaches infinity, the stationary phase method of integration (31) may be used to evaluate the integral. In this application of the method of stationary phase the equation is transformed from rectangular (x,y,z) coordinates to sperhical (r,θ,Φ) coordinates and the rectangular wavenumber coordinates (k_x,k_y) are given in terms of the spherical angles (θ,Φ). The transverse electric far field is then shown (31) to be

$$\bar{E}(r,\theta,\Phi) = \frac{jk_o \cos\theta\, e^{-j\vec{k}\cdot\vec{r}}}{r}\, \bar{A}(k_o \sin\theta\cos\Phi, k_o \sin\theta \sin\Phi)$$

$$\text{for } k_x^2 + k_y^2 \leqq k_o^2 \tag{2-12}$$

$$= 0 \qquad \text{elsewhere.}$$

The restriction $(k_x)^2 + (k_y)^2 \leqq (k_o)^2$ corresponds to all the real angles (θ,Φ) of propagation. Other wavenumbers (k_x,k_y) correspond to complex angles of propagation and to imaginary values of k_z. Plane waves with imaginary k_z attenuate as they travel in the z-direction and

Reproduced with permission of the copyright owner. Further reproduction prohibited without permission.

are called evanescent waves. The x and y components of the electric field at infinite radius (i.e., the far field) therefore contain no evanescent waves and are directly related to the Fourier transform of the transverse components of the electric field at z = 0.

Having found the transverse components of the electric far field, the z component is found from Equation (2-8) as

$$E_z = \frac{-1}{k_z}(k_x E_x + k_y E_y) \tag{2-13}$$

The magnetic field associated with the electric field of a plane wave is given by

$$\vec{H} = \frac{\vec{k} \cdot \vec{E}}{\eta} \tag{2-14}$$

where

$$\eta = \sqrt{\mu/\epsilon} \tag{2-15}$$

is the characteristic impedance of a non-conducting region, with dielectric constant ϵ and permeability μ. From Equation (2-14) the three components of the magnetic field may be found as

$$H_x = \frac{-1}{\omega\mu k_z}\left[k_x k_y E_x + (k_x^2 + k_y^2) E_y\right] \tag{2-16}$$

$$H_y = \frac{1}{\omega\mu k_z}\left[(k_x^2 + k_y^2) E_x + k_x k_y E_y\right] \tag{2-17}$$

$$H_z = \frac{1}{\omega\mu}\left[- k_x E_x + k_y E_y\right] \tag{2-18}$$

Thus the complete vector electric and magnetic far field may be determined from the transverse components of the electric field on the z = 0 plane.

Reproduced with permission of the copyright owner. Further reproduction prohibited without permission.

Sample Spacing Criterion

Attention is now focused on the wavenumber domain. The wavenumber domain is divided into two important regions, as shown in Figure 2. The region bounded by the circle of radius k_o contains wavenumber coordinates (k_x, k_y) such that

$$k_x^2 + k_y^2 \leqq k_o^2 \tag{2-19}$$

For these wavenumbers k_z, the propagation constant in the z-direction, is specified from Equation (2-4) as

$$k_z = \pm \sqrt{k_o^2 - k_x^2 - k_y^2} \tag{2-20}$$

where the positive sign on the radical indicates propagation in the $z \geqq 0$ half-space, and the negative sign indicates propagation in the $z \leqq 0$ half-space. Plane waves with wavenumber coordinates satisfying Equation (2-19) have real propagation constants k_z and propagate without attenuation.

Plane waves with wavenumber coordinates (k_x, k_y) such that

$$k_x^2 + k_y^2 > k_o^2 \tag{2-21}$$

result in imaginary values of

$$k_z = \mp j\sqrt{k_x^2 + k_y^2 - k_o^2} \tag{2-22}$$

where the negative sign is chosen for the $z \geqq 0$ half-space to ensure finite power of the electromagnetic fields. These plane waves are

Reproduced with permission of the copyright owner. Further reproduction prohibited without permission.

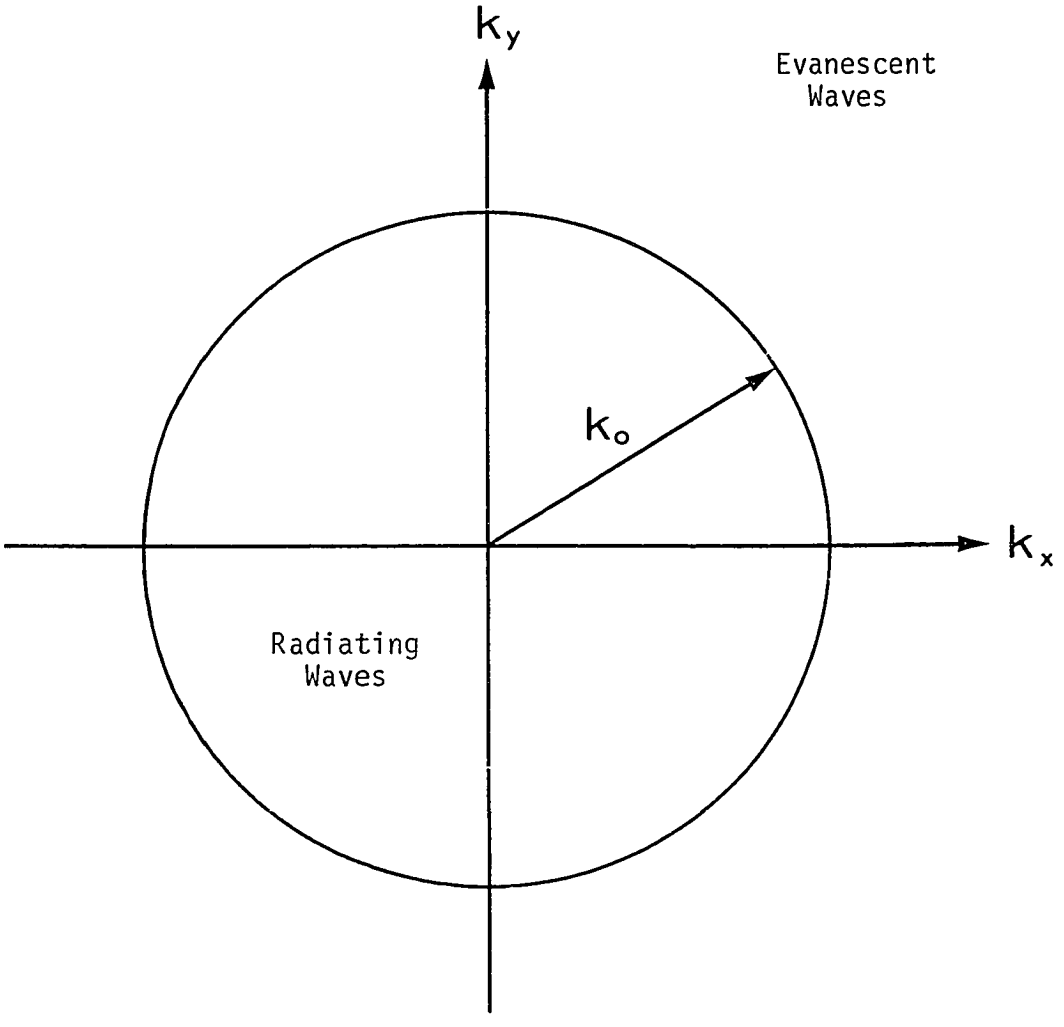

Figure 2. Wavenumber Space

Reproduced with permission of the copyright owner. Further reproduction prohibited without permission.

called evanescent waves and decrease in amplitude with increasing distance in the z direction. More precisely, the amplitudes of the evanescent waves decrease exponentially at a rate specified by

$$e^{-\sqrt{k_x^2 + k_y^2 - k_o^2}\, z} \quad \text{for } k_x^2 + k_y^2 > k_o^2$$

The exponential decrease of evanescent waves with increasing wavenumber and increasing distance from the $z = 0$ plane suggests that a wavenumber limiting process occurs for electromagnetic fields existing in an unbounded medium. If a wavenumber limit did exist the Fourier sampling theorem (29) could be applied to the near-field measurement problem. The two-dimensional Fourier sampling theorem, restated in terms of the domains of electromagnetic theory, states that any wavenumber limited electromagnetic field may be uniquely determined on a planar surface from samples located at the intersections of a rectangular lattice defined on the planar surface. The origin of the planar surface is chosen to coincide with one of the lattice intersections and the two planar axes are aligned parallel to the structure. The lattice spacings in the x and y directions are given by

$$\Delta_x = \pi/k_{xm} \tag{2-23}$$

$$\Delta_y = \pi/k_{ym} \tag{2-24}$$

where k_{xm} and k_{ym} are the magnitude of the largest k_x and k_y coordinates, respectively, of the wavenumber spectrum of the electromagnetic field being sampled. Equations (2-23) and (2-24) show that the sample spacings approach zero for large wavenumber limits k_{xm} and k_{ym}, requiring large

Reproduced with permission of the copyright owner. Further reproduction prohibited without permission.

amounts of measurements and data. The electromagnetic field may be reconstructed from the samples through the well known relation (29)

$$\bar{E}(x,y,0) = \sum_{\ell=-\infty}^{-\infty} \sum_{n=-\infty}^{-\infty} \bar{E}\left(\frac{\ell\pi}{k_{xm}}, \frac{n\pi}{k_{ym}}, 0\right) \frac{\sin(k_{xm}x - \ell\pi)}{(k_{xm}x - \ell\pi)} \frac{\sin(k_{ym}y - n\pi)}{(k_{ym}y - n\pi)} \qquad (2\text{-}25)$$

An electromagnetic field composed entirely of radiating plane waves (e.g., the far field of an antenna) has maximum k_x and k_y wavenumbers of k_o. The sample spacings for this field are given by Equations (2-23) and (2-24) as $\lambda/2$. In general, however, the wavenumber spectrum of the electromagnetic field near a radiating structure will have no apparent wavenumber limit. Nevertheless, an approximate wavenumber limit can be determined as a function of the sample spacing and distance away from the radiating source.

The maximum k_x and k_y wavenumbers within a circle of radius k_m centered about the origin of wavenumber space are

$$k_{xm} = k_{ym} = k_m = \sqrt{k_x^2 + k_y^2} \qquad (2\text{-}26)$$

where (k_x, k_y) lie on the circle of radius k_m. This maximum wavenumber k_m may also be specified as a function of k_z through Equation (2-4) as

$$k_m = \sqrt{k_o^2 - k_{zm}^2} \qquad (2\text{-}27)$$

where k_{zm} is the k_z associated with the wavenumber coordinates (k_x, k_y) lying on the circle of radius k_m. Substituting this value of k_m into Equations (2-23) and (2-24) yields

Reproduced with permission of the copyright owner. Further reproduction prohibited without permission.

$$\Delta_x = \Delta_y = \lambda/2 \left[\frac{1}{\sqrt{1 - \left(\frac{k_{zm}}{k_o}\right)^2}} \right] \qquad (2\text{-}28)$$

For imaginary values of k_{zm} (i.e., evanescent waves) the sample spacings are seen to approach zero with increasing k_{zm}.

The imaginary value of k_{zm} in Equation (2-28) may also be written as a function of the amplitude decay of all evanescent waves with $k_z \neq k_{zm}$. The amplitude decay of evanescent waves may be expressed in decibels as

$$\alpha = 20 \log_{10} \left(e^{-jk_{zm}z}\right)$$

$$= \frac{-j\ 20k_{zm}z}{2.302585} \qquad \text{for } k_x^2 + k_y^2 > k_o^2 \qquad (2\text{-}29)$$

Solving this equation for k_{zm} yields

$$k_{zm} = \frac{-2.302585\ \alpha}{j20z} \qquad \text{for } k_x^2 + k_y^2 > k_o^2 \qquad (2\text{-}30)$$

Letting $z = N\lambda$, where N is the number of wavelengths from the antenna to the near-field measurement plane, and substituting the value of k_{zm} from Equation (2-30) into Equation (2-28) gives

$$\Delta_x = \Delta_y = \lambda/2 \left[\frac{1}{\sqrt{1 + \left(\frac{\alpha}{54.6N}\right)^2}} \right] \quad \text{for } k_x^2 + k_y^2 > k_o^2 \qquad (2\text{-}31)$$

Figure 3 is a graph of Equation (2-31) for four values of N.

Equation (2-31) specifies the required sample spacings in the measurement plane to accurately reproduce all plane waves which, having

Reproduced with permission of the copyright owner. Further reproduction prohibited without permission.

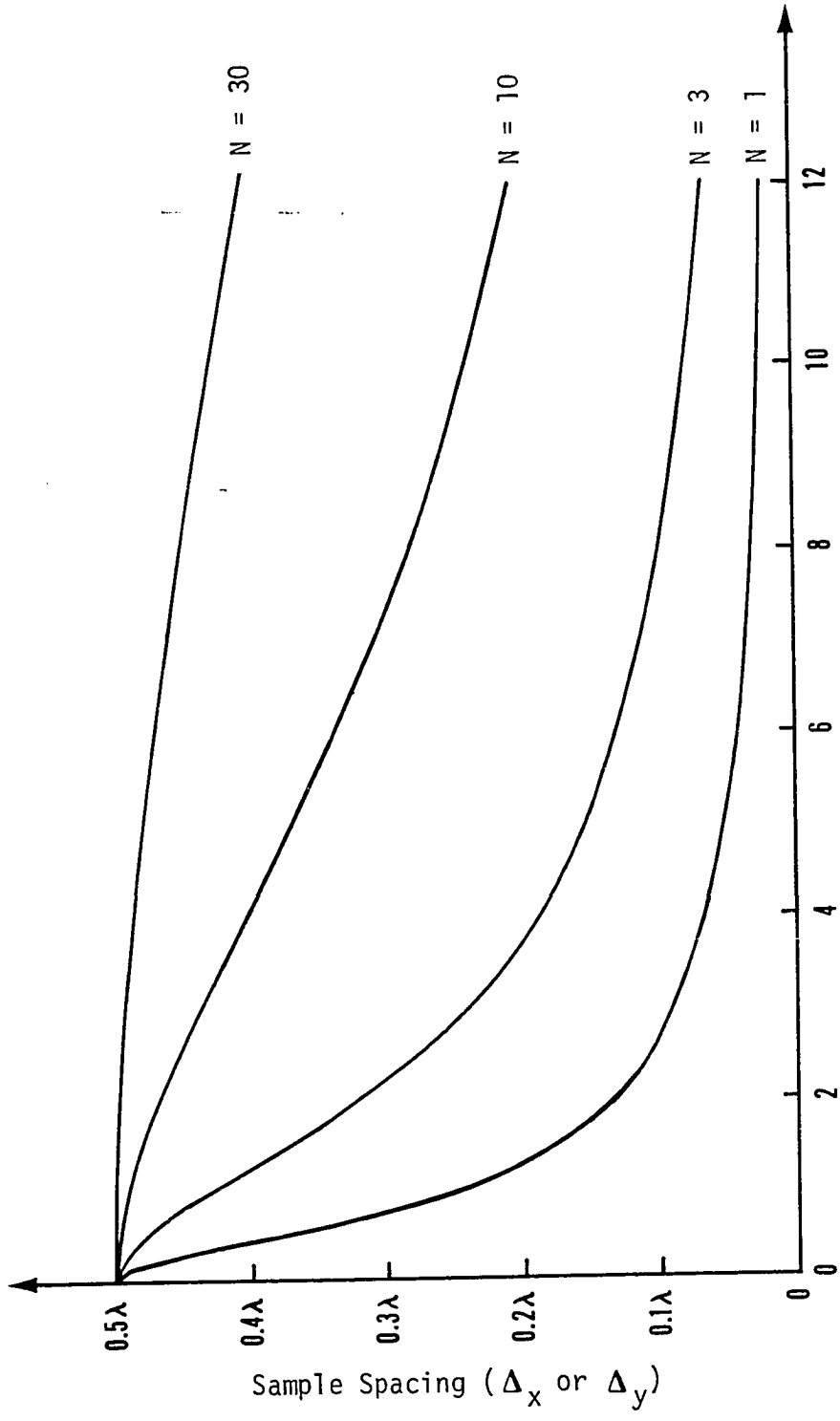

Figure 3. Sample Spacing as a Function of Attenuation Level and Distance from Antenna, in Wavelengths

Reproduced with permission of the copyright owner. Further reproduction prohibited without permission.

traveled the distance to the measurement plane, have undergone an attenuation of less than some preselected amount. The amount of attenuation is somewhat arbitrary, but should be selected to be much greater than the dynamic range of the near-field measurement equipment. In this research a 610 dB level of attenuation was chosen with the near-field plane ten wavelengths from the antenna. The dynamic range of the near-field measurement equipment was 70 dB. From Equation (2-31), the required sample spacing for this level of attenuation and this distance from the antenna is seen to be $\lambda/3$.

Equation (2-31) is true for an arbitrary antenna; however, through the use of a priori information concerning the "Q", the direction of propagation and the angular size of a single beam antenna, the sample spacing may in certain cases be increased. As shown by Rhodes (32), a Q of zero is associated with an aperture field containing no evanescent waves. For a very low Q antenna, typical of wide-band, non-supergain antennas, the field on the near-field measurement plane is composed entirely of radiating waves with a maximum wavenumber of k_o. The sample spacings for this antenna, according to Equations (2-23) and (2-24) should be $\lambda/2$ apart.

Narrow-beam antennas with low values of Q are designed to concentrate most of their radiated energy into small angular portions of the far field. In terms of the wavenumber domain, most of the plane wave wavenumber spectrum is located in a small, well-defined region of wavenumber space within the radiation circle. If the direction from the antenna to the far-field sector of energy concentration is known, the z axis of the near-field measurement plane can be aligned with it. This

Reproduced with permission of the copyright owner. Further reproduction prohibited without permission.

alignment places the origin of the wavenumber domain in the region of far-field energy concentration. The angular size of the far-field sector, if known a priori, can be used to determine the maximum radiating wavenumbers through Equations (2-5) and (2-6). Maximum radiating wavenumbers less than k_o correspond to sample spacings greater than $\lambda/2$, as shown in Equations (2-23) and (2-24).

As an example, let it be assumed that an antenna has a Q of zero. Thus no evanescent waves are assumed on the near-field measurement plane. Let it be further assumed that the antenna concentrates almost all of its energy into an angular region emcompassed by a two degree polar angle about the z-axis of the near-field measurement plane. In wavenumber space this angular region corresponds to a circular region centered about the origin with radius

$$\begin{aligned} k_m &= \sqrt{k_x^2 + k_y^2} \\ &= \sqrt{k_o^2 \sin^2\theta \cos^2\Phi + k_o^2 \sin^2\theta \sin^2\Phi} \\ &= k_o \sin\theta \\ &= 0.0348995\, k_o \end{aligned} \tag{2-32}$$

The sample spacings corresponding to this maximum wavenumber are determined from Equations (2-23) and (2-24) as

$$\Delta_x = \Delta_y = 14.3\lambda \tag{2-33}$$

thereby greatly reducing the number of near-field samples required to calculate the far-field pattern of the antenna through the use of a priori information.

Reproduced with permission of the copyright owner. Further reproduction prohibited without permission.

Near-field Data Minimization

In addition to the natural wavenumber limiting process observed with increasing distance from the antenna, other results of Fourier analysis may be applied to further limit the wavenumber spectrum of the measured electromagnetic field.

As described earlier, the transverse electromagnetic field over a planar surface is related to its plane wave amplitude spectrum through a two-dimensional Fourier transform. This relationship is denoted as

$$\bar{E}(x,y) \overset{F}{\Longleftrightarrow} \bar{A}(k_x,k_y) \tag{2-34}$$

Let another two-dimensional Fourier transform pair of scalar functions be defined in the spatial and wavenumber domains as

$$h(x,y) \overset{F}{\Longleftrightarrow} H(k_x,k_y) \tag{2-35}$$

It is well known from Fourier analysis that the product

$$\bar{M}(k_x,k_y) = \bar{A}(k_x,k_y)H(k_x,k_y) \tag{2-36}$$

has an inverse Fourier transform $\bar{m}(x,y)$ defined in the spatial domain as the spatial convolution (28) of $\bar{E}(x,y)$ with $h(x,y)$

$$\bar{M}(x,y) = \int_{-\infty}^{\infty}\int_{-\infty}^{\infty} \bar{E}(\eta,\xi)h(\eta - x,\xi - y)d_\eta d_\xi \tag{2-37}$$

A wavenumber limiting process of $\bar{A}(k_x,k_y)$ may be carried out if $H(k_x,k_y)$ is specified as

Reproduced with permission of the copyright owner. Further reproduction prohibited without permission.

$$H(k_x,k_y) = 1 \quad \text{for } |k_x| \leq k_{xLP} \quad \text{and} \quad |k_y| \leq k_{yLP}$$
$$= 0 \quad \text{elsewhere} \tag{2-38}$$

$H(k_x,k_y)$ is then called an ideal low-pass filter with wavenumber limits k_{xLP} and k_{yLP}. This filter is ideal in two respects. First, when $\bar{A}(k_x,k_y)$ is multiplied by $H(k_x,k_y)$ the product is wavenumber limited to exactly k_{xLP} and k_{yLP}. Second, the amplitude of $\bar{A}(k_x,k_y)$ is unaltered in the low wavenumber pass region of the filter. The function $H(k_x,k_y)$, as defined in Equation (2-38), has an inverse Fourier transform given by

$$h(x,y) = 4k_{xLP}k_{yLP} \frac{\sin(k_{xLP}x)}{(k_{xLP}x)} \quad \frac{\sin(k_{yLP}y)}{(k_{yLP}y)} \tag{2-39}$$

Thus, wavenumber limiting may be performed in the wavenumber domain as

$$\bar{A}_{LP}(k_x,k_y) = \bar{A}(k_x,k_y)H(k_x,k_y) \tag{2-40}$$

where $\bar{A}_{LP}(k_x,k_y)$ is the resulting wavenumber limited plane wave spectrum. In the spatial domain, this operation is given by the convolution

$$\bar{E}_{LP}(x,y) = 4k_{xLP}k_{yLP}\int_{-\infty}^{\infty}\int_{-\infty}^{\infty} \bar{E}(\eta,\xi) \frac{\sin k_{xLP}(\eta-x)}{k_{xLP}(\eta-x)} \quad \frac{\sin k_{yLP}(\xi-y)}{k_{yLP}(\xi-y)} \, d\eta d\xi \tag{2-41}$$

where $\bar{E}_{LP}(x,y)$ is the inverse Fourier transform of $\bar{A}_{LP}(k_x,k_y)$, and represents the wavenumber limited transverse electromagnetic field. In the spatial domain, the output of a low-pass filter with wavenumber limits of k_{xLP} and k_{yLP} may be sampled at distances

Reproduced with permission of the copyright owner. Further reproduction prohibited without permission.

$$\Delta_x = \pi/k_{xLP} \tag{2-42}$$

$$\Delta_y = \pi/k_{yLP} \tag{2-43}$$

depending only on the wavenumber limits of the low-pass filter k_{xLP} and k_{yLP}.

Thus, to determine the plane wave spectrum of an antenna in a small wavenumber region centered about the origin of wavenumber space or, equivalently, to determine the far-field pattern of an antenna for a small angular region centered about the z-axis of the near-field measurement plane, low-pass filtering can be employed to increase the post-filter sample spacing and minimize the amount of near-field data required for the far-field calculation. Use of low-pass filtering of the measured near-field data allows an important trade-off to be made between the amount of post-filter data and the angular size of the calculated far-field pattern.

Other small angular sectors of the far-field pattern of an antenna may be calculated from near-field measured data with equal degrees of data minimization. Two methods are available.

The first method, which accomplishes data minimization for off-axis sectors, involves the re-orientation of the near-field measurement plane. If the z axis of the measurement plane is aligned parallel with the direction from the antenna to the center of the angular sector of interest, this angular sector will appear centered about the origin of wavenumber space. Low-pass filtering may then be carried out as before.

The second method utilizes another result of Fourier analysis. It is well known from Fourier analysis that the wavenumber spectrum of

Reproduced with permission of the copyright owner. Further reproduction prohibited without permission.

$$\bar{A}_t(k_x,k_y) = \bar{A}(k_x - k_{xt},\ k_y - k_{yt}) \tag{2-44}$$

formed through a wavenumber translation of $\bar{A}(k_x,k_y)$ by an amount (k_{xt},k_{yt}) has an inverse Fourier transform (23)

$$\bar{E}_t(x,y) = e^{-j(k_{xt}x + k_{yt}y)}\bar{E}(x,y) \tag{2-45}$$

Thus, if the small sector of wavenumber space of interest has central coordinates (k_{xt},k_{yt}), the small sector may be translated to the origin of wavenumber space by multiplication of the measured electromagnetic field by the exponential function of Equation (2-45). In the spatial domain the wavenumber translation process is called heterodyning. With the heterodyning operation completed, the measured data may then be low-pass filtered as before, the wavenumber limits of the low-pass filter being chosen by the angular size of the region of interest. (The chosen wavenumber limits also specify the post filter sample spacings and associated amount of data minimization.) Next, the heterodyned, low-pass filtered, near-field data is Fourier transformed to obtain the translated, wavenumber-limited wavenumber spectrum of the measured electromagnetic field. To correct for the heterodyning operation, the wavenumber spectrum must be translated to its proper location in the wavenumber domain as

$$\bar{A}(k_x,k_y) = \bar{A}_t(k_x + k_{xt},k_y + k_{yt}) \tag{2-46}$$

Thus, data minimization depends only on the angular size of the region of interest and not on its location in wavenumber space.

So far, complete knowledge of $\bar{E}(x,y)$ has been assumed for all

Reproduced with permission of the copyright owner. Further reproduction prohibited without permission.

values of (x,y). Experimentally, however, only amplitudes of $\bar{E}(x,y)$ above the noise level of the near-field measurement equipment can be recorded and, typically, only values down to -40 dB of the maximum near-field value are needed for accurate far-field determination. The result of near-field measurement is a finite, usually rectangular matrix of sample values.

In addition to the practical limitation of the infinite measurement plane to a finite size, a low-pass filter of finite spatial dimensions is also desirable. The ideal low-pass filter specified in Equation (2-39) possesses infinite spatial dimensions, which makes it computationally undesirable. A low-pass filter is needed which is finite in spatial dimension and has good filter characteristics in the wavenumber domain.

A Blackman low-pass filter (33) was chosen from a wide class of spatially finite low-pass filters. Figure 4 shows a Blackman low-pass filter with $k_{xLP} = k_{yLP} = 0.5k_o$ in the spatial and wavenumber domains. In comparison to the wavenumber limiting property of the ideal filter, the greatest value of the Blackman filter wavenumber spectrum, beyond its wavenumber limits, is -58 dB below its peak value at (0,0). In comparison, however, to the non-distortion property of the ideal filter, the Blackman low-pass filter possesses a severe amplitude taper, requiring post filter correction. The Blackman low-pass filter is specified in the wavenumber domain as

Reproduced with permission of the copyright owner. Further reproduction prohibited without permission.

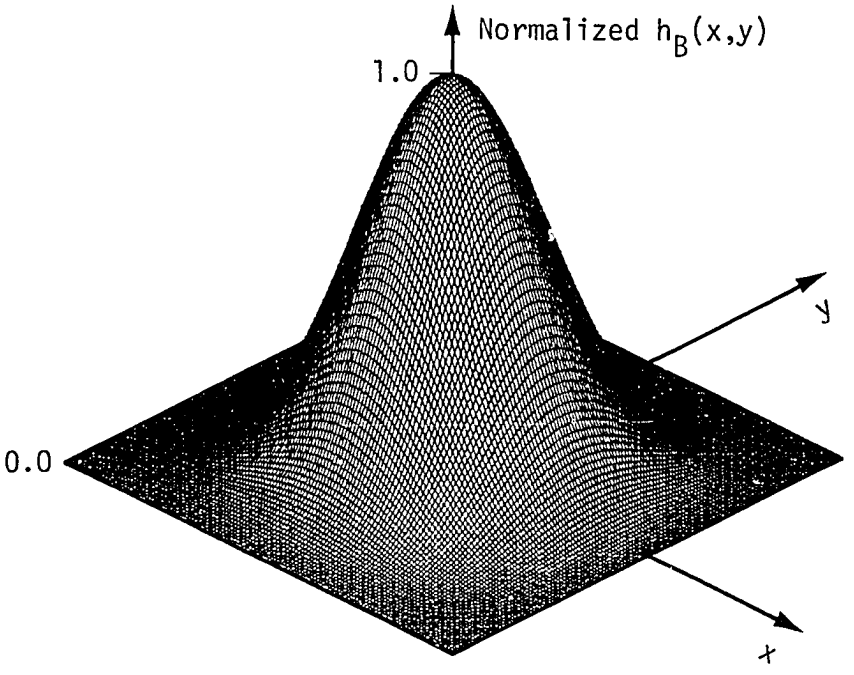

(a) Spatial Domain Characterization

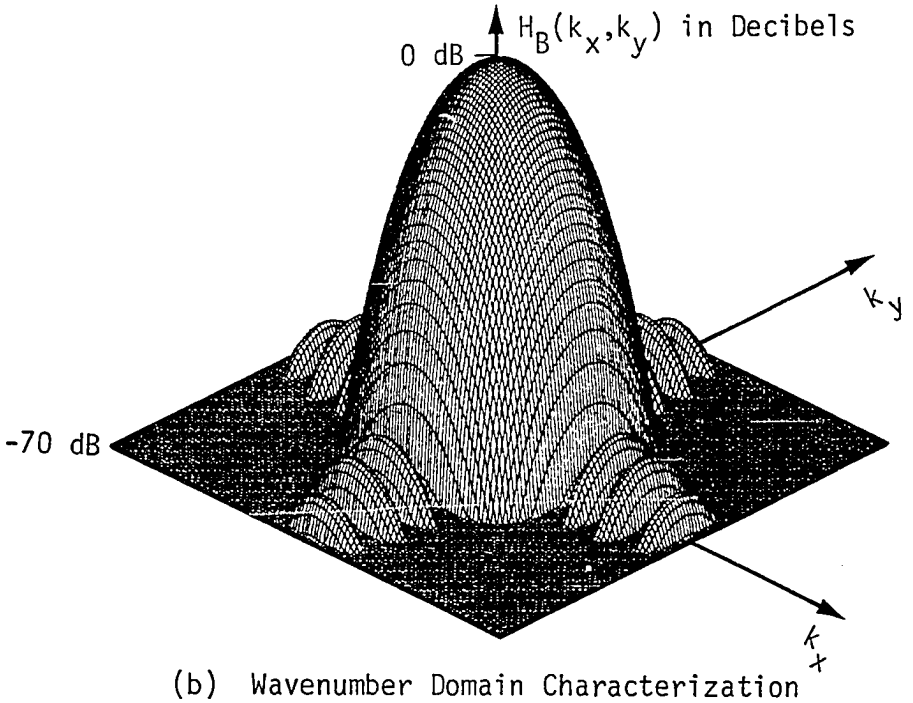

(b) Wavenumber Domain Characterization

Figure 4. Blackman Low-pass Filter Characteristics

Reproduced with permission of the copyright owner. Further reproduction prohibited without permission.

$$H_B(k_x,k_y) = T_xT_y\Bigg(0.84\frac{\sin k_xT_x}{k_xT_x} + 0.50\,\frac{\sin(k_xT_x - \pi)}{(k_xT_x - \pi)} \qquad (2\text{-}47)$$

$$+ 0.50\,\frac{\sin(k_xT_x + \pi)}{(k_xT_x + \pi)} + 0.08\,\frac{\sin(k_xT_x - 2\pi)}{(k_xT_x - 2\pi)}$$

$$+ 0.80\,\frac{\sin(k_xT_x + 2\pi)}{(k_xT_x + 2\pi)}\Bigg)\Bigg(0.84\,\frac{\sin k_yT_y}{k_yT_y}$$

$$+ 0.50\,\frac{\sin\,(k_yT_y - \pi)}{(k_yT_y - \pi)} + 0.50\,\frac{\sin(k_yT_y + \pi)}{(k_yT_y + \pi)}$$

$$+ 0.08\,\frac{\sin(k_yT_y - 2\pi)}{(k_yT_y - 2\pi)} + 0.08\,\frac{\sin(k_yT_y + 2\pi)}{(k_yT_y + 2\pi)}\Bigg)$$

and in the spatial domain as

$$h_B(x,y) = \left(0.42 + 0.5\cos\frac{\pi x}{T_x} + 0.08\cos\frac{2\pi x}{T_x}\right) \cdot \qquad (2\text{-}48)$$

$$\left(0.42 + 0.5\cos\frac{\pi y}{T_y} + 0.08\cos\frac{2\pi y}{T_y}\right) \text{ for } |x| \leqq T_x$$

$$= 0 \quad \text{elsewhere.} \qquad \text{and } |y| \leqq T_y$$

where

$$T_xk_{xLPB} = T_yk_{yLPB} = 3\pi \qquad (2\text{-}49)$$

specifies the wavenumber limits k_{xLPB} and k_{yLPB}.

Having chosen the Blackman filter, the measured electromagnetic

Reproduced with permission of the copyright owner. Further reproduction prohibited without permission.

field is low-pass filtered in the spatial domain, as a spatial convolution.

$$\bar{E}_{LPB}(x,y) = \int_{-\infty}^{\infty}\int_{-\infty}^{\infty} \bar{E}(\eta,\xi)\, h_B(\eta - x,\ \xi - y)\, d_\eta d_\xi \qquad (2\text{-}50)$$

The wavenumber limited near field is then sampled at distances

$$\Delta_x = \pi/k_{xLPB} \qquad (2\text{-}51)$$

$$\Delta_y = \pi/k_{yLPB} \qquad (2\text{-}52)$$

and Fourier transformed to the wavenumber domain. In the wavenumber domain the filter operation may be described as

$$\bar{A}_{LPB}(k_x,k_y) = \bar{A}(k_x,k_y)\, H_B(k_x,k_y) \quad \text{for } |k_x| \leqq k_{xLPB} \text{ and } |k_y| \leqq k_{yLPB} \qquad (2\text{-}53)$$
$$\simeq 0 \quad \text{elsewhere}$$

To correct for the amplitude taper of the Blackman low-pass characteristics, the calculated spectrum $\bar{A}_{LPB}(k_x,k_y)$ is multiplied by the inverse of the wavenumber spectrum of the Blackman filter

$$\bar{A}_{LP}(k_x,k_y) = \frac{\bar{A}_{LPB}(k_x,k_y)}{H_B(k_x,k_y)} = \frac{\bar{A}(k_x,k_y)H_B(k_x,k_y)}{H_B(k_x,k_y)} = \bar{A}(k_x,k_y) \quad \text{for } |k_x| \leqq k_{xLPB} \text{ and for } |k_y| \leqq k_{yLPB}$$
$$\simeq 0 \quad \text{elsewhere.}$$

Thus, a non-ideal low-pass filter may be used provided that it has good wavenumber limiting properties, and provided also that post filter correction is applied.

Many low-pass filters, including the ideal and Blackman filters,

Reproduced with permission of the copyright owner. Further reproduction prohibited without permission.

have separable spatial and wavenumber functions. A separable spatial function may be written as

$$h(x,y) = h_1(x)\, h_2(y) \tag{2-55}$$

When this separable function is used in a convolution process, the convolution may be carried out one dimension at a time. Thus,

$$\begin{aligned} \bar{E}_{LP}(x,y) &= \int_{-\infty}^{\infty}\int_{-\infty}^{\infty} \bar{E}(\eta,\xi)\, h_1(\eta - x)\, h_2(\xi - y)\, d_\eta d_\xi \\ &= \int_{-\infty}^{\infty} h_2(\xi - y)\left[\int_{-\infty}^{\infty} \bar{E}(\eta,\xi)\, h_1(\eta - x)\, d\eta\right] d_\xi \end{aligned} \tag{2-56}$$

A separable filter may be used to obtain one-dimensional slices of the two-dimensional wavenumber spectrum of an antenna. These one-dimensional slices of the wavenumber domain correspond to the standard far-field range measurements (34) performed by fixing one of the two far-field angles and varying the other. Typical examples of these one-dimensional slices are the principal plane patterns of an antenna. The filter function for one such principal plane slice is specified in wavenumber space as

$$\begin{aligned} H_s(k_x,k_y) = T_x U_o(k_y)\Bigg[& 0.84\,\frac{\sin k_x T_x}{k_x T_x} + 0.50\,\frac{\sin (k_x T_x - \pi)}{(k_x T_x - \pi)} \\ & + 0.50\,\frac{\sin (k_x T_x + \pi)}{(k_x T_x + \pi)} + 0.08\,\frac{\sin(k_x T_x - 2\pi)}{(k_x T_x - 2\pi)} \\ & + 0.08\,\frac{\sin(k_x T_x + 2\pi)}{(k_x T_x + 2\pi)}\Bigg] \quad \text{for } |k_x| \leq k_{xLPB} \\ \simeq\ & 0 \quad \text{elsewhere} \end{aligned} \tag{2-57}$$

Reproduced with permission of the copyright owner. Further reproduction prohibited without permission.

This separable filter is composed of an impulse in the k_y dimension and a one-dimensional Blackman filter function in the k_x dimension. The inverse Fourier transform for this filter function is specified in the spatial domain as

$$h_s(x,y) = \frac{T_x}{2\pi}\left(0.42 + 0.5\cos\left(\frac{\pi x}{T_x}\right) + 0.08\cos\left(\frac{2\pi x}{T_x}\right)\right) \text{ for } |x| \leq T_x \qquad (2\text{-}58)$$

$$= 0 \quad \text{elsewhere.}$$

where the impulse transforms to $1/2\pi$ in the spatial domain. The convolution of this separable filter with the measured near-field data has the form

$$\bar{E}_{LPS}(x) = \int_{-\infty}^{\infty} \frac{T_x}{2\pi}\left[0.42+0.5\cos\left[\frac{\pi}{T_x}(\eta-x)\right] + 0.08\cos\left[\frac{2\pi}{T_x}(\eta-x)\right]\right]\left[\int_{-\infty}^{\infty}\bar{E}(\eta,\xi)\,d\xi\right]d\eta \qquad (2\text{-}59)$$

showing that the filter operation in the y dimension is simply an integration of the measured near-field values in the y-direction, leaving the filtered near field a function of x only. The one-dimensional output of this filter is then sampled at x spacings of

$$\Delta_x = \pi/k_{xLPB} \qquad (2\text{-}60)$$

and transformed to the wavenumber domain by a one-dimensional Fourier transform. Thus, even larger reductions in the amount of near-field data may be accomplished when only slices of the far-field patterns are to be calculated.

Reproduced with permission of the copyright owner. Further reproduction prohibited without permission.

Two examples of data minimization are given to illustrate the amount of data reduction possible through the use of low-pass filtering. The near field in both examples is sampled at $\lambda/3$ x and y spacings, as determined from Equation (2-31).

The objective of the first example is to determine the amount of post-filter data required to calculate the far-field pattern of an antenna in a conical region about the z-axis of the near-field measurement plane. The conical far-field sector is shown in Figure 5. The Blackman low-pass filter, as specified in Equation (2-48), is used in this case with wavenumber limits of

$$k_{xLPB} = k_{yLPB} = k_m = \sqrt{k_x^2 + k_y^2} = k_o \sin\theta \qquad (2\text{-}61)$$

where θ is the conical angle shown in Figure 5.

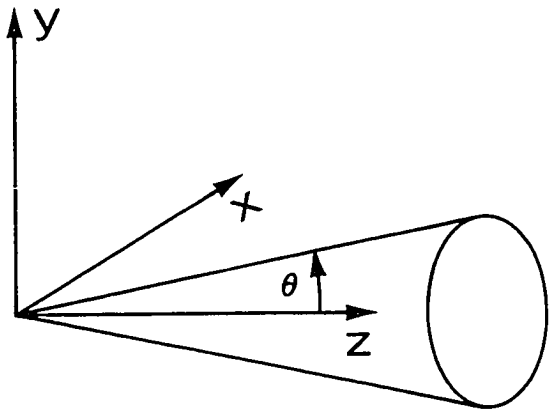

Figure 5. Conical Far-field Sector

Reproduced with permission of the copyright owner. Further reproduction prohibited without permission.

For this example, a 42.3λ by 42.3λ aperture is sampled at λ/3 sample spacings yielding a near-field data matrix of

$$128 \times 128 = 16{,}384 \tag{2-62}$$

transverse vector samples, measured in both amplitude and phase. From Equation (2-49), the spatial dimensions of the Blackman low-pass filter are given by

$$2T_x \times 2T_y = 6\pi/k_{xLPB} \times 6\pi/k_{yLPB} \tag{2-63}$$

square meters. With wavenumber limits of $k_{xLPB} = k_{yLPB} = k_o \sin(\theta)$, the spatial dimensions of the filter become

$$2T_x \times 2T_y = 3\lambda/\sin\theta \times 3\lambda/\sin\theta \tag{2-64}$$

At sample spacings of λ/3 the number of samples required to specify the Blackman low-pass filter is

$$9/\sin\theta \times 9/\sin\theta = 81/\sin^2\theta \tag{2-65}$$

As the spatial convolution of an Nλ by Nλ function with an Mλ by Mλ function yields a $(N + M)\lambda$ by $(N + M)\lambda$ function (26), the convolution of the measured near-field data with the Blackman filter produces a function of $(42.3 + 3/\sin(\theta))\lambda$ by $(42.3 + 3/\sin(\theta))\lambda$ spatial dimensions. This matrix is then sampled at sample spacings of

$$\Delta_x = \Delta_y = \pi/k_o \sin\theta = \lambda/2\sin\theta \tag{2-66}$$

yielding a matrix containing

Reproduced with permission of the copyright owner. Further reproduction prohibited without permission.

$$(84.5 \sin\theta + 6) \times (84.6 \sin\theta + 6) = (84.6 \sin\theta + 6)^2 \quad (2\text{-}67)$$

samples. This matrix is transformed to the wavenumber domain and the far field within the angular region determined.

Figure 6 is a graph of the number of post-filter samples required to calculate the limited far-field pattern as a function of the angular limit of the region. Large reductions in near-field data are seen to be associated with small angular regions. For example, a 10 degree conical region can be calculated with 403 post filter samples in comparison to the 16,384 original near-field samples.

The second data minimization example demonstrates that still greater data reduction is possible for principal plane far-field pattern calculation. Principal plane far-field patterns are typical of the infinite number of one-dimensional far-field patterns which may be determined. The symmetric sector of the xz plane to be determined is shown in Figure 7 and is bounded by the polar angle θ.

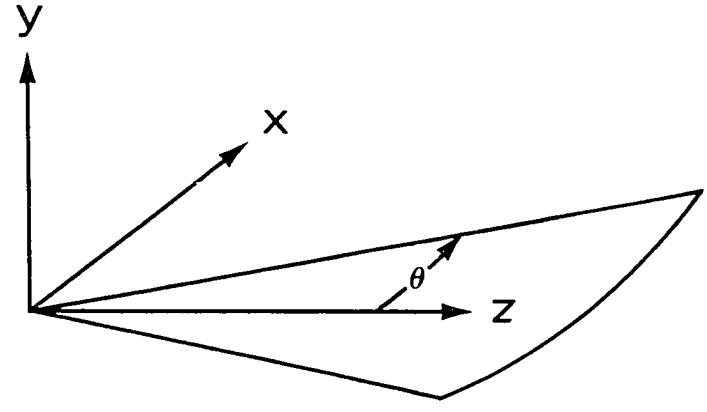

Figure 7. Principal Plane Sector

Reproduced with permission of the copyright owner. Further reproduction prohibited without permission.

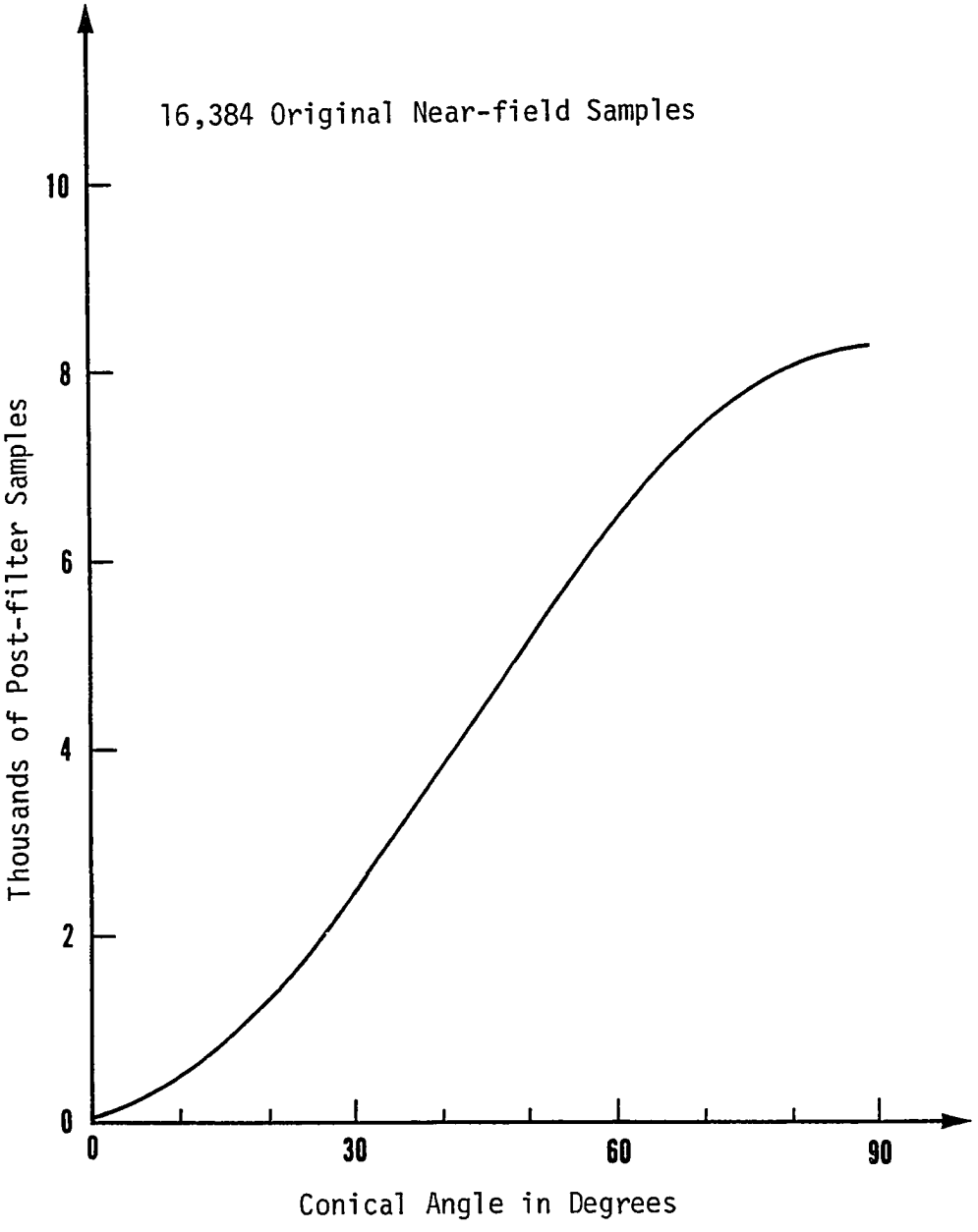

Figure 6. Number of Post-filter Samples Required to Calculate the Conical Far-field Pattern of the First Example

Reproduced with permission of the copyright owner. Further reproduction prohibited without permission.

The low-pass filter used in this example is the separable filter given by Equation (2-58) with wavenumber limit of

$$k_{xLPB} = k_o \sin\theta \cos\Phi$$
$$= k_o \sin\theta \qquad (2\text{-}68)$$

where $\cos(\Phi) = 1$. The 42.3λ by 42.3λ near field of the antenna is again sampled at $\lambda/3$ x and y spacings with a resulting matrix of

$$128 \times 128 = 16{,}384 \qquad (2\text{-}69)$$

(generally complex) transverse vector samples. Filtering in the y dimension is accomplished, according to Equation (2-59), as an integration of the near-field data in the y direction. The integration reduces the number of data values to 128. The 128 samples are then filtered in the x dimension with a one-dimensional Blackman filter. At a sample spacing of $\lambda/3$ the number of samples required to specify the one dimensional Blackman filter with wavenumber limit of $k_{xLPB} = k_o \sin(\theta)$ is $9/\sin\theta$. The one-dimensional convolution yields $(127 + 9/\sin\theta)$ samples, which, when sampled at the sample spacing associated with the wavenumber limit of the filter, yields $(84.6 \sin\theta + 6)$ post filter samples. The one-dimensaional, low-pass filtered, measurement matrix is then transformed to the wavenumber domain to determine the θ sector of the principal plane far-field pattern.

Figure 8 shows a graph of the number of post-filter samples required to calculate the θ sector of the principal plane far-field pattern as a function of θ. It can be seen that a 10 degree sector of

Reproduced with permission of the copyright owner. Further reproduction prohibited without permission.

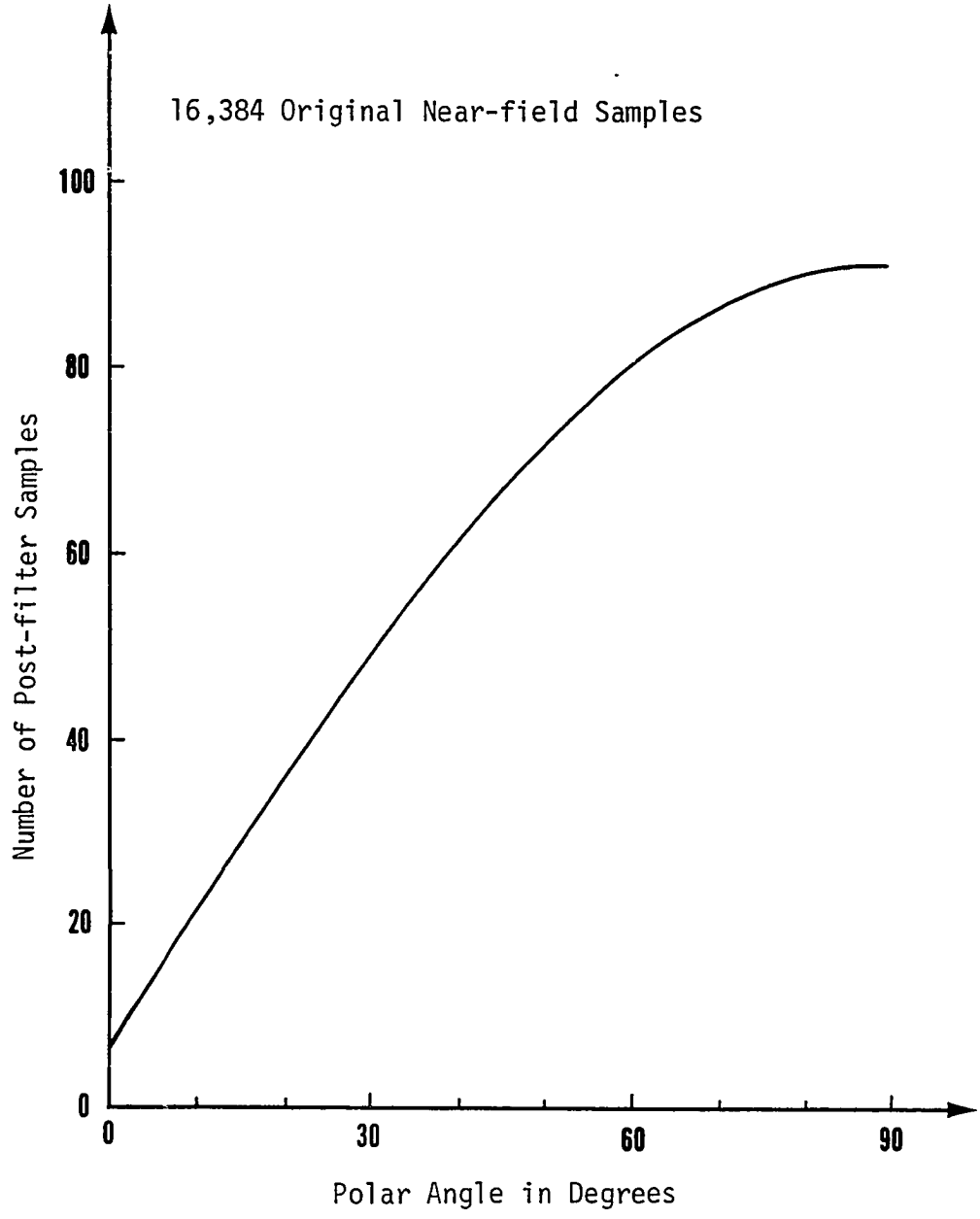

Figure 8. Number of Post-filter Samples Required to Calculate the Principal Plane Far-field Sector of the Second Example

Reproduced with permission of the copyright owner. Further reproduction prohibited without permission.

the principal plane pattern can be calculated with only 20 post-filter samples, a data reduction of almost three orders of magnitude.

Thus the amount of near-field measurement data may be greatly reduced when only one-dimensional sectors of the far-field pattern are to be calculated.

Scattering Approach to the Two Antenna Measurement System

The vector far field, or equivalently, the vector plane wave amplitude spectrum, of an antenna radiating into half-space ($z \geqq 0$) may in principle be obtained from a two dimensional Fourier transform of near-field values measured in a transverse (x,y) plane, as shown in Equation (2-12). However, the measurement of the near field is, in general, affected in a complicated way by the characteristics of the measuring antenna. Kerns (23) gives a method of rigorously correcting for the effects of a measuring antenna of arbitrary but known characteristics, under the assumption that the effects of multiple reflections between the two antennas are negligible. What follows is a summary of his work.

The two-antenna measurement system is shown schematically in Figure 9. In both the receiving and radiating systems the antennas are connected to their respective load and source by shielded waveguides in which only the dominant mode is propagating. The source and load are housed in separate shielded structures.

The volume V associated with the radiating system has two surfaces through which electromagnetic propagation may occur. An incident traveling wave with complex amplitude A_0 and an emerging traveling wave

Reproduced with permission of the copyright owner. Further reproduction prohibited without permission.

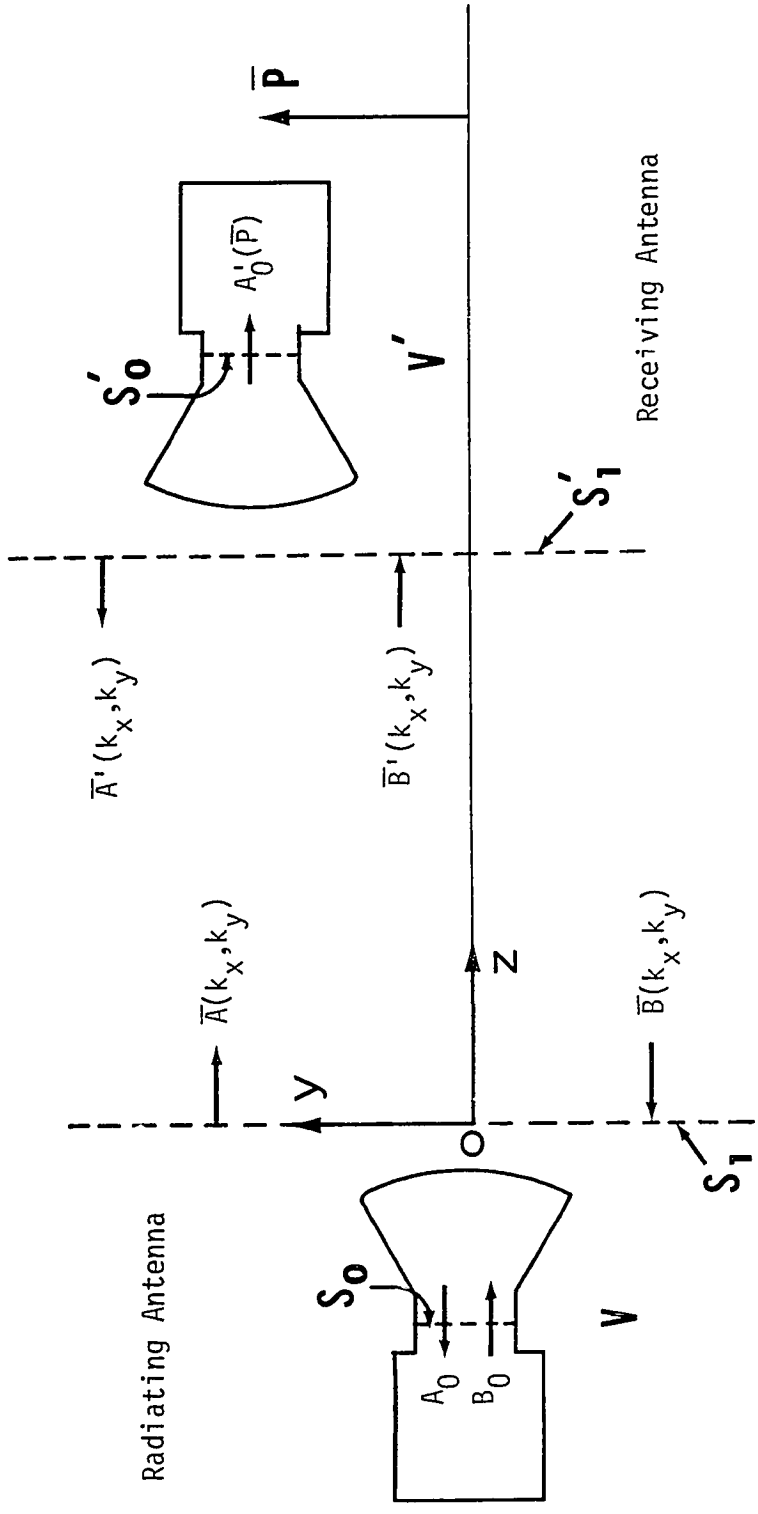

Figure 9. Two Antenna Measurement System Schematic

Reproduced with permission of the copyright owner. Further reproduction prohibited without permission.

B_0 cross the waveguide surface S_0 of the radiating system. A continuum of incident plane waves with complex amplitude $\bar{B}(k_x,k_y)$ and emerging plane waves with complex amplitude $\bar{A}(k_x,k_y)$ cross the planar surface S_1 of the radiating system. The planar surface S_1 is the $z = 0$ plane of the reference right-hand coordinate system Oxyz. A similar volume V', with its associated surfaces of electromagnetic propagation S_0' and S_1', encloses the receiving antenna. With the load of the receiving system matched to its connecting waveguide, no incident traveling wave appears at S_0', leaving only an emerging wave A_0'. A continuum of incident plane waves with amplitudes $\bar{B}'(k_x,k_y)$ and emerging plane waves with amplitudes $\bar{A}'(k_x,k_y)$ cross S_1' of the receiving system. During the near-field measurement process the receiving system is moved throughout the $z = d$ plane and its position is defined by the transverse vector $\bar{P} = x\vec{a}_x + y\vec{a}_y$. Thus the received signal A_0' is a function of $\bar{P}$ and is written $A_0'(\bar{P})$.

As the radiating system is assumed to be linear, a scattering matrix may be written for the emerging electromagnetic fields of the volume V in terms of the incident fields as

$$A_0 = S_{00}B_0 + \int_{-\infty}^{\infty}\int_{-\infty}^{\infty} \bar{S}_{01}(k_x,k_y) \cdot \bar{B}(k_x,k_y)\, dk_x dk_y \qquad (2\text{-}70)$$

$$\bar{A}(k_x,k_y) = \bar{S}_{10}(k_x,k_y)B_0 + \int_{-\infty}^{\infty}\int_{-\infty}^{\infty} \overleftrightarrow{S}_{11}(k_x,k_y;\ell_x,\ell_y) \cdot \bar{B}(\ell_x,\ell_y)\, d\ell_x d\ell_y \qquad (2\text{-}71)$$

using three types of scattering matrix elements: the scalar element S_{00}, the vector elements $\bar{S}_{01}(k_x,k_y)$ and $\bar{S}_{10}(k_x,k_y)$ and the dyadic element $\overleftrightarrow{S}_{11}(k_x,k_y;\ell_x,\ell_y)$.

Reproduced with permission of the copyright owner. Further reproduction prohibited without permission.

A similar scattering matrix may be written for the receiving system for each value of $\bar{P}$ as

$$A_0' = \int_{-\infty}^{\infty}\int_{-\infty}^{\infty} \bar{S}_{01}'(k_x,k_y) \cdot \bar{B}'(k_x,k_y)\, dk_x dk_y \tag{2-72}$$

$$\bar{A}'(k_x,k_y) = \int_{-\infty}^{\infty}\int_{-\infty}^{\infty} \overleftrightarrow{S}_{11}'(k_x,k_y;\ell_x,\ell_y) \cdot \bar{B}'(\ell_x,\ell_y)\, d\ell_x d\ell_y \tag{2-73}$$

where $\bar{S}_{01}'(k_x,k_y)$ is the vector scattering parameter and $\overleftrightarrow{S}_{11}'(k_x,k_y;\ell_x,\ell_y)$ is the dyadic scattering parameter of the receiving system.

Considerable simplification of the two scattering matrices results, if scattering by the receiving system is considered to be negligible. This assumption makes $\bar{A}'(k_x,k_y)$ essentially zero, and it reduces the receiving scattering matrix to

$$A_0' = \int_{-\infty}^{\infty}\int_{-\infty}^{\infty} \bar{S}_{01}'(k_x,k_y) \cdot \bar{B}'(k_x,k_y)\, dk_x dk_y \tag{2-74}$$

In a linear, homogeneous, isotropic and source-free region, the amplitude of the incident plane waves of one system may be given in terms of the amplitude of the emerging planes waves of the other as

$$\bar{B}'(k_x,k_y) = \bar{A}(k_x,k_y)\, e^{-j\vec{k}\cdot\bar{P}}\, e^{-jk_z d} \tag{2-75}$$

$$\bar{B}(k_x,k_y) = \bar{A}'(k_x,k_y)\, e^{+j\vec{k}\cdot\bar{P}}\, e^{jk_z d} \tag{2-76}$$

As $\bar{B}(k_x,k_y)$ is directly related to $\bar{A}'(k_x,k_y)$, it too is essentially zero reducing the radiating system scattering matrix to

$$A_0 = S_{00} B_0 \tag{2-77}$$

Reproduced with permission of the copyright owner. Further reproduction prohibited without permission.

$$\bar{A}(k_x,k_y) = \bar{S}_{10}(k_x,k_y)B_0 \tag{2-78}$$

Equation (2-78) shows that, under these assumptions, the transmitting scattering parameter $\bar{S}_{10}(k_x,k_y)$ of the radiating antenna is directly related to the plane wave amplitude spectrum of the field on the z = 0 plane.

$\bar{B}'(k_x,k_y)$ may be determined from Equations (2-75) and (2-78) as a function of $\bar{S}_{10}(k_x,k_y)$. With this value of $\bar{B}'(k_x,k_y)$ the receiving system's scattering equation becomes

(2-79)

$$A_0'(\bar{P}) = B_0 \int_{-\infty}^{\infty}\int_{-\infty}^{\infty} \left[\bar{S}_{01}'(k_x,k_y) \cdot \bar{S}_{10}(k_x,k_y)\, e^{-jk_z d} \right] e^{-j(k_x x + k_y y)}\, dk_x dk_y$$

which is recognized as a two-dimensional Fourier transform. Taking the inverse Fourier transform of Equation (2-79) yields

(2-80)

$$S_m'(k_x,k_y) = \bar{S}_{01}'(k_x,k_y) \cdot \bar{S}_{10}(k_x,k_y) = \frac{e^{-jk_z d}}{(2\pi)^2 B_0} \int_{-\infty}^{\infty}\int_{-\infty}^{\infty} A_0'(\bar{P}) e^{-j\vec{k}\cdot\bar{P}}\, d\bar{P}$$

Equation (2-80) determines one linear combination of the two components of $\bar{S}_{10}(k_x,k_y)$; in general, one must take two such sets of measurements with "independent" antennas. In many cases a single antenna can be used in two different orientations, obtained, say, by a 90 degree rotation around the z-axis. An additional measurement equation is then obtained

$$S_m''(k_x,k_y) = \bar{S}_{01}''(k_x,k_y) \cdot \bar{S}_{10}(k_x,k_y) \tag{2-81}$$

where $S_m''(k_x,k_y)$ is the Fourier transform of the second set of near-field data and $\bar{S}_{01}''(k_x,k_y)$ is the receiving scattering parameter of the receiving

Reproduced with permission of the copyright owner. Further reproduction prohibited without permission.

system for its new orientation.

The two vector components of $\bar{S}_{10}(k_x,k_y)$ may be found from Equations (2-80) and (2-81), the measurement equations, if the receiving characteristics $\bar{S}_{01}'(k_x,k_y)$ and $\bar{S}_{01}''(k_x,k_y)$ of the near-field measuring antenna are known, and the near-field data Fourier transforms $S_m'(k_x,k_y)$ and $S_m''(k_x,k_y)$ are known. Since, as shown by Equation (2-78), $\bar{A}(k_x,k_y)$ and $\bar{S}_{10}(k_x,k_y)$ differ by only a multiplicative constant, the far field of the antenna is readily determined from $S_{10}(k_x,k_y)$ as

$$\bar{E}(k_x,k_y) = \frac{jk_o \cos\theta\, e^{-j\vec{k}\cdot\vec{r}}}{r}\ \bar{S}_{10}(k_x,k_y) \quad \text{for} \quad k_x^2 + k_y^2 \leq k_o^2 \qquad (2\text{-}82)$$

$$= 0 \qquad \text{elsewhere}$$

Thus, the far field of an antenna is directly proportional to the wavenumber spectrum of the electromagnetic field over the near-field planar surface weighted by the wavenumber spectrum of the near-field probe.

Far-Field Measurement Equations

As shown in the previous section, the wavenumber spectrum of the near-field probe must be known to correct the calculated wavenumber spectrum of the near-field measurements. The purpose of this section is to develop equations for the determination of the wavenumber spectrum of an arbitrary antenna as a function of measured far-field data.

The two antenna far-field measurement system to be analyzed is shown schematically in Figure 10. The receiving antenna is located on a far-field hemisphere of the radiating antenna in a fixed orientation with respect to the radius vector. The far-field condition implies (6) that

Reproduced with permission of the copyright owner. Further reproduction prohibited without permission.

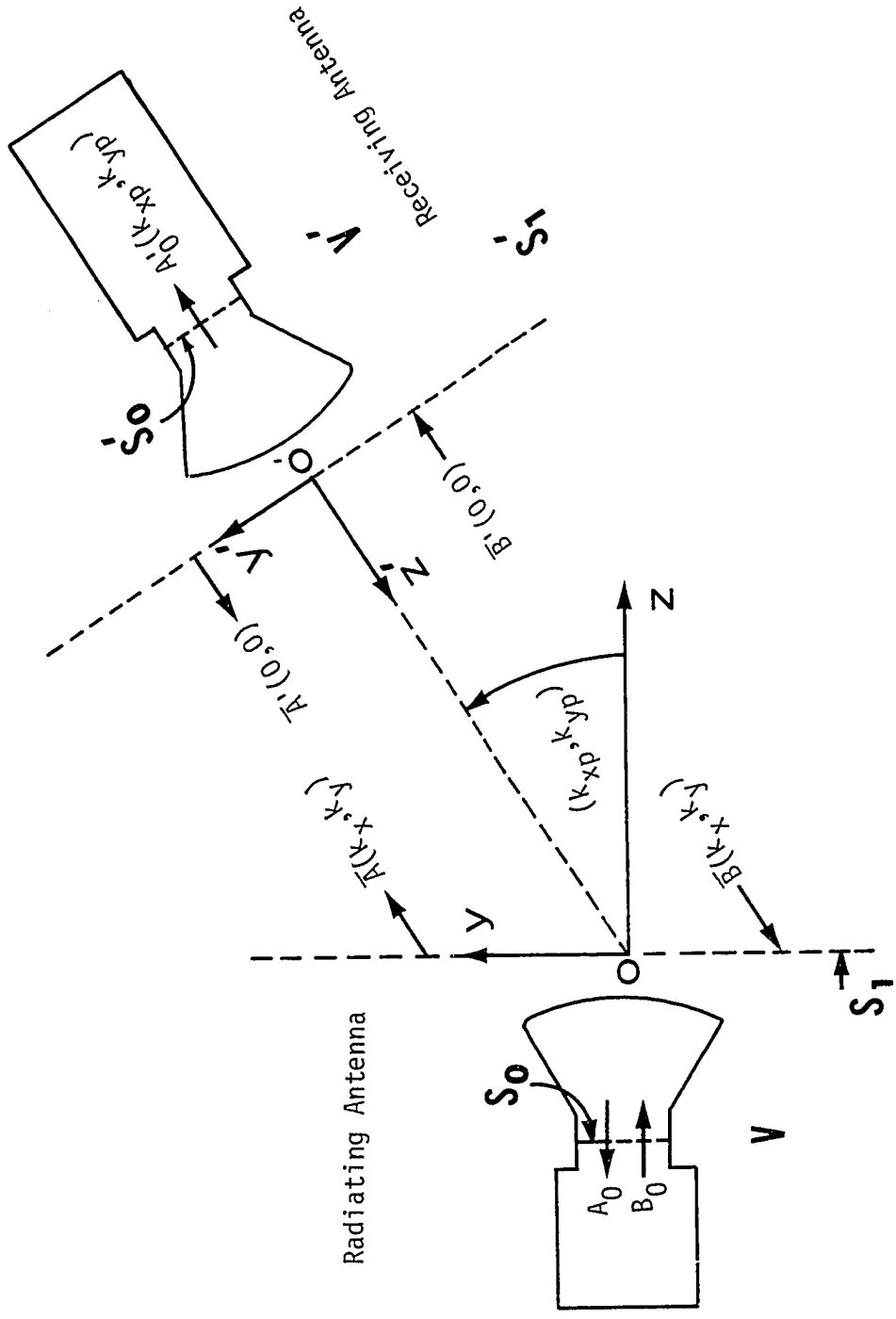

Figure 10. Far-field Measurement System Schematic

Reproduced with permission of the copyright owner. Further reproduction prohibited without permission.

the field at each point of the far-field hemispherical surface is a plane wave propagating in the radial direction. Thus, for each receiving point on the far-field hemisphere, the direction of propagation relative to the receiving antenna is constant.

The two-antenna measurement system is described as before using the scattering matrices of Equations (2-70) through (2-73). The scattering matrices are reduced by applying several assumptions concerning the receiving antenna. If the receiving antenna is matched to its load, the scalar scattering parameter S_{00}' of the receiving antenna is zero. If no multiple reflections exist between the radiating and receiving antenna, the emerging spectrum of plane waves from the receiving antenna is essentially zero, making the impinging spectrum of plane waves at the radiating antenna essentially zero. With these assumptions applied, the scattering matrix for the radiating system becomes

$$A_0 = S_{00}B_0 \tag{2-83}$$

$$\bar{A}(k_x,k_y) = \bar{S}_{10}(k_x,k_y)B_0 \tag{2-84}$$

and the scattering matrix for the receiving antenna then takes the form

$$A_0' = \int_{-\infty}^{\infty}\int_{-\infty}^{\infty} \bar{S}_{01}'(k_x,k_y) \cdot \bar{B}'(k_x,k_y)\,dk_x dk_y \tag{2-85}$$

For far-field measurements made on a hemisphere of constant radius from the origin of the radiating antenna's coordinate system, the location of the receiving antenna is given by the wavenumber coordinates (k_{xp},k_{yp}). The wavenumber coordinates of the receiving antenna may also

Reproduced with permission of the copyright owner. Further reproduction prohibited without permission.

be written in terms of the spherical angles θ and Φ of Figure (2-1) using Equations (2-5) and (2-6).

From Equation (2-12) the far field at each (k_{xp},k_{yp}) position of the receiving antenna is seen to be a single plane wave which has an amplitude directly related to the emerging plane wave spectrum of the radiating system. The far-field plane wave in the (k_{xp},k_{yp}) direction impinges at the receiving antenna in the receiving antenna's ($k_x = 0$, $k_y = 0$) direction. This relationship is written as

$$\bar{B}'(0,0) = \frac{jk_o \cos\theta\, e^{-j\vec{k}\cdot\vec{r}}}{r}\, \bar{A}(k_{xp},k_{yp}) \qquad (2\text{-}86)$$

for each (k_{xp},k_{yp}) position of the receiving antenna.

Substituting Equations (2-86) and (2-84) into Equation (2-85) gives

$$A_0'(k_{xp},k_{yp}) = \frac{jB_0k_o \cos\theta\, e^{-j\vec{k}\cdot\vec{r}}}{r}\, \bar{S}_{01}'(0,0) \cdot \bar{S}_{10}(k_{xp},k_{yp}) \qquad (2\text{-}87)$$

where the integral of Equation (2-85) vanishes for other values of k_x and k_y. Equation (2-87) is true for each (k_{xp},k_{yp}) position of the receiving antenna. A second far-field measurement may be made for the receiving antenna rotated 90 degrees about its z' axis, yielding a second relation

$$A_0''(k_{xp},k_{yp}) = \frac{jB_0k_o \cos\theta\, e^{-j\vec{k}\cdot\vec{r}}}{r}\, \bar{S}_{01}''(0,0) \cdot \bar{S}_{10}(k_{xp},k_{yp}) \qquad (2\text{-}88)$$

where $\bar{S}_{01}''(0,0)$ is the on-axis, transverse vector, scattering parameter of the receiving antenna for its new orientation. The two transverse vector components of $\bar{S}_{10}(k_{xp},k_{yp})$ may then be determined from the two far-field measurement equations, (2-87) and (2-88).

Reproduced with permission of the copyright owner. Further reproduction prohibited without permission.

The above measurement equations may be normalized by the constant

$$j \frac{B_0 k_o e^{-j\vec{k}\cdot\vec{r}}}{r}$$

if the relative plane wave spectrum of the radiating antenna is to be determined. The normalized measurement equations are then given by

$$\frac{A_N'(k_{xp},k_{yp})}{\cos\theta} = \bar{S}_{01}'(0,0) \cdot \bar{S}_{10}(k_{xp},k_{yp}) \qquad (2\text{-}89)$$

$$\frac{A_N''(k_{xp},k_{yp})}{\cos\theta} = \bar{S}_{01}''(0,0) \cdot \bar{S}_{10}(k_{xp},k_{yp}) \qquad (2\text{-}90)$$

Thus, when far-field conditions apply, the wavenumber spectrum of an arbitrary antenna may be found point by point if the ($k_x = 0$, $k_y = 0$) value of the receiving antenna's wavenumber spectrum is known.

On-axis Polarization Ratio Measurement Equation

To determine the wavenumber spectrum of a near-field probe from measured far-field data, $\bar{S}_{01}'(0,0)$ and $\bar{S}_{01}''(0,0)$ of the far-field receiving antenna must be known. The objective of this section is to determine the relative values $\bar{S}_{01}'(0,0)$ and $\bar{S}_{01}''(0,0)$ of an arbitrary antenna as a function of the measured far-field polarization ratios of a group of three arbitrary antennas taken pairwise. It is understood that one of the three arbitrary antennas is the antenna for which the relative values $\bar{S}_{01}'(0,0)$ and $\bar{S}_{01}''(0,0)$ are to be determined.

The two-antenna, far-field, on-axis measurement system is shown in Figure 11. For this far-field, on-axis measurement system the far-field

Reproduced with permission of the copyright owner. Further reproduction prohibited without permission.

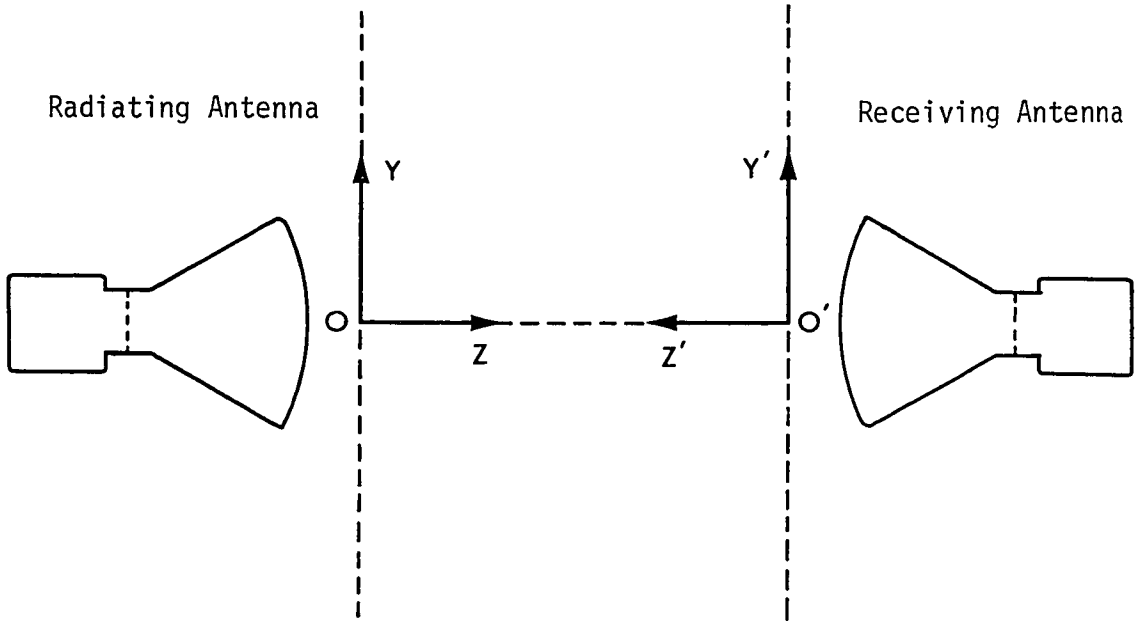

Figure 11. Two Antenna, On-axis, Far-field Measurement System Schematic

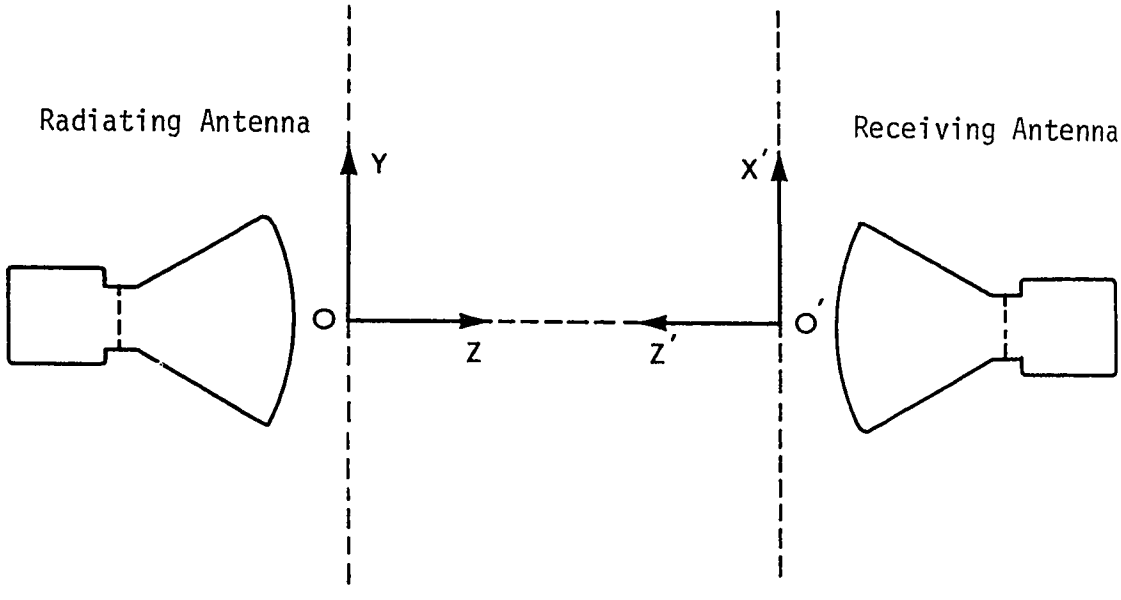

Figure 12. Rotated Two Antenna, On-axis, Far-field Measurement System Schematic

Reproduced with permission of the copyright owner. Further reproduction prohibited without permission.

measurement equations, Equations (2-89) and (2-90) reduce to

$$A_N'(0,0) = \bar{S}_{01}'(0,0) \cdot \bar{S}_{10}(0,0) \tag{2-91}$$

$$A_N''(0,0) = \bar{S}_{01}''(0,0) \cdot \bar{S}_{10}(0,0) \tag{2-92}$$

where $\cos\theta = 1$ for ($k_x = 0$, $k_y = 0$). The transverse vector components of $\bar{S}_{01}'(0,0)$ are explicitly displayed in terms of the coordinate system of the radiating antenna as

$$\bar{S}_{01}'(0,0) = -S_x\vec{ax} + S_y\vec{ay} \tag{2-93}$$

Let $\bar{S}_{01}''(0,0)$ be the on-axis point of the wavenumber spectrum of the receiving antenna of Figure 11 rotated 90 degrees such that the y' axis of the receiving antenna is aligned with the x axis of the radiating antenna as shown in Figure 12. For this new orientation of the receiving antenna, $\bar{S}_{01}''(0,0)$ may be expressed in terms of the x and y components of $\bar{S}_{01}'(0,0)$ as

$$\bar{S}_{01}''(0,0) = S_y\vec{ax} + S_x\vec{ay} \tag{2-94}$$

Kerns (24) has shown that the receiving and transmitting scattering parameters of an antenna obey a reciprocity relationship which for the on-axis case of the receiving antenna becomes

$$\bar{S}_{10}'(0,0) = \bar{S}_{01}'(0,0) \tag{2-95}$$

If the receiving antenna of Figure 11 is rotated 90 degrees about the y axis and used as the radiating antenna, the transmitting scattering

Reproduced with permission of the copyright owner. Further reproduction prohibited without permission.

parameter of this radiating antenna may be written

$$\bar{S}_{10}(0,0) = S_x\vec{ax} + S_y\vec{ay} \tag{2-96}$$

An additional subscript is used on the x and y components of the on-axis receiving and transmitting scattering parameters to denote which of the three arbitrary antennas is being referred to as #1, #2, or #3.

The first far-field measurement is made using antenna #1 as the radiating antenna and antenna #2 as the receiving antenna oriented as shown in Figure 11. In terms of the scattering parameters of the two antennas, the measurement may be described by the normalized far-field measurement equation (2-91) as

$$A_N'(0,0) = S_{y1}S_{y2} - S_{x1}S_{x2} \tag{2-97}$$

Without changing the amplitude or phase of the excitation and without changing the z distance separating the two antennas, antenna #2 is rotated about the z' axis, as shown in Figure 12. The received signal $A_N''(0,0)$ is given by Equation (2-92) as

$$A_N''(0,0) = S_{x1}S_{y2} + S_{y1}S_{x2} \tag{2-98}$$

The measured polarization ratio is formed by dividing Equation (2-98) by Equation (2-97). Thus

$$M_{1,2} = \frac{A_N''(0,0)}{A_N'(0,0)} = \frac{S_{x1}S_{y2} + S_{y1}S_{x2}}{S_{y1}S_{y2} - S_{x1}S_{x2}} \tag{2-99}$$

Reproduced with permission of the copyright owner. Further reproduction prohibited without permission.

Dividing numerator and denominator of Equation (2-99) by $S_{y1}S_{y2}$ yields

$$M_{1,2} = \frac{\frac{S_{x1}}{S_{y1}} + \frac{S_{x2}}{S_{y2}}}{1 - \frac{S_{x1}}{S_{y1}}\frac{S_{x2}}{S_{y2}}} \qquad (2\text{-}100)$$

At this point the true complex polarization ratios for each antenna can be defined as

$$R_1 = \frac{S_{x1}}{S_{y1}} \quad , \quad R_2 = \frac{S_{x2}}{S_{y2}} \quad , \text{ and } \quad R_3 = \frac{S_{x3}}{S_{y3}} \qquad (2\text{-}101)$$

In terms of the complex polarization ratios, Equation (2-100) then becomes

$$M_{1,2} = \frac{R_1 + R_2}{1 - R_1R_2} \qquad (2\text{-}102)$$

The same measurement can be repeated for the antenna pair #1 and #3, with the resulting measured polarization ratio equation

$$M_{1,3} = \frac{R_1 + R_3}{1 - R_1R_3} \qquad (2\text{-}103)$$

Similarly, for the antenna pair #2 and #3

$$M_{2,3} = \frac{R_2 + R_3}{1 - R_2R_3} \qquad (2\text{-}104)$$

Equations (2-102), (2-103), and (2-104) may now be solved for R_1,

Reproduced with permission of the copyright owner. Further reproduction prohibited without permission.

R_2, and R_3. The solution for R_1 is

$$R_1 = -(B/A) + \sqrt{(B/A)^2 + 1} \tag{2-105}$$

where

$$A = M_{2,3} - M_{1,2} - M_{1,3} - M_{1,2}M_{1,3}M_{2,3} \tag{2-106}$$

and

$$B = M_{1,2}M_{1,3} - M_{2,3}M_{1,3} - M_{1,2}M_{2,3} - 1 \tag{2-107}$$

Thus the far-field, complex polarization ratio of an arbitrary antenna may be found using Equation (2-105) and performing the six measurements outlined above. The relative values of $\bar{S}_{01}'(0,0)$ and $\bar{S}_{01}''(0,0)$ may then be found from the complex polarization ratio.

Reproduced with permission of the copyright owner. Further reproduction prohibited without permission.

CHAPTER III

INSTRUMENTATION AND EQUIPMENT

The measurement systems, described in this chapter, were implemented to demonstrate the feasibility and practicality of far-field determination from near-field measurement data.

The near fields of two test antennas were measured on three different occasions with three different near-field measurement probes. Redundant measurements were made to demonstrate the repeatability of the calculated far-field patterns, independent of the measuring near-field probe for two non-symmetric antennas. The far fields of the two antennas were next measured directly on a standard far-field range for comparison to the patterns calculated from the near-field measurements.

To correct the calculated far-field patterns for the presence of the near-field probe, the probe's wavenumber spectrum was determined. As the probe antennas used were electrically small, their wavenumber spectra were most conveniently determined from their far-field amplitude and phase patterns. A single antenna was used to measure the far-field patterns of the probe antennas. This far-field antenna was located on a far-field hemispherical surface centered about the probe antenna in a fixed orientation with respect to the radius vector. In this configuration only the complex polarization ratio of the far field antenna was needed to correct the measured far-field patterns for the presence of the far-field antenna.

In summary, four measurement systems are described: the

Reproduced with permission of the copyright owner. Further reproduction prohibited without permission.

polarization measurement system, the probe far-field measurement system, the near-field measurement system, and the test antenna far-field measurement system. In addition to the instrumentation and equipment incorporated in the four measurement systems, the two test antennas, three near-field probe antennas, and the probe far-field antenna are described.

Antennas and Probes

Two X-band parabolic dish antennas were designed and constructed in order to measure their near fields and far fields. Photographs of the mounted large and small test antennas are shown in Figure 13(a) and Figure 13(b) respectively. The larger test antenna is center-fed with an open-ended waveguide located approximately at the focal point of its 31-inch diameter parabolic dish reflector. The smaller test antenna is fed with a small pyramidal horn located 20.5 degrees in azimuth from the main axis of its 25-inch diameter dish. No attempt was made to achieve symmetry of far-field patterns or any special characteristics in the design or construction of these antennas. A mount was also constructed to hold either of the test antennas and was covered with Spongex 12 CM Broadband Absorber.

Three probe antennas were designed and constructed to measure the near fields of the two X-band test antennas described above. A photograph of the three near-field probe antennas and the far-field probe antenna is shown in Figure 13(c). The smallest probe is an open-ended section of RG-52U X-band waveguide with tapered edges at its mouth to reduce back scattering. The next largest probe is a 0.81 by 1.88 inch, X-band, pyramidal horn antenna with a 5.7 degree E-plane half angle flare and a 15.7 degree H-plane half angle flare. The largest near-field

Reproduced with permission of the copyright owner. Further reproduction prohibited without permission.

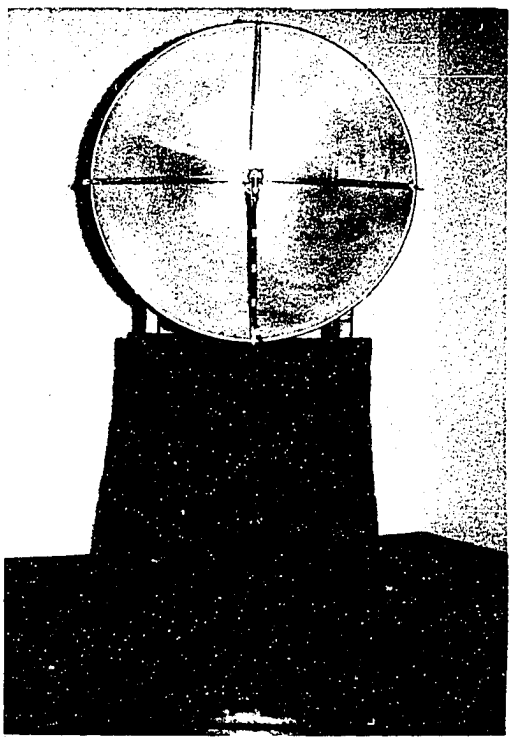

(a) Large Test Antenna

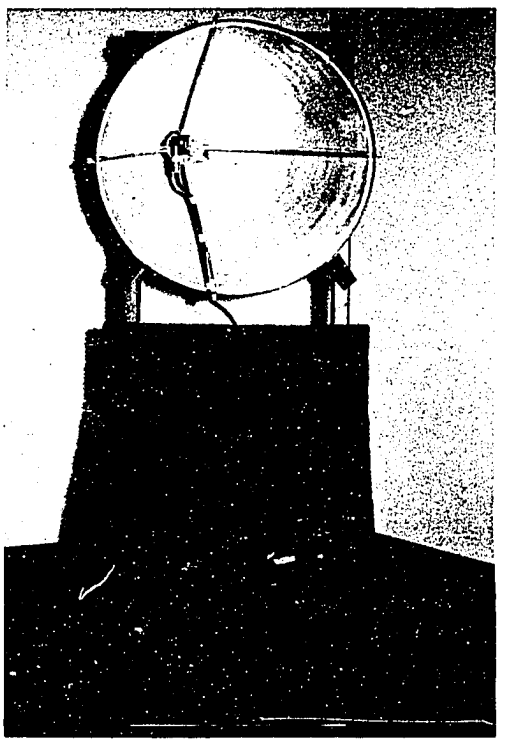

(b) Small Test Antenna

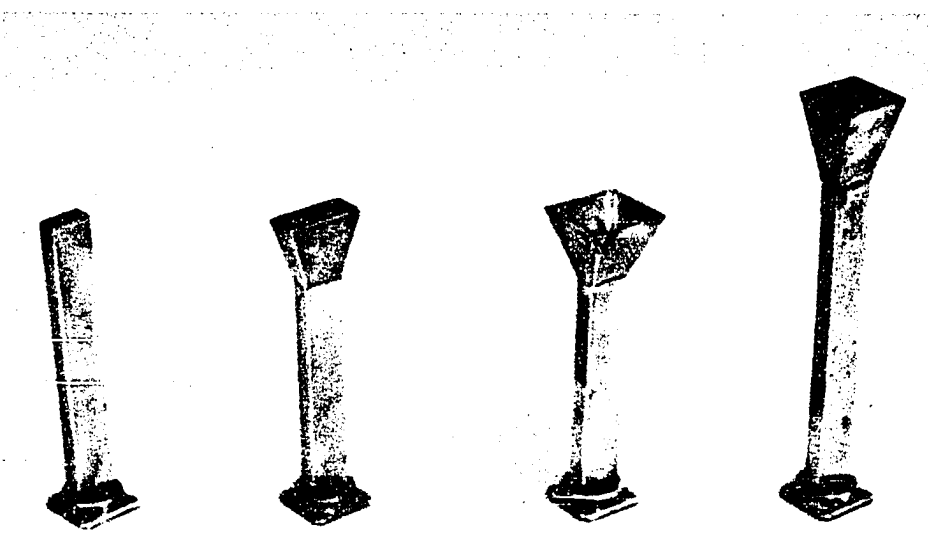

(c) From Left to Right: Open-ended Waveguide Probe, Small Horn Probe, Large Horn Probe, and Far-field Probe

Figure 13. Test Antennas and Probes

Reproduced with permission of the copyright owner. Further reproduction prohibited without permission.

probe is a 1.81 by 1.88 inch, X-band, pyramidal horn with a 22.8 degree E-plane half angle flare and a 15.7 degree H-plane half angle flare. All three probes measure seven inches in length and are fitted with a standard X-band flange.

A single 1.55 by 1.55 inch, pyramidal horn antenna with a 15.2 degree E-plane half angle flare and a 8.2 degree H-plane half angle flare was designed and constructed to measure the far-field patterns of the three near-field probe antennas. The far-field probe antenna measures ten inches in length and is fitted with a standard X-band flange.

Polarization Measurement System

The complex polarization ratio of the far-field probe antenna is determined to correct the measured relative far-field amplitude and phase patterns of the three near-field probe antennas. As shown in Chapter II, the complex polarization ratio of the far-field probe may be determined from three measured on-axis polarization ratios. The measured polarization ratio is recorded from each pair of antennas in a group of three antennas which include the far-field probe antenna. Thus the polarization measurement system must permit the measurement of the on-axis amplitude and phase of two orthogonal components of the far-field pattern. As each antenna must be in the far field of the other for this measurement, the antennas are separated by a distance greater than the sum of their individual far field distances. A schematic diagram of the polarization measurement system and the coordinate system used are shown in Figure 14.

The receiving antenna is held in position by a rotary probe holder capable of complete rotation without changing the amplitude or phase of the signal passing through it. The rotary probe holder is a

Reproduced with permission of the copyright owner. Further reproduction prohibited without permission.

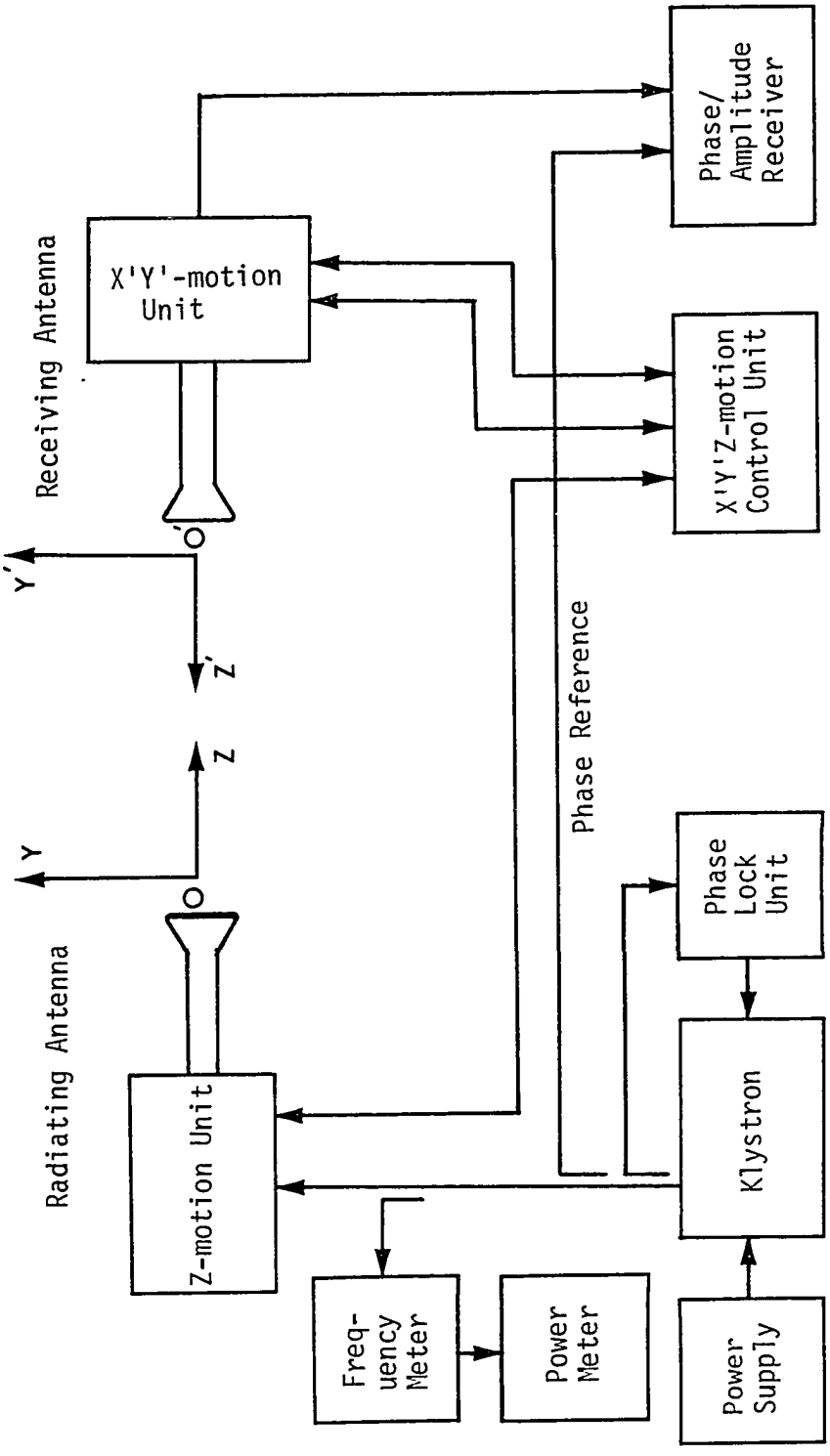

Figure 14. Schematic Diagram of the Polarization Ratio Measurement System

Reproduced with permission of the copyright owner. Further reproduction prohibited without permission.

hollow aluminum tube, 30 inches long and 3.5 inches in diameter. The holder houses an X-band waveguide mounted on eight centering posts, a waveguide to coaxial connector, a 10-inch section of RG-212U coaxial cable, a Scientific Atlanta Series 14-2 mixer, and a Scientific Atlanta Series 10-1 Rotary Joint connected in series. The rotary probe holder is transported to any point in a 100 by 100 inch plane by a Scientific Atlanta XY-motion Unit and associated Series 4100 Position Control and Indicator Unit. A mechanical scissor unit built into the xy-motion unit connects the rotary probe holder to a stationary point on the xy-motion unit with RG-214U RF cable and three rotary joints. This scissor unit enables movement of the receiving antenna throughout a 100 by 100 inch plane without changing the amplitude or phase of the received signal due to xy motion. A photograph of the transmitting antenna structure, rotary probe holder, and the xy-motion unit is shown in Figure 15.

Microwave energy passes from the xy-motion unit to a Scientific Atlanta Series 1750 Wide Range Phase/Amplitude Receiving System through RG-214U RF cable lashed to rigid supports. The receiver provides direct reading of the relative amplitude of the received signal and the relative difference in phase between the received signal and the phase of the microwave source output. The transmitting antenna is mounted on a Scientific Atlanta Z-motion Unit. The xy position of the transmitting antenna is fixed by its mounting structure; however, its z-position may be varied by the control and position indicator unit.

The transmitting antenna is connected to a X-13 klystron by a non-moving RG-212U RF cable. The klystron is powered by a Narda Microwave Corporation Model 438 Klystron Power Supply. The output of the klystron

Reproduced with permission of the copyright owner. Further reproduction prohibited without permission.

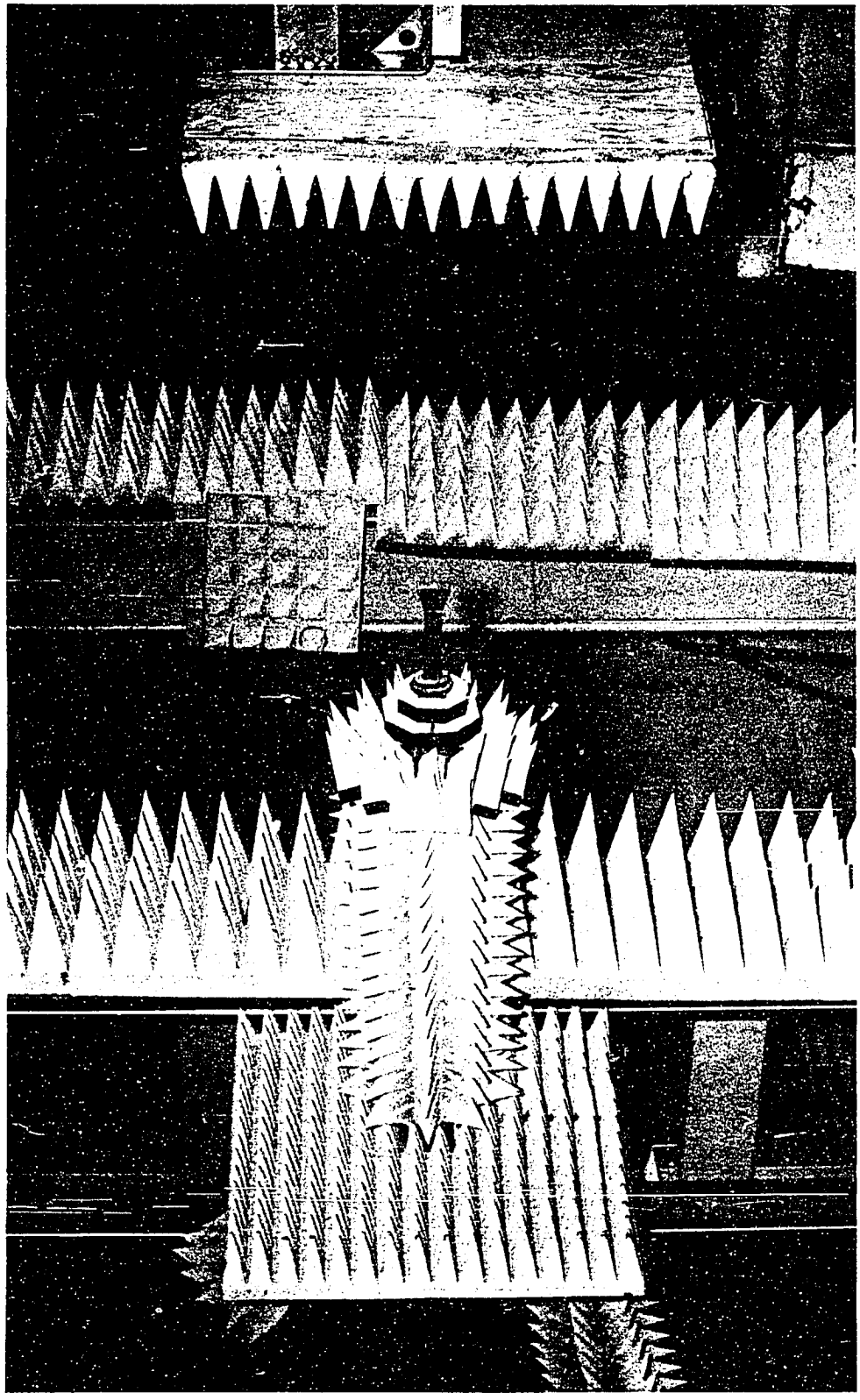

Figure 15. Antenna Mounts Used in the Polarization Ratio Measurement System

Reproduced with permission of the copyright owner. Further reproduction prohibited without permission.

is phase locked to a crystal frequency reference with a FEL Model 133-AK Klystron Synchronizer and its power output is continuously monitored with a Hewlett Packard Model 431B Power Meter to insure constant output energy. The frequency of the klystron is initially set and periodically checked with a MICROLAB/FXB Model X410B Frequency Meter connected in series with the power meter.

The xy-motion unit, the z-motion unit, the rotary probe holder, the entire wall behind the xy-motion unit and much of the surrounding area are covered with B. F. Goodrich VHP-8 microwave absorbing material with a normal incident minimum absorption of 50 db at X-band. The receiver, xyz-motion control and position indicator unit, the klystron, klystron power supply, synchronizer, frequency meter, and power meter are located behind a wall of absorbing material away from the measurement area.

Probe Measurement System

The far-field amplitude and phase patterns of two orthogonal components of each of the three near-field probe antennas must be measured to determine their individual complex wavenumber spectra. An apparatus for accomplishing these measurements was designed and constructed, and is shown schematically in Figure 16. The two spherical motions which allow measurement of the far-field patterns over almost a complete hemisphere of each of the near-field probes are performed with separate rotation devices.

A photograph of the near-field probe measurement system is shown in Figure 17(a). In this figure the elevation angle is approximately 45 degrees and the azimuth angle is approximately 40 degrees. The

Reproduced with permission of the copyright owner. Further reproduction prohibited without permission.

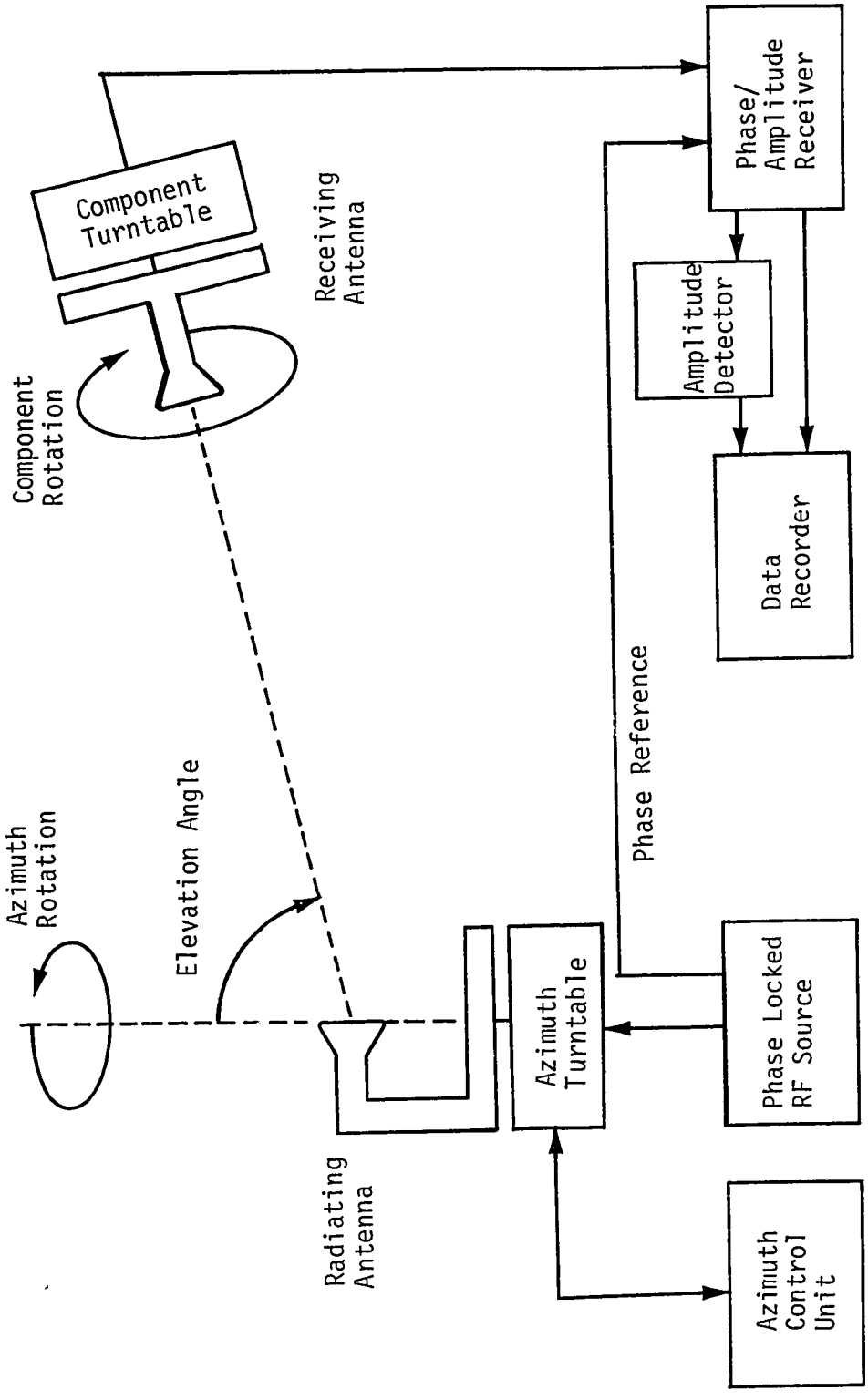

Figure 16. Schematic Diagram of the Probe Far-field Measurement System

Reproduced with permission of the copyright owner. Further reproduction prohibited without permission.

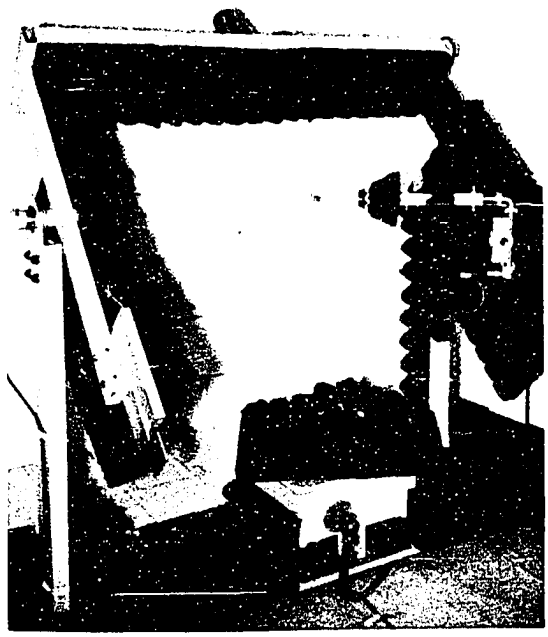

(a) Spherical Motion Unit

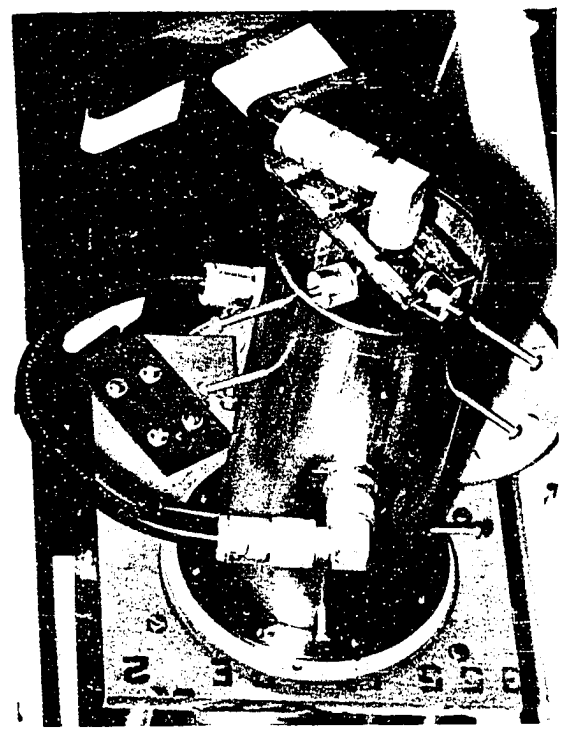

(b) Far-field Probe Holder

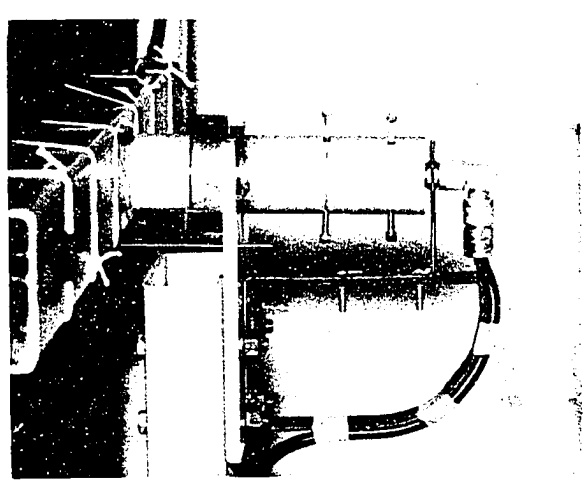

(c) V-bearing Rotary Joint

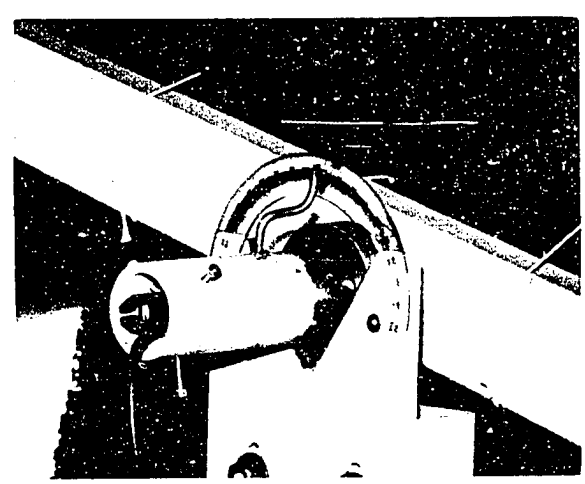

(d) Telescope and Elevation Indicator

Figure 17. Probe Far-field Measurement System

Reproduced with permission of the copyright owner. Further reproduction prohibited without permission.

near-field probes which are used as transmitting antennas, are mounted on a standard azimuth turntable and positioned by a servo control unit. The azimuth mounting structure supports the near-field probes in a horizontal position at the end of a 20-inch, X-band waveguide mounted on eight adjustable centering posts. The structure places the mouth of each of the near-field probe antennas 24 inches above the azimuth turntable and directly over the center of azimuth rotation. The near-field probes are connected to the X-band source through a variable attenuator mounted at the other end of the 20-inch X-band waveguide, a waveguide to coaxial adapter, an RG-212U RF cable and a rotary joint mounted in the base of the azimuth turntable concentric to the axis of the azimuth rotation. A Scientific Atlanta prototype phase locked source supplies 9.68 GHz energy to the transmitting antenna. A 20-inch separation between the transmitting and receiving antennas is maintained by the elevation carriage.

The far-field probe antenna is used as the receiving antenna and is rotated in elevation by an inverted swing carriage. This elevation carriage is supported by two V-bearings and counter-balanced to permit the carriage to rest at any elevation angle without a locking mechanism. The far-field probe antenna is supported on the elevation carriage by a four inch diameter, bearing mounted, aluminum tube whose axis of rotation is perpendicular to a far-field spherical surface. The far-field probe antenna is mounted within the aluminum tube on eight centering posts. A photograph of a rear view of the mounted far-field probe holder is shown in Figure 17(b). Also within the tube are a Scientific Atlanta Series 14-1 Mixer, a ten inch length of RG-212U RF cable, and a Scientific

Reproduced with permission of the copyright owner. Further reproduction prohibited without permission.

Atlanta Series 10-1 Rotary Joint. The rotary joint is supported on six centering posts and is connected to the mixer with RF cable. The mixer is mounted directly on a standard waveguide to coaxial adapter fixed on the far-field probe antenna.

The received signal is transmitted to the receiver via RG-212U RF cable and through another rotary joint located inside one of the the V-bearing shafts supporting the elevation carriage. A photograph of the V-bearing shaft housing the elevation rotary joint is shown in Figure 17(c). The receiving apparatus thus allows the far-field probe to be rotated to receive energy associated with any tangential component of the far field of a near-field probe antenna at any elevation angle without amplitude or phase errors due to these motions. The other V-bearing shaft houses a ten inch pinhole telescope mounted on six centering posts and is shown in Figure 17(d). An elevation angle indicator is mounted on this V-bearing assembly and is also shown in Figure 17(d).

A Scientific Atlanta Series 1750 Wide Range Phase/Amplitude Receiving System is used to determine the relative phase difference between the received signal and the source signal, and the relative amplitude of the received signal. The amplitude signal from the receiver passes through a Scientific Atlanta Model 333 Synchronous Detector to convert the 1000 Hz, amplitude-modulated amplitude signal to its equivalent baseband signal. As the phase signal from the receiver is already in a baseband form, no conversion is necessary for it. The amplitude and phase signals are recorded on an Amplex Model 4000 analog tape recorder. All of the internal structural surfaces of the probe far-field measurement system are covered with Spongex 12 CM Broadband Absorber. The

Reproduced with permission of the copyright owner. Further reproduction prohibited without permission.

complete measurement system is located in a small anechoic room lined with Eccosorb FR-330 absorbing material. The receiver, source, detector, control unit, and recorder are located behind a wall of absorbing material within the anechoic room.

Near-Field Measurement System

A near-field measurement system was designed and constructed to measure the amplitude and phase of two orthogonal components of the near fields of the two test antennas. The near-field measurement apparatus is basically the same apparatus used to make the polarization ratio measurements described earlier.

A schematic diagram of this system is given in Figure 18 and a photograph of the system is shown in Figure 19. The klystron with its associated power supply, synchronizer, frequency meter, and power monitor used to supply 9.68 GHz energy to the transmitting antennas, is the same source used in the polarization measurement system. The test antennas are used to transmit and are secured, together with their mount, on the z-motion unit. The near-field probes are used as receiving antennas and are held in position by the same rotary probe holder and xy-motion unit used in the polarization measurement system. Full use of the xy-motion unit is made in the near-field measurement system as the near-field probes are moved throughout a 53.1 by 53.1 inch xy planar surface in front of the test antenna being measured. Microwave connection to the receiver from both the receiving antenna and the microwave source are the same as described in the polarization measurement system. The same synchronous detector used in the probe measurement system is used to demodulate the amplitude output of the receiver. The baseband phase and amplitude

Reproduced with permission of the copyright owner. Further reproduction prohibited without permission.

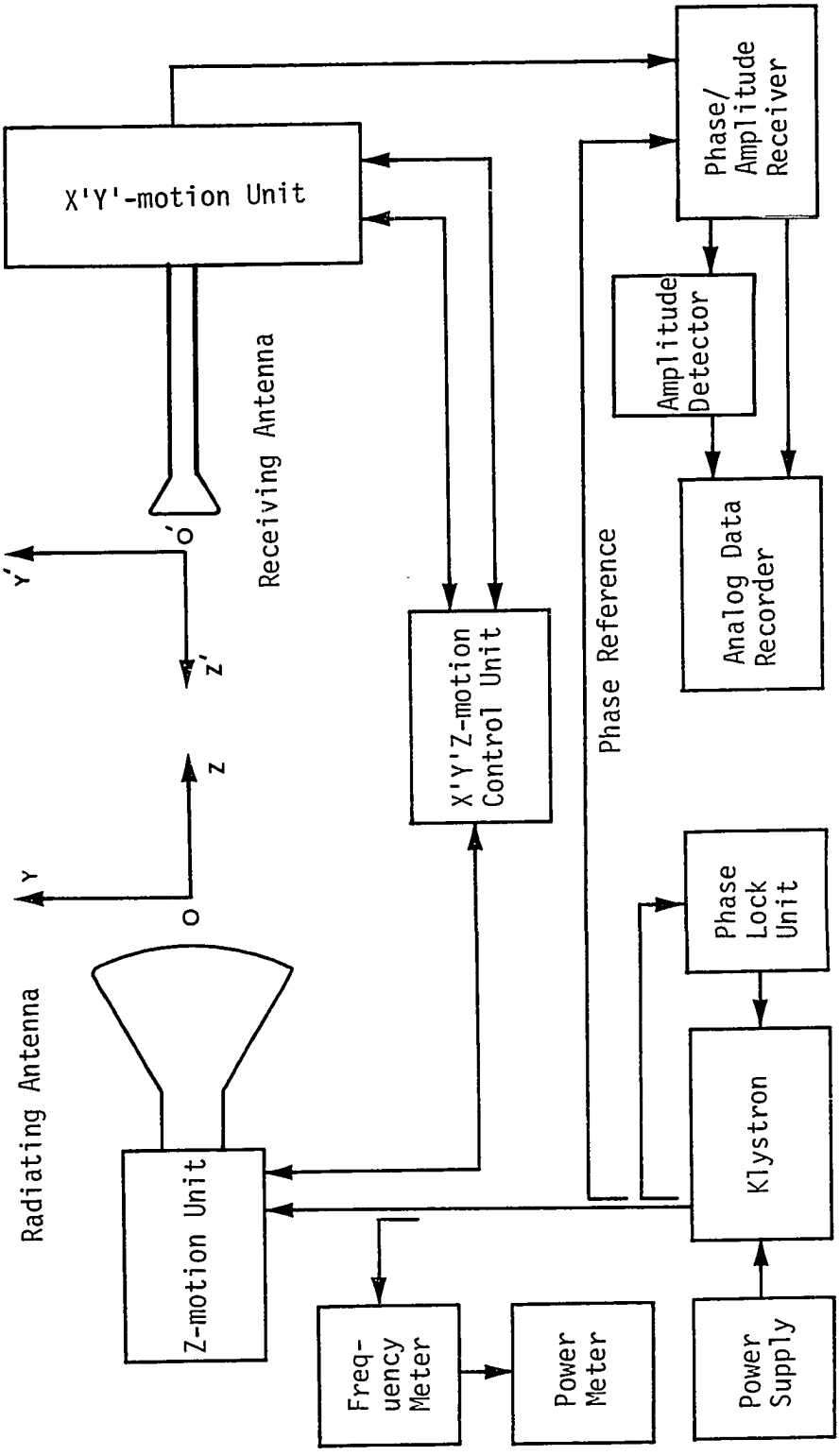

Figure 18. Schematic Diagram of the Near-field Measurement System

Reproduced with permission of the copyright owner. Further reproduction prohibited without permission.

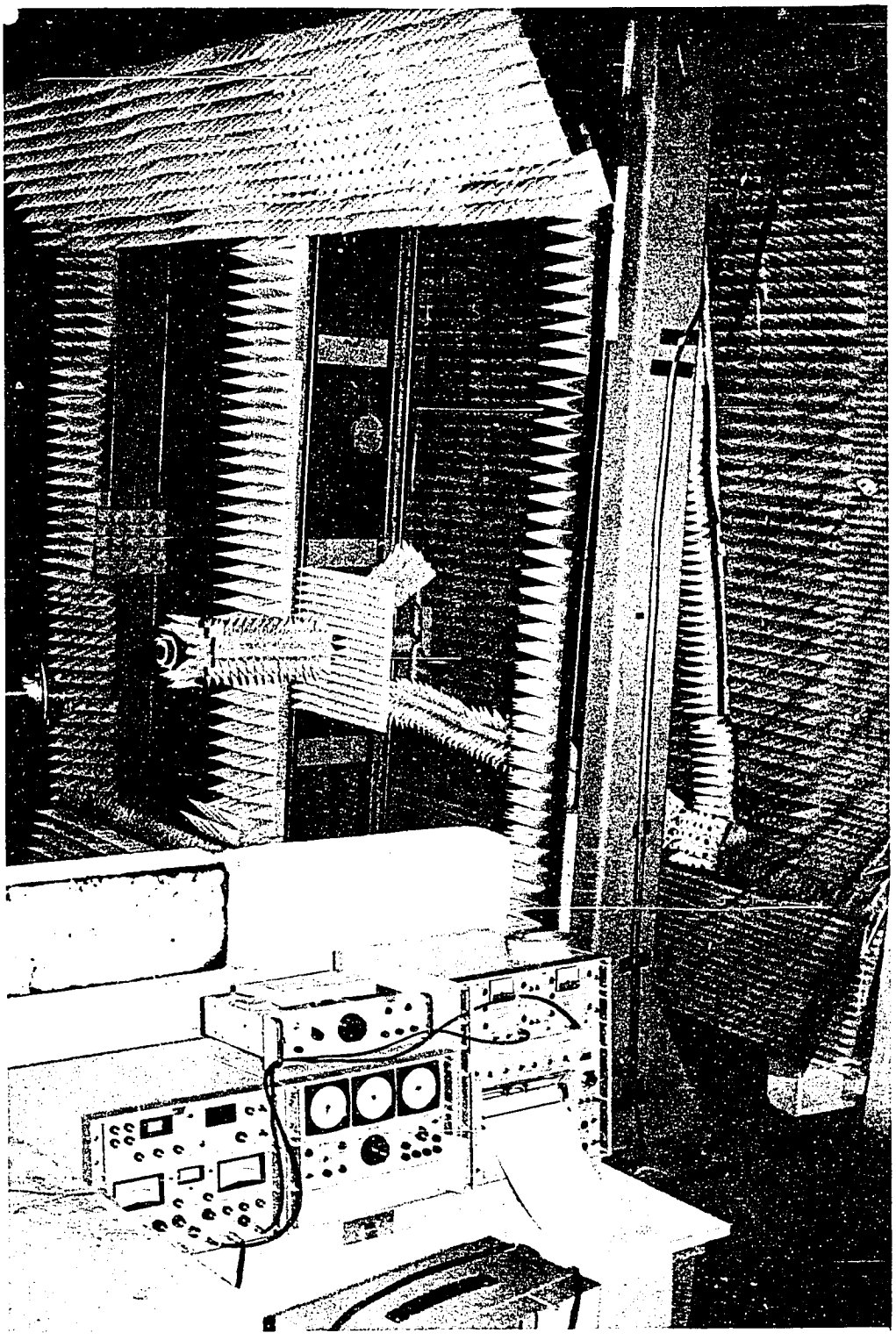

Figure 19. Near-field Measurement System

Reproduced with permission of the copyright owner. Further reproduction prohibited without permission.

signals are recorded on a Honeywell Portable Recorder/Reproducer Model 8100.

The recorder also records an x position voltage derived from a microswitch mounted on the x-motion part of the xy-motion unit. When the xy-motion unit positions the probe antenna within the 53.1 inch x-measurement area, the microswitch closes producing a voltage of eight volts at the recorder. When the probe is outside the x-measurement area, the microswitch closes and the voltage at the recorder is zero.

As in the polarization measurement system the xy-motion unit, the z-motion unit, the rotary probe holder, the entire wall behind the xy-motion unit and much of the surrounding area is covered with B. F. Goodrich VHP-8 microwave absorbing material. The receiver, synchronous detector, recorder, xyz-motion control and position indicator unit, klystron, power meter, frequency meter, synchronizer, and klystron power supply are located behind a wall of absorbing material removed from the near-field measurement area.

Far-Field Measurement System

Georgia Tech's 700 foot, far-field antenna range was used to measure the far-field power patterns of the two test antennas. This far-field measurement system uses a 48-inch diameter parabolic dish antenna with a three dB beam width of approximately 1.8 degrees as the transmitting antenna, and is housed atop the Electrical Engineering Building at a height of approximately fifty-five feet above the ground. The test antenna is used as the receiving antenna and is mounted atop a specially fabricated receiving instrumentation room on the roof of the Georgia

Reproduced with permission of the copyright owner. Further reproduction prohibited without permission.

Tech Engineering Experiment Station.

A photograph of the receiving room and antenna positioner is shown in Figure 20. The antenna mounting platform is approximately 49 feet above the ground and 700 feet from the transmitting antenna. The receiving antenna, together with its mount, is mounted on an azimuth-over-elevation turntable and is capable of complete azimuth motion and an elevation motion of nine degrees up or down from horizontal. A schematic diagram of the far-field measurement system is given in Figure 21.

The receiving antenna is connected to a Scientific Atlanta Series 1600 Wide Range Receiver by RF cable and via a Scientific Atlanta Series 14-1 Mixer and a Scientific Atlanta Series 10-1 Rotary Joint. The amplitude output of the receiver is fed directly into a Scientific Atlanta Series 1520 Rectangular Recorder which traces in ink the amplitude of the received power in decibels as a function of the azimuth angle of the receiving antenna. The azimuth rotation of the receiving antenna is controlled by a Scientific Atlanta 4100 Position Control Unit. The control unit also provides a servo position signal for the chart recorder keeping the chart and antenna position synchronized. The elevation angle of the antenna is controlled by a hand winch located at the base of the antenna positioner.

Microwave energy at the transmitting end of the range is furnished by an X-13 klystron. A Narda Microwave Corporation Model 438 Klystron Power Supply supplies anode, reflector, and filament voltages to the klystron and a MICROLAB/FXB Model X410B frequency meter is used to set the frequency of the klystron to 9.68 GHz. The klystron is connected to the transmitting antenna by semirigid RF cable. The direction of the main

Reproduced with permission of the copyright owner. Further reproduction prohibited without permission.

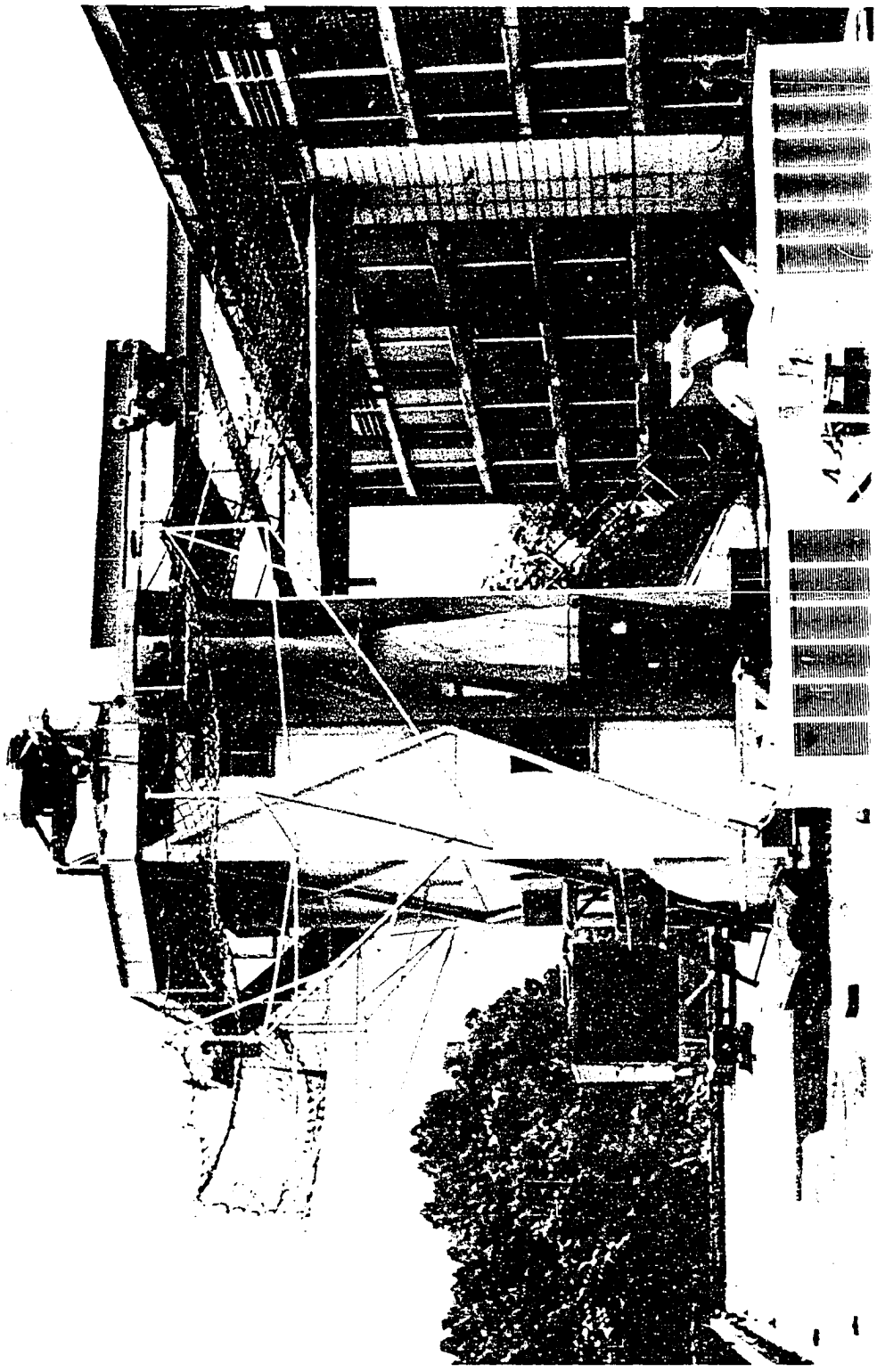

Figure 20. Far-field Receiving Equipment Room and Antenna Positioner

Reproduced with permission of the copyright owner. Further reproduction prohibited without permission.

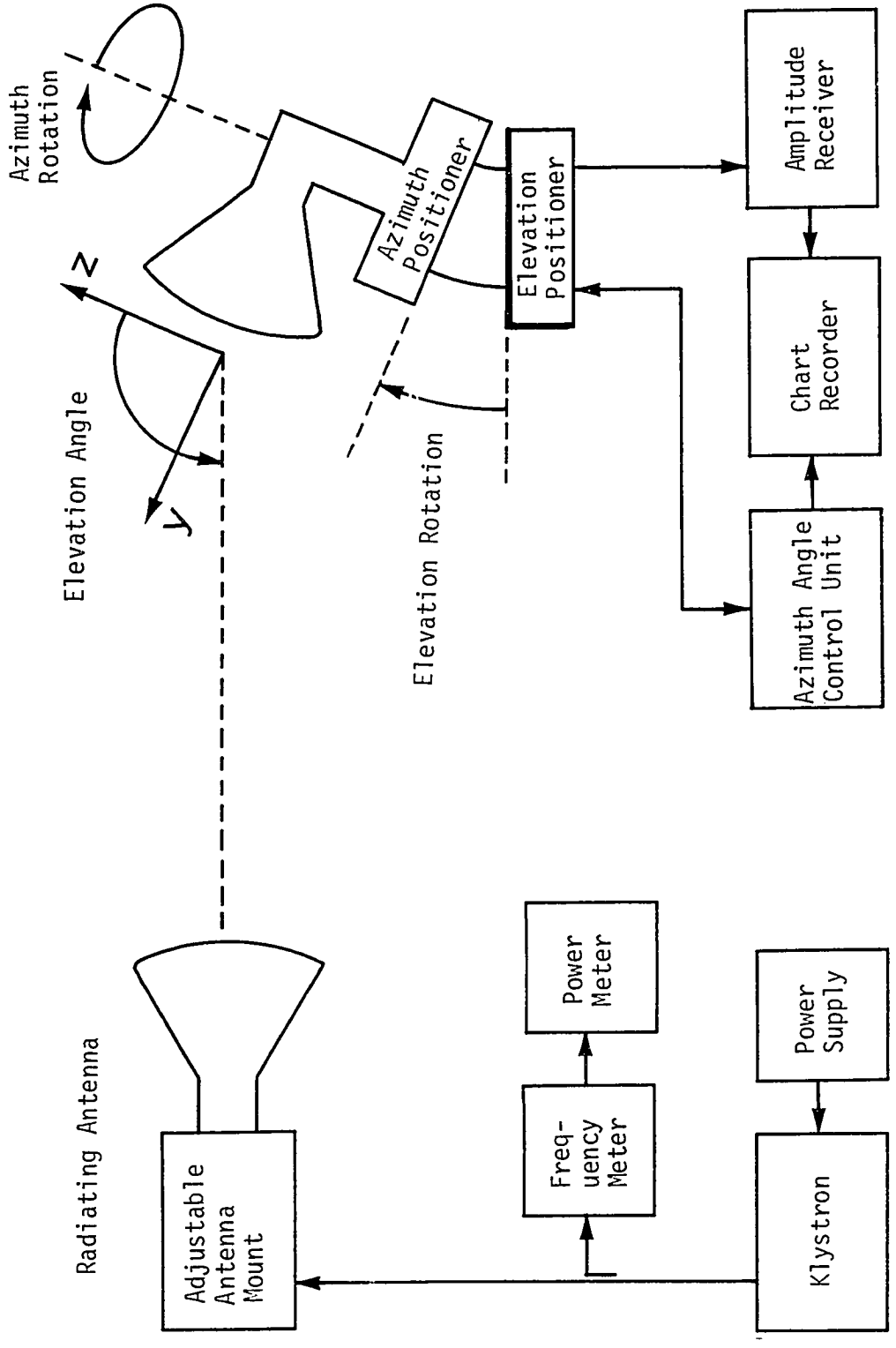

Figure 21. Schematic Diagram of the Far-field Measurement System

Reproduced with permission of the copyright owner. Further reproduction prohibited without permission.

beam of the transmitting atenna may be adjusted a few degrees in azimuth and in elevation with hand cranks mounted on the supporting structure of the antenna.

Reproduced with permission of the copyright owner. Further reproduction prohibited without permission.

CHAPTER IV

MEASUREMENTS AND FAR-FIELD CALCULATION

Detailed measured procedures are presented in this chapter for the four measurement systems described in Chapter III. The measurement procedure for each measurement system is basically the same and is divided into four parts.

First, the measurement system is mechanically aligned. A high degree of precision is required in this alignment as a distance of ten-thousandths of an inch at the operating frequency of 9.68 GHz corresponds to an electrical phase shift of approximately three degrees.

Second, stray radiation impinging at the receiving antenna is reduced below measurement capability. Absorbing material is used to cover all reflecting objects in the measurement area. Remaining reflectors are tested to determine if they are contributing stray radiation at the receiving antenna by means of the following absorption test: A set of measurements is taken for various positions of the receiving and transmitting antennas; the suspected reflector is covered with absorbing material and the measurements repeated. Any difference in the measurements indicate absorbing material is required to cover the reflector.

Third, the accuracy of the measurement system is determined. A worst case estimate of the overall system amplitude and phase accuracy is provided by the sum of the amplitude and phase errors due to mechanical alignment error, equipment and instrumentation error, and the microwave source amplitude and frequency drift.

Reproduced with permission of the copyright owner. Further reproduction prohibited without permission.

Fourth, a data collection procedure is established on the location and number of measurements to be taken, on the recording of data, and on the particular measurements to be used as repeatability check points. Having completed the measurements, the data is displayed in tables or graphs.

The measured data is used to calculate the far-field patterns of the two test antennas on a Univac 1108 digital computer. A block diagram of the computation process is given later in Figure 36, which features many possible variations of near-field probes, sample spacings, low-pass filter wavenumber limits, and wavenumber translations that may be used in the far-field determination.

Polarization Ratio Measurement

The xy-motion unit and the z-motion unit are mechanically aligned such that the z-axis of the z-motion is parallel to the earth and perpendicular to the xy-plane of the xy-motion unit. A precision bubble level is used to align the z-axis of the z-motion unit and the x-direction traverse bar of the xy-motion unit parallel to the earth with an accuracy of five arc-minutes. A precision clinometer is used to align the y-direction traverse bars of the xy-motion unit perpendicular to the earth with an accuracy of 30 arc-seconds. A transit and a precision square are used to set the z-axis of the z-motion unit perpendicular to the x-axis of the xy-motion unit with an accuracy of five arc-minutes.

Next, the receiving antenna is centered to an accuracy of two-thousandths of an inch in the rotary probe holder using a dial guage. The receiving and transmitting antennas are leveled with a small bubble level to an accuracy of five arc-minutes, and set to the same height above ground

Reproduced with permission of the copyright owner. Further reproduction prohibited without permission.

by bringing them together with the z-motion unit and adjusting the position of the receiving probe with the xy-motion unit.

The antennas are separated by a distance greater than the sum of their far-field distances and the absorption test is performed to eliminate stray radiation. To reduce stray radiation from the flanges of the probe antennas, a series of absorbing rings are placed around the waveguide near the flanges and around the flanges themselves. These same absorbing rings are used in all subsequent measurements involving the probe antennas.

The accuracy of the amplitude and phase measurements made with this system depends on the mechanical alignment of the transmitting and receiving antennas, the receiver accuracy, klystron amplitude and frequency drift, and the amplitude and phase changes occurring in the rotary joints. The error introduced by the misalignment of the receiving and transmitting antennas is difficult to analyze as all the probe antennas are nearly linearly polarized. The measured parallel component has a large amplitude and a phase which is insensitive to small changes in angle, making alignment relatively unimportant. The measured cross component, however, has a very low amplitude and a phase which varies rapidly with off-axis angle. The specified accuracy of the receiver is 0.05 dB in amplitude and 0.1 degree in phase.

The klystron was continuously monitored in amplitude and found not to vary more than 0.05 dB during the measurement. The klystron synchronizer is specified to maintain a frequency stability of one part in 10^6 for long term operation. To analyze the effect of a small frequency change on the relative phase difference between the received signal and the

Reproduced with permission of the copyright owner. Further reproduction prohibited without permission.

reference signal, the two electrical path lengths are calculated in wavelengths. The difference between the direct reference path from source to receiver and the source to transmitting antenna to receiving antenna to receiver path is approximately 700 wavelengths. An increase or decrease in frequency of one part in 10^6 produces a corresponding decrease or increase in the number of wavelengths of one part in 10^6, yielding a change of phase of $\pm 700 \times 10^{-6} \times 360 \approx \pm 0.25$ degree.

The amplitude and phase variation of each of the four rotary joints in the system were measured with the receiver and found to have a maximum of 0.05 dB amplitude variation and a maximum of 0.2 degrees phase variation at the operating frequency.

Excluding the error in amplitude and phase due to mechanical misalignment of the system, the total accuracy of this measurement system is estimated to be 0.3 dB in amplitude and 1.5 degrees in phase.

Two groups of three antennas are used in the polarization ratio measurement. The first group contains the far-field probe antenna, the small horn near-field probe, and the large horn near-field probe; the second group contains the far-field probe antenna, the large horn near-field probe and the open-ended waveguide near-field probe. Two of the three antennas in a group are mounted on axes facing each other, one as the receiving antenna and the other as the transmitting antenna. With their y-axes (see Figure 14) aligned, the relative amplitude and phase of the received signal is set to zero dB and zero degrees phase. The receiving antenna is then rotated so that its y-axis is aligned with the x-axis of the transmitting antenna, and the relative amplitude and phase of the received signal are recorded as Measurement #1 in Table 1. This

Reproduced with permission of the copyright owner. Further reproduction prohibited without permission.

Table 1. Polarization Ratio Measurement Data

Antennas Used (Probes)	Measurement #1		Measurement #2	
First Group	Amplitude (dB)	Phase (Degrees)	Amplitude (dB)	Phase (Degrees)
Large Horn - Far Field	-41.2	-162	-40.9	-162
Small Horn - Far Field	-31.4	-5	-30.9	-5
Small Horn - Large Horn	-35.5	+55	-35.5	+55
Second Group	Amplitude (dB)	Phase (Degrees)	Amplitude (dB)	Phase (Degrees)
Large Horn - Far Field	-42.2	-95	-42.1	-80
Open-ended Waveguide - Far Field	-37.4	-105	-38.2	-109
Open-ended Waveguide - Large Horn	-32.9	-160	-32.9	-160

Table 2. Calculated Polarization Ratio

Antenna Group	Measurement Number	Amplitude (dB)	Phase (Degrees)
First	#1	-39.7	-64.5
First	#2	-39.4	-61.5
Second	#1	-39.4	-37.3
Second	#2	-39.2	-32.0

Reproduced with permission of the copyright owner. Further reproduction prohibited without permission.

process is repeated three times, once for each pair of the three antennas. Each of the above measurements is repeated and recorded in Table 1 as Measurement #2 and repeated for the second group of three antennas. The calculated polarization ratios of the far-field probe antenna, are given in Table 2.

Probe Measurement

The three axes of mechanical rotation, the azimuth rotation axis, the elevation rotation axis, and the far-field component rotation axis are aligned so as to intersect perpendicularly thus establishing a spherical coordinate system of rotation. The three rotary joints corresponding to the three axes of rotation are centered with an accuracy of two-thousandths of an inch, within their respective rotation units with a dial guage. The elevation axis of rotation is used as the reference for the other two axes, and is leveled from a reference level set with a precision bubble level having an accuracy of five arc-minutes. The pinhole of a pinhole telescope is aligned with the axis of elevation rotation to an accuracy of two-thousandths of an inch with a dial guage. With the elevation carriage at zero degrees elevation, a plumb bob is hung from the center of the rotary far-field probe holder and is used to crudely align the rotation axis of the azimuth turntable to within one-tenth of an inch.

A special alignment jig, seven inches in length with a one-sixteenth inch diameter shaft mounted vertically at its end, is fitted to the near-field probe mount of the azimuth turntable. With the aid of a dial guage the one-sixteenth inch diameter shaft is aligned concentric to the azimuth axis of rotation. This same shaft is then sighted through the pinhole

Reproduced with permission of the copyright owner. Further reproduction prohibited without permission.

telescope and the location of the azimuth turntable adjusted to make the shaft appear stationary as the azimuth turntable is rotated.

The far-field probe is aligned concentric with the axis of far-field component rotation to an accuracy of two-thousandths of an inch with a dial guage. With the elevation carriage in its 90.0 degree position, the far-field probe holder unit is adjusted to make the far-field probe level using a small bubble level with an accuracy of five arc-minutes.

The open-ended waveguide near-field probe is installed replacing the special alignment jig. The well-defined phase centers of the open-ended waveguide are used for final adjustment of the location of the near-field probe and azimuth turntable. The position of the open-ended waveguide probe and azimuth turntable is adjusted to produce a constant phase pattern in the 90.0 degree elevation far-field cut, and a symmetric phase pattern in the 90.0 degree azimuth far-field cut. The near-field probe is then leveled with a small bubble level to an accuracy of five arc-minutes, and the electrical alignment repeated.

The total positional accuracy of the mechanical alignment is approximately five-thousandths of an inch and total angular accuracy is 0.3 degrees.

Stray radiation is minimized using the absorption test and the absorbing rings on the probe antennas.

The accuracy of the amplitude and phase measurements of this system depends on the mechanical alignment of the system, the receiver accuracy, the drift in amplitude and frequency of the klystron, and the amplitude and phase changes occurring in the rotary joints. The amplitude changes

Reproduced with permission of the copyright owner. Further reproduction prohibited without permission.

due to the mechanical misalignment of five thousandths of an inch are small in comparison to the phase change of 1.5 degrees. The specifications of the receiver accuracy are 0.05 dB and 0.1 degree phase as before.

The amplitude of the klystron is monitored throughout the measurements and found to vary not more than 0.2 dB. As the klystron is phase-locked to a crystal, the frequency is held constant to one part in 10^6 for long term operation. The electrical path length difference between the reference path from the source to receiver and the signal path from the source to transmitting antenna to receiving antenna to approximately 300 wavelengths corresponding to phase error of $\pm$ 0.11 degree with the above frequency change.

The rotary joints are measured with the receiver and found to have a constant transmission coefficient to within 0.5 dB and 0.2 degree phase. The total accuracy of the system is, therefore, estimated to be 0.35 dB in amplitude and 2.5 degrees in phase.

All large amplitude measurements taken with this system have a repeatability of 0.1 dB in amplitude and one degree in phase, and low amplitude (below -30 dB) measurements have a repeatability of one dB in amplitude and five degrees in phase.

Continuous analog amplitude and phase data of the elevation and azimuth components of the far-field patterns of the probe antennas are taken as a function of azimuth angle for constant values of elevation angle. The elevation angle is varied in five degree increments from an elevation angle of 30.0 degrees to 150.0 degrees. The azimuth angle varies continuously and linearly from 10.0 degrees to 170.0 degrees. At

Reproduced with permission of the copyright owner. Further reproduction prohibited without permission.

the start of every other azimuth sweep the elevation angle is set to 90.0 degrees and the azimuth angle is set to 90.0 degrees, the far-field probe is rotated to receive the elevation component, and a reference check of amplitude and phase is made. This process is repeated for each of the three near-field probes.

Figures 22, 23, and 24 show the measured amplitude and phase of the elevation and azimuth components of the far fields of the open-ended waveguide probe, the small horn probe, and the large horn probe, respectively. The base coordinates for all graphs are the far-field azimuth angle and elevation angle. The ordinate for the amplitude graphs is decibels and the range from zero to -60 dB. The ordinate for the phase graphs is degrees of phase and range from zero to 360 degrees.

Near-Field Measurement

The z-axis of the z-motion unit is aligned parallel to the earth and perpendicular to the x-axis of the xy-motion unit as described for the polarization measurement system. An optical target is mounted on the side of the rotary probe holder and a precision transit is aligned in an xy-plane of the xy-motion unit such that the optical target appears at the same point in the transit sight at each end of the x-traverse of the rotary probe holder. With the transit level, an elevation sweep of the transit sight then forms an xy-plane perpendicular to the earth and contains the x-axis of the xy-motion unit. The xy-motion unit is further adjusted to make the optical target appear at the same point of the transit sight at each of the four corners of the 100 by 100 inch measurement area. Using the transit, the deviation of the probe location from a true plane is recorded throughout the measurement area at the intersections of a square

Reproduced with permission of the copyright owner. Further reproduction prohibited without permission.

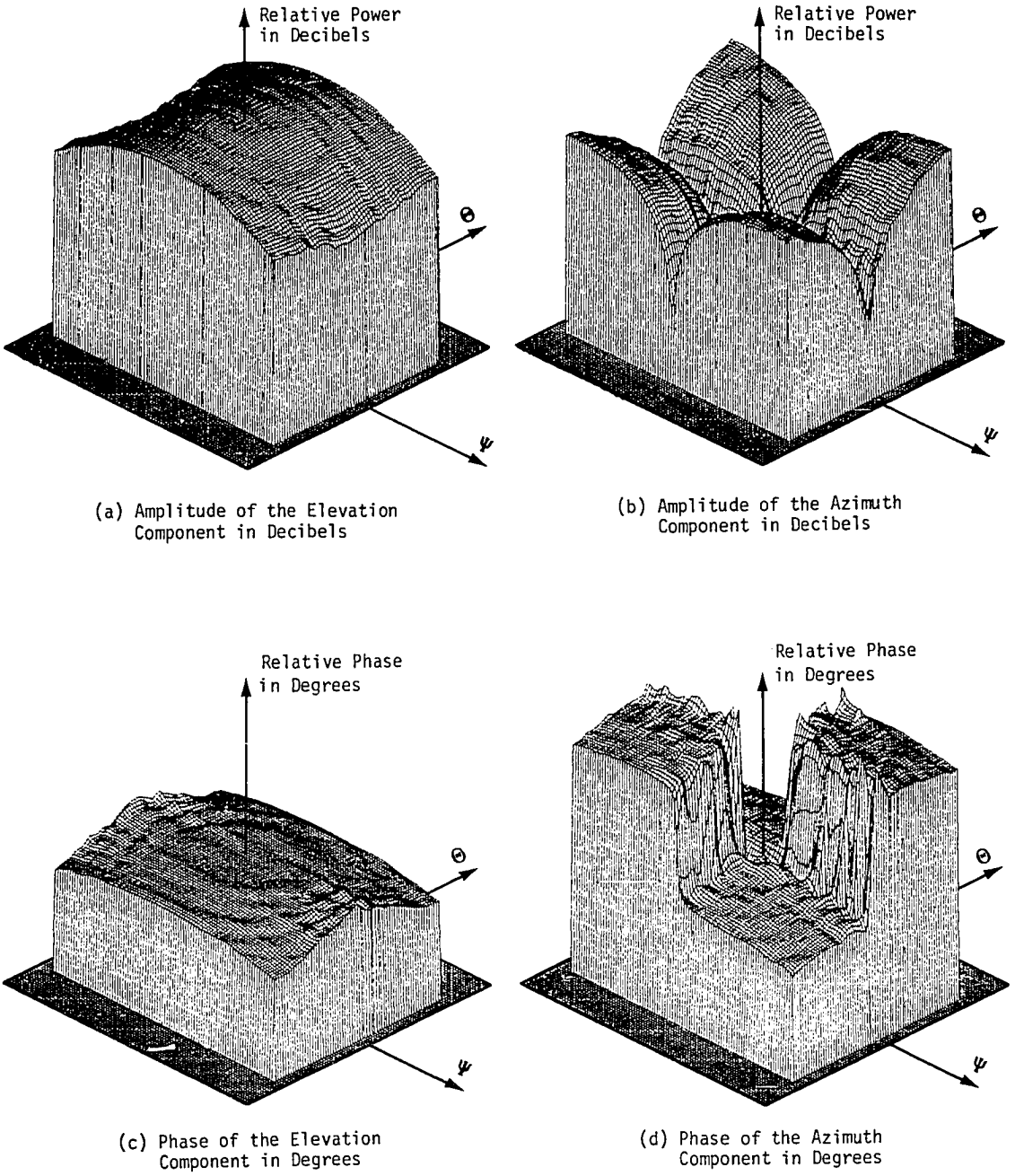

(a) Amplitude of the Elevation Component in Decibels

(b) Amplitude of the Azimuth Component in Decibels

(c) Phase of the Elevation Component in Degrees

(d) Phase of the Azimuth Component in Degrees

Θ = Elevation Angle

Ψ = Azimuth Angle

Figure 22. Measured Far-field Amplitude and Phase Patterns of the Open-ended Waveguide Probe

Reproduced with permission of the copyright owner. Further reproduction prohibited without permission.

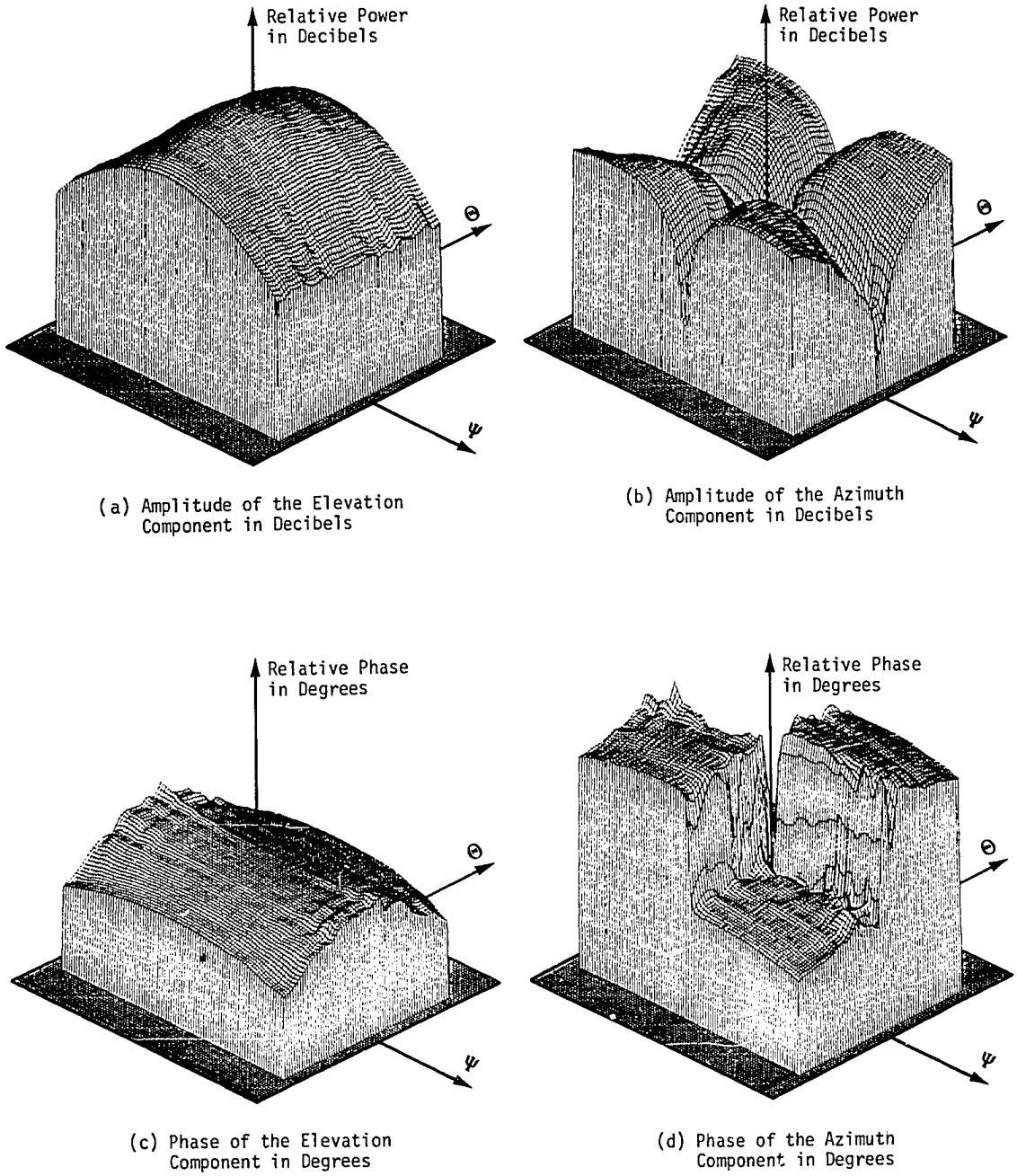

(a) Amplitude of the Elevation Component in Decibels

(b) Amplitude of the Azimuth Component in Decibels

(c) Phase of the Elevation Component in Degrees

(d) Phase of the Azimuth Component in Degrees

Θ = Elevation Angle

Ψ = Azimuth Angle

Figure 23. Measured Far-field Amplitude and Phase Patterns of the Small Horn Probe

Reproduced with permission of the copyright owner. Further reproduction prohibited without permission.

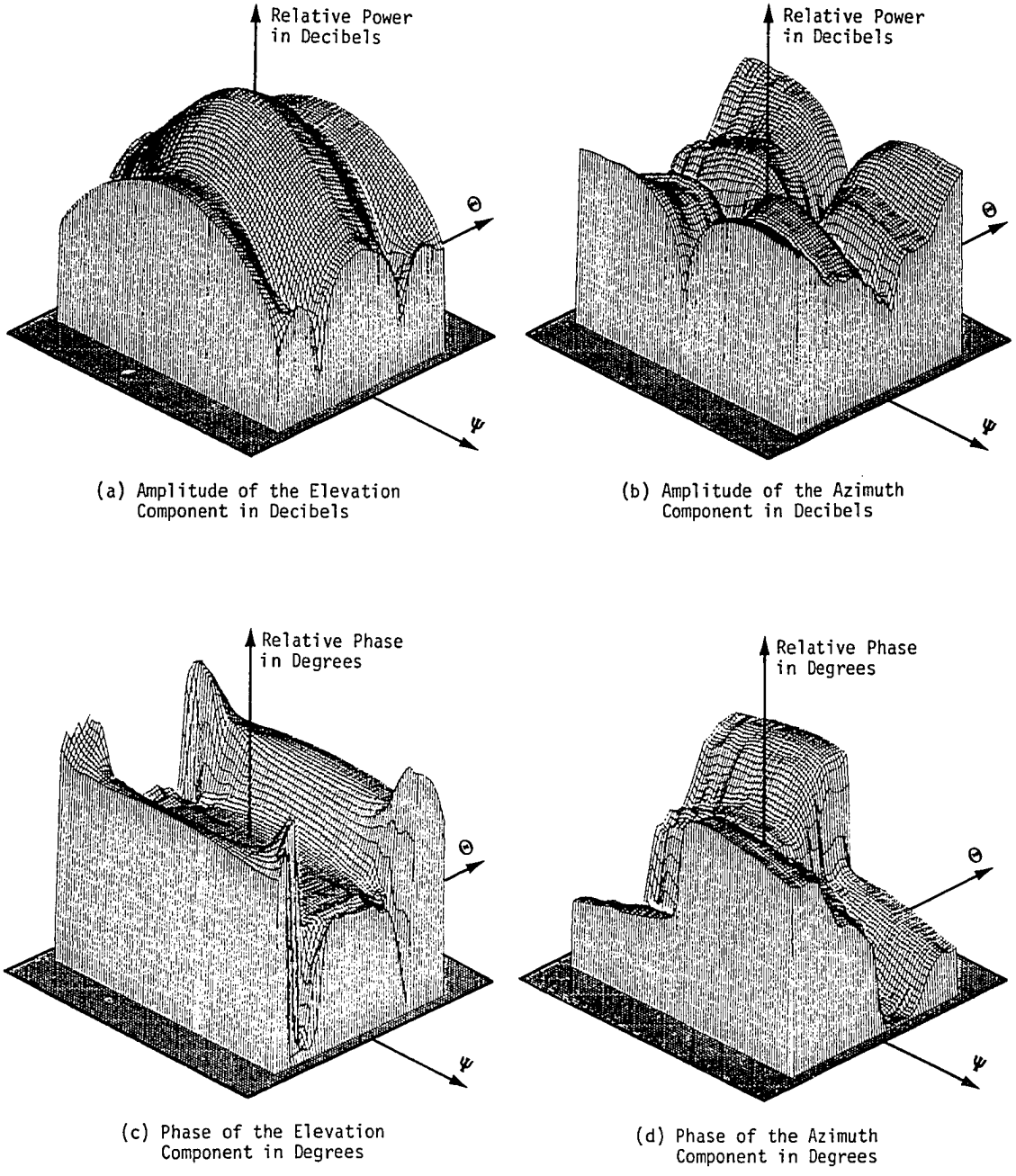

(a) Amplitude of the Elevation Component in Decibels

(b) Amplitude of the Azimuth Component in Decibels

(c) Phase of the Elevation Component in Degrees

(d) Phase of the Azimuth Component in Degrees

Θ = Elevation Angle

Ψ = Azimuth Angle

Figure 24. Measured Far-field Amplitude and Phase Patterns of the Large Horn Probe

Reproduced with permission of the copyright owner. Further reproduction prohibited without permission.

lattice, five inches in horizontal and vertical spacings, with an accuracy of five-thousandths of an inch. Figure 25 is a graph of the z-position error of the rotary probe holder in thousandths of an inch. The maximum error is found to be 40-thousandths of an inch. The error graph is tabulated and used to correct probe position information as part of the far-field computation process.

The near-field probes are leveled in the rotary probe holder and centered within the rotary probe holder as in the polarization measurement. The transmitting test antenna is mounted together with its mount on the z-motion unit and aligned with the z-axis of the z-motion unit with an accuracy of 0.1 degree. The transmitting antenna is then moved with the xyz-control and position indicator unit to adjust the distance between the mouth of the near-field probe and the closest point of the test antenna to 10.0 inches. The accuracy of the z-position of the z-motion unit and the xy-position of the xy-motion unit is given by the manufacturer as 25-thousandths of an inch and is read directly from servo positioned dials on the control and indicator unit.

Stray radiation is substantially reduced through application of the absorption test and use of absorbing rings on the near-field probes. A photograph of the xy-motion unit, the z-motion unit, a near-field probe mounted in the rotary probe holder, and a test antenna is given in Figure 26. Extensive use of absorbing material is to be noted in the photograph.

The accuracy of the amplitude and phase measurements made with the near-field measurement system depends on the mechanical alignment accuracy of the system, the mechanical positional accuracy of the near-field probe,

Reproduced with permission of the copyright owner. Further reproduction prohibited without permission.

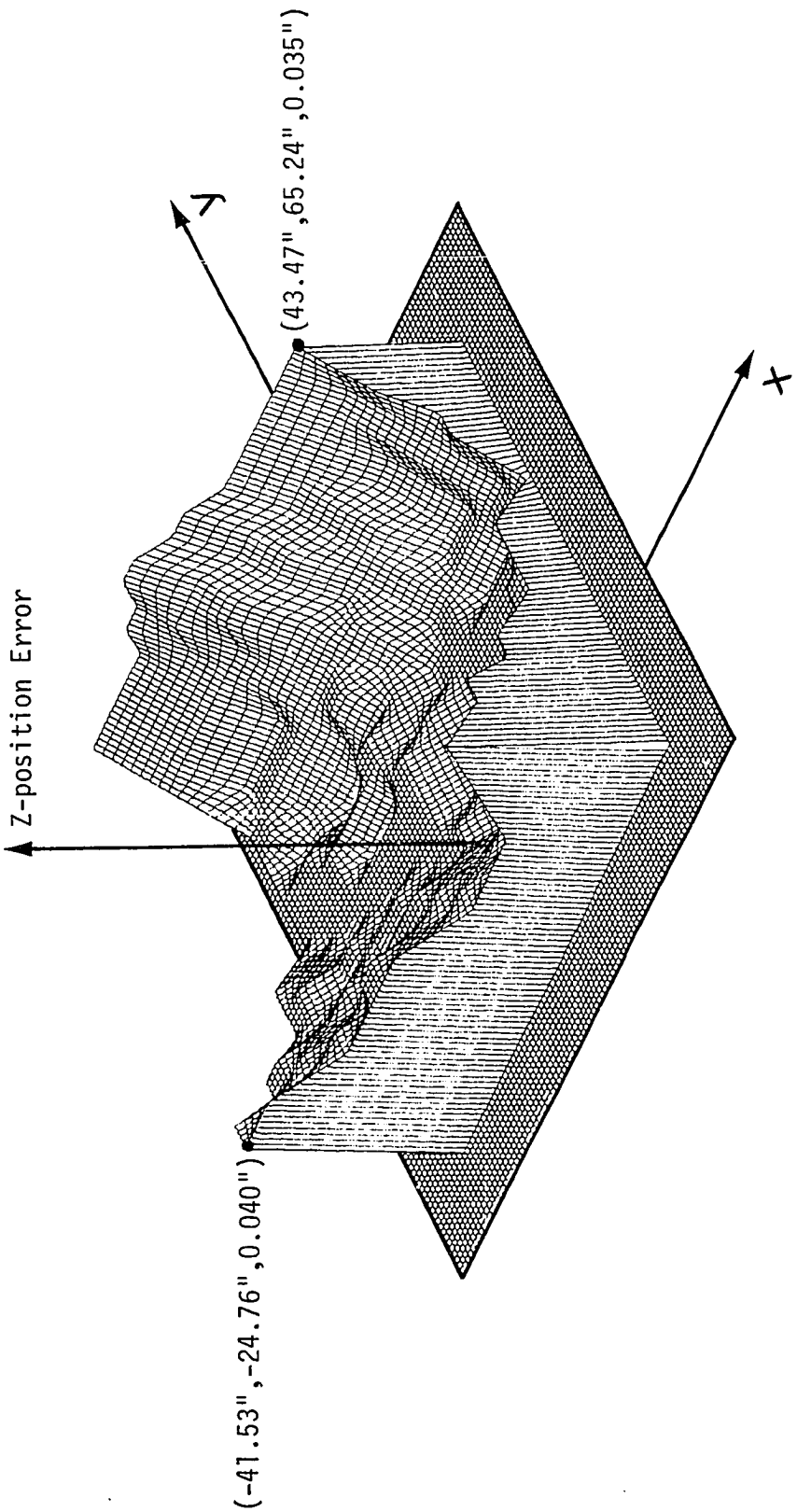

Figure 25. Z-position Error of the Near-field Measurement Plane

Reproduced with permission of the copyright owner. Further reproduction prohibited without permission.

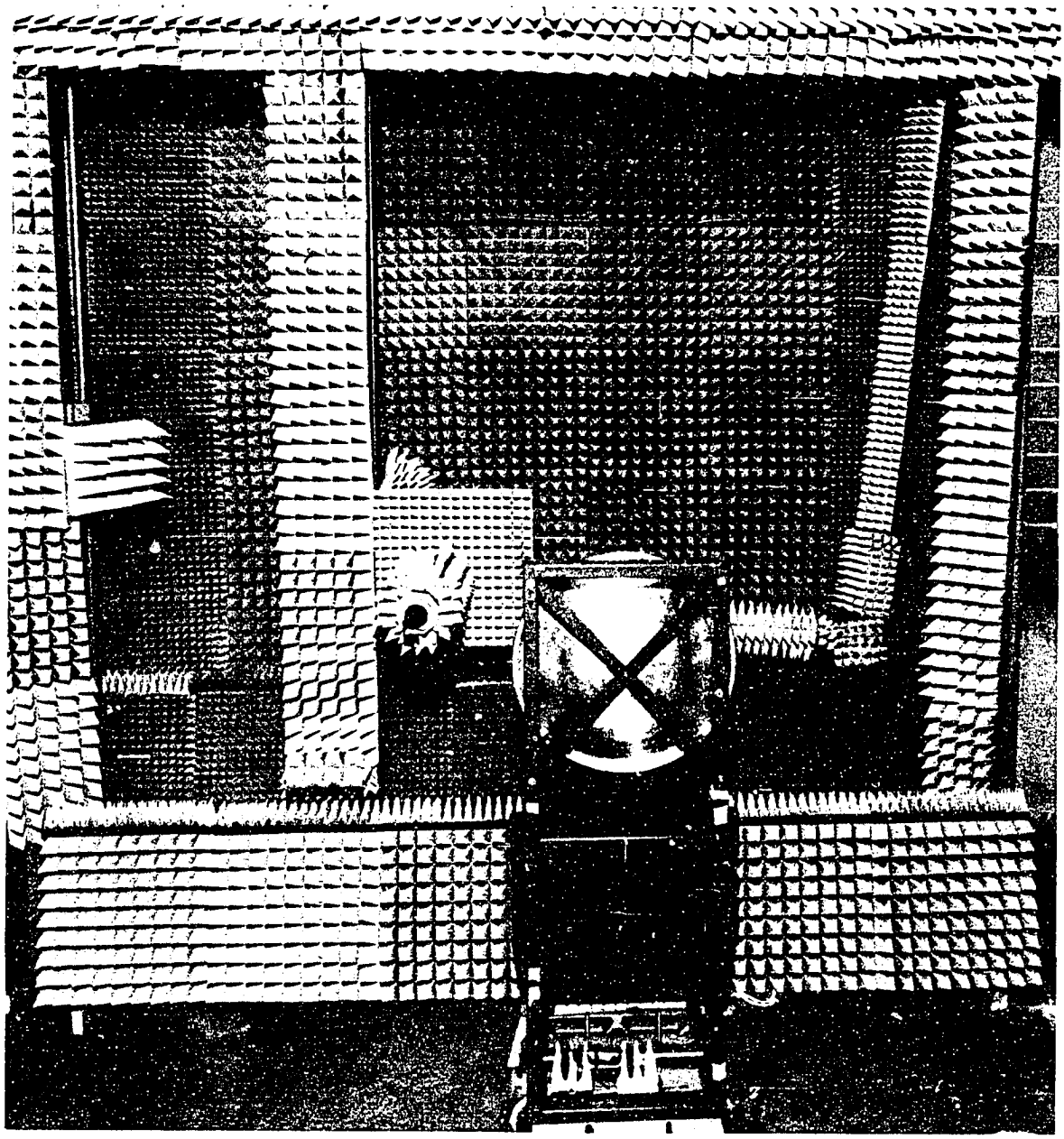

Figure 26. Near-field Measurement Area

Reproduced with permission of the copyright owner. Further reproduction prohibited without permission.

the receiver amplitude and phase detection accuracy, the stability of the amplitude and frequency of the klystron, and the amplitude and phase changes of the signals passing through the rotary joints. These factors, which influence measurement accuracy, are identical to those of the polarization measurement system except for the additional positional accuracy of the near-field probe. To estimate this additional error, it is assumed that the z-position error is the only error which affects the phase measurements significantly. This error is estimated to be five-thousandths of an inch, after correction of the measured data using the z-position error graph of Figure 25. The total accuracy of the near-field measurement system is, therefore, estimated to be 0.3 dB in amplitude and three degrees in phase. The repeatability of amplitude and phase measurements for signals having an amplitude greater than -40 dB is 0.2 dB in amplitude and three degrees in phase.

Amplitude and phase data of the x- and y-components of the near field of the test antenna are recorded in analog form as a continuous function of the x-position of the near-field probe for fixed y positions. The y position is incremented in one-third wavelength steps for a total of 128 steps. The total measurement area is a 53.1 by 53.1 inch area, centered about the geometrical center of the test antenna. As the calculated far-field phase patterns of the test antennas are not compared to measured far-field phase patterns, the exact location of the center is not important. Another channel of the recorder records the x-position voltage, as previously described, and provides accurate identification of the beginning and ending points of x-position data.

Using a stable low frequency oscillator and the servo position

Reproduced with permission of the copyright owner. Further reproduction prohibited without permission.

indicators of a Scientific Atlanta Series 4100 Rectangular Recorder, a graph of position versus time was made for a constant speed setting of the control unit. Figure 27 shows graphs of the difference between the true position versus time, and a superimposed linear relationship of position versus time. These error graphs are tabulated and are used to determine the true x position of the near-field probe. Figure 27(a) is the positional error for motion in the positive x direction. Figure 27(b) is the positional error for motion in the negative x direction. The near-field measurement procedure is repeated for the three near-field probes and the two test antennas.

Figures 28 through 33 show the near-field amplitude and phase data of the x and y components of the near fields of the two test antennas. The base coordinates for all graphs are the x and y coordinates within the near-field measurement plane. The ordinate for the amplitude measurement data is decibels and ranges from zero to -40 dB. The ordinate for the phase measurement data is degrees of phase and ranges from zero to 360 degrees. The ordinate of the measured phase data is compressed to allow better visualization of the regions of slowly changing phase.

Far-Field Measurement

The transmitting antenna of the Georgia Tech far-field measurement range is aligned to illuminate the receiving antenna with the peak of the main beam of the transmitting antenna. A test antenna is mounted together with its mount on the receiving antenna positioner and aimed approximately in the direction of the transmitting antenna. The receiving antenna is connected, via a mixer and a rotary joint, to the receiver. The amplitude output of the receiver is monitored as the direction of the transmitting

Reproduced with permission of the copyright owner. Further reproduction prohibited without permission.

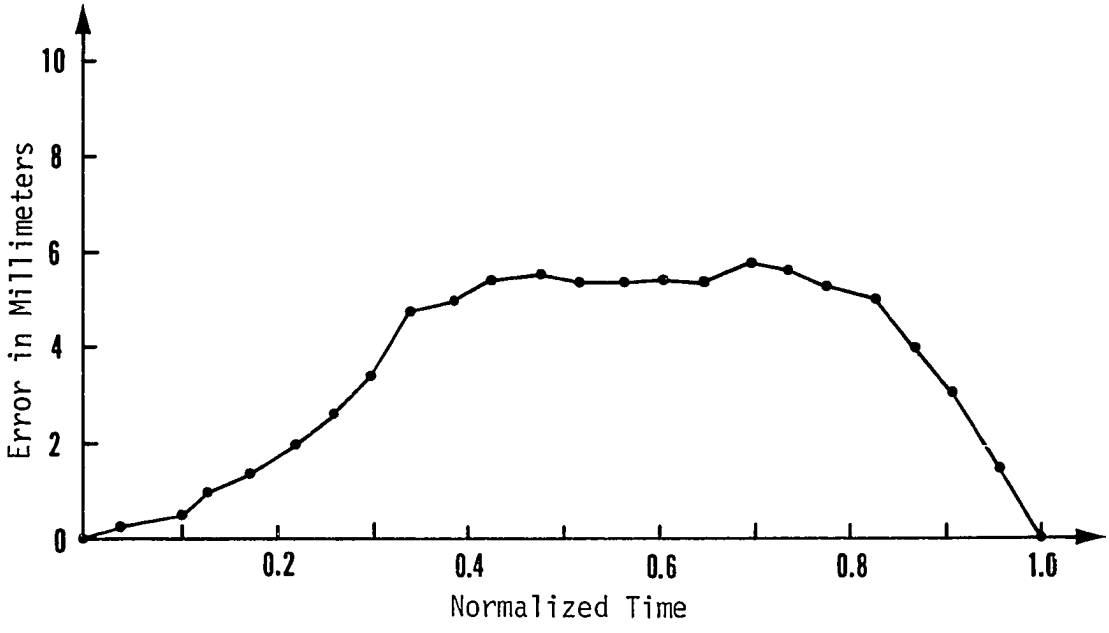

(a) Travel in the Positive X Direction

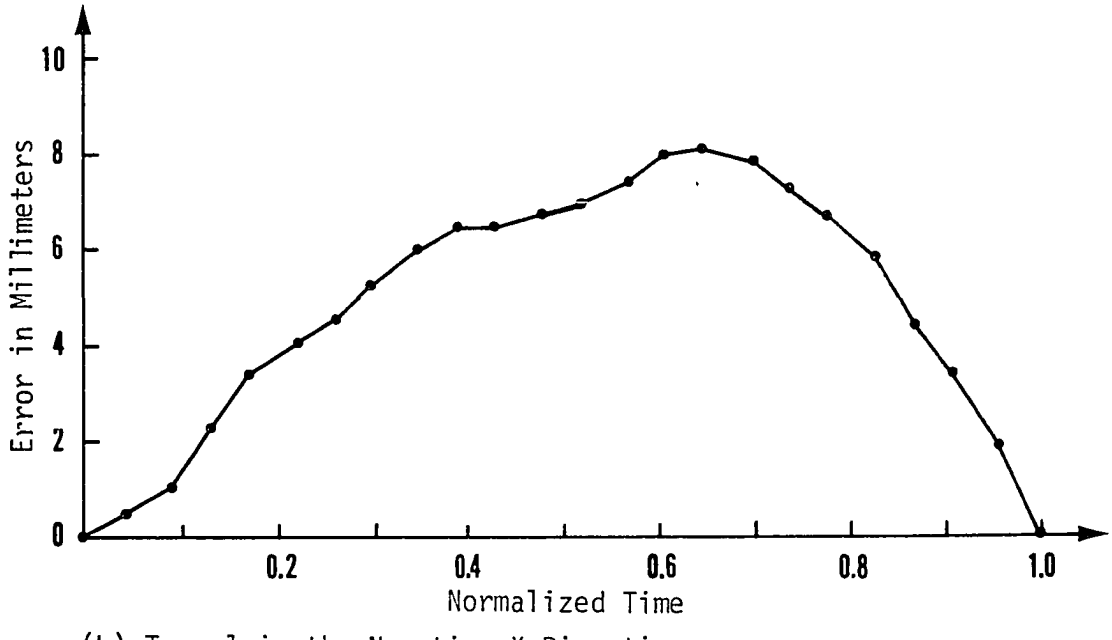

(b) Travel in the Negative X Direction

Figure 27. X-position Error Versus Normalized Time of the XY-motion Unit

Reproduced with permission of the copyright owner. Further reproduction prohibited without permission.

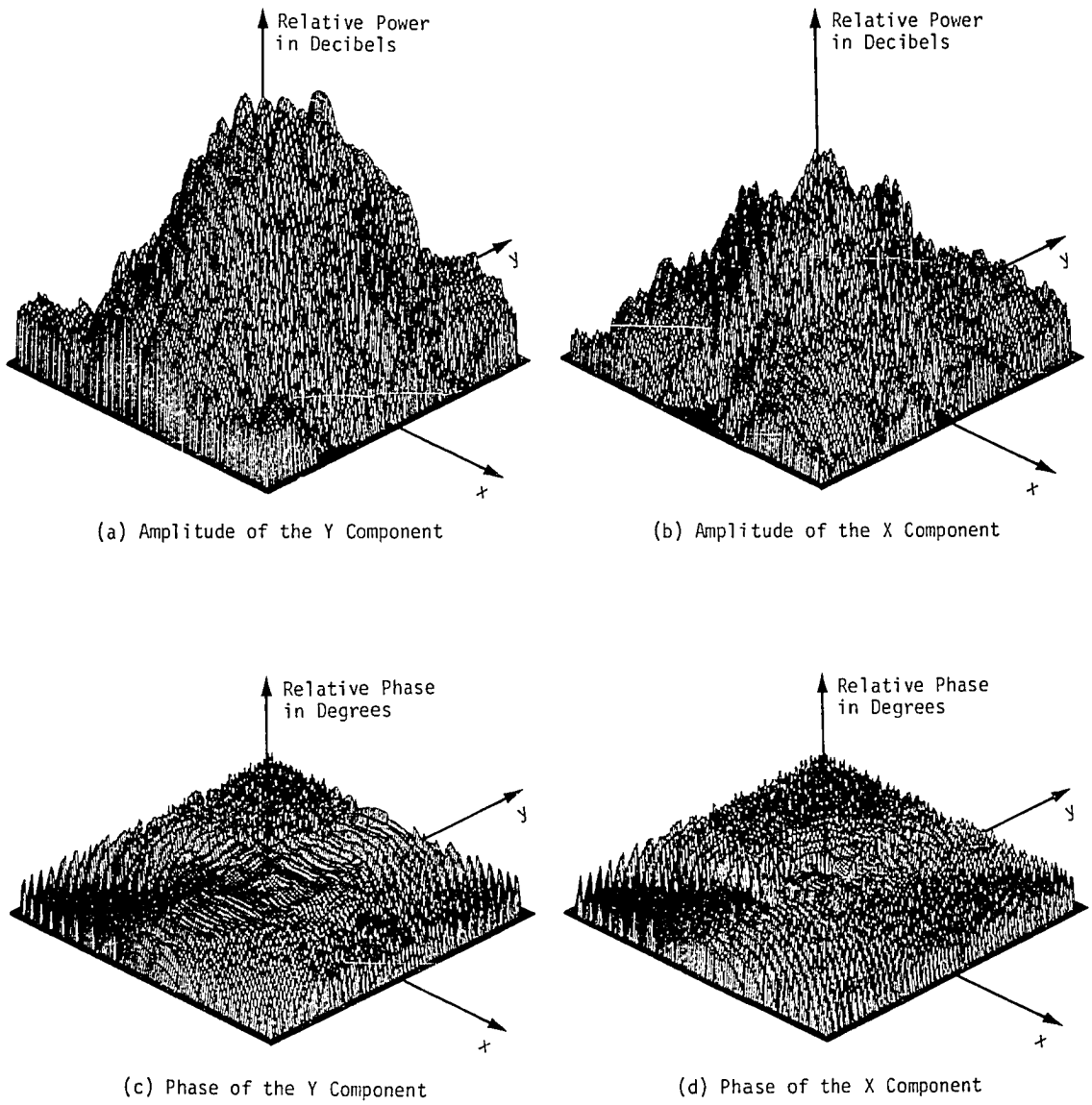

(a) Amplitude of the Y Component

(b) Amplitude of the X Component

(c) Phase of the Y Component

(d) Phase of the X Component

Figure 28. Near-field Amplitude and Phase Patterns of the Large Test Antenna as Measured with the Open-ended Waveguide Probe

Reproduced with permission of the copyright owner. Further reproduction prohibited without permission.

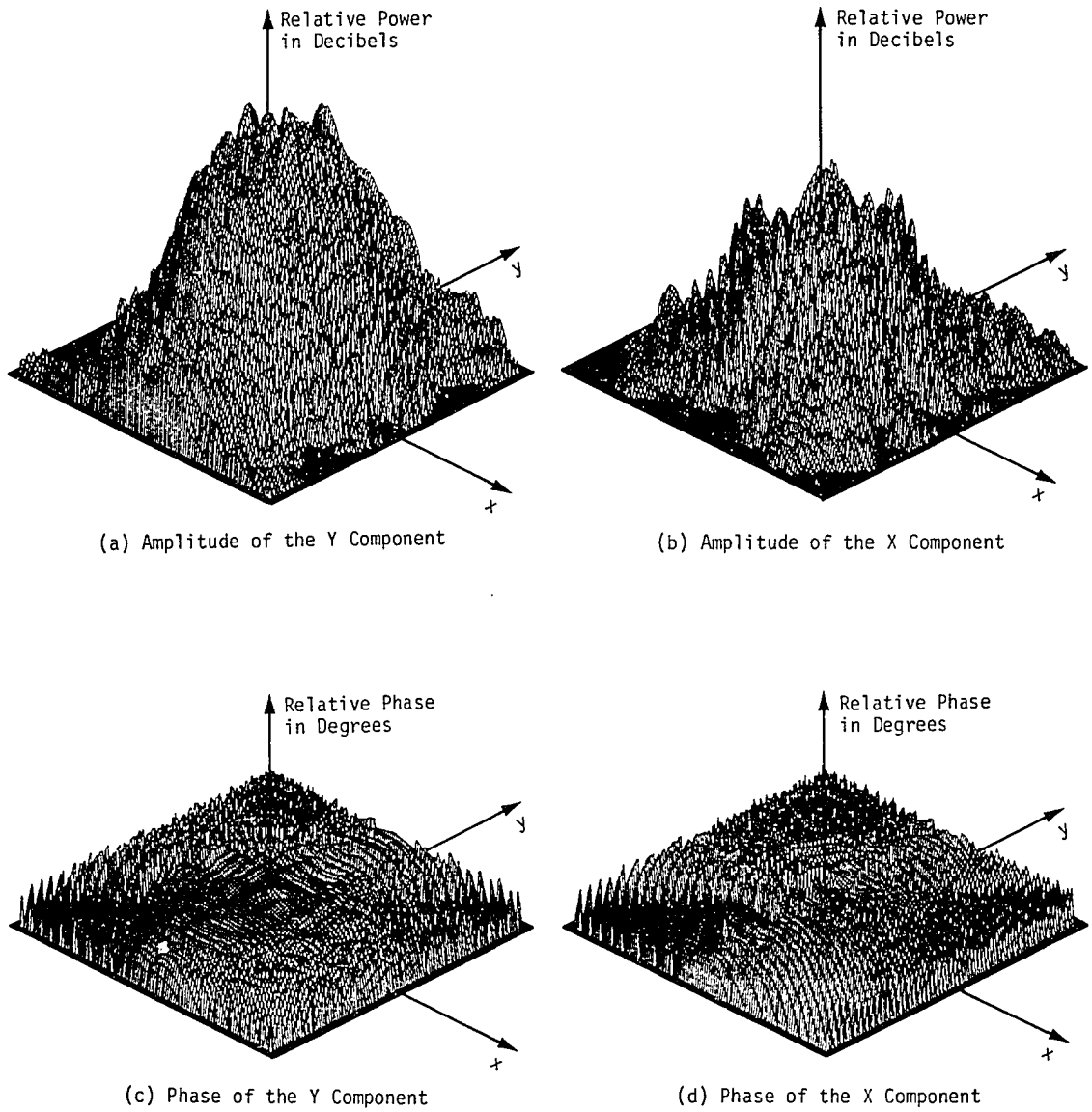

(a) Amplitude of the Y Component

(b) Amplitude of the X Component

(c) Phase of the Y Component

(d) Phase of the X Component

Figure 29. Near-field Amplitude and Phase Patterns of the Large Test Antenna as Measured with the Small Horn Probe

Reproduced with permission of the copyright owner. Further reproduction prohibited without permission.

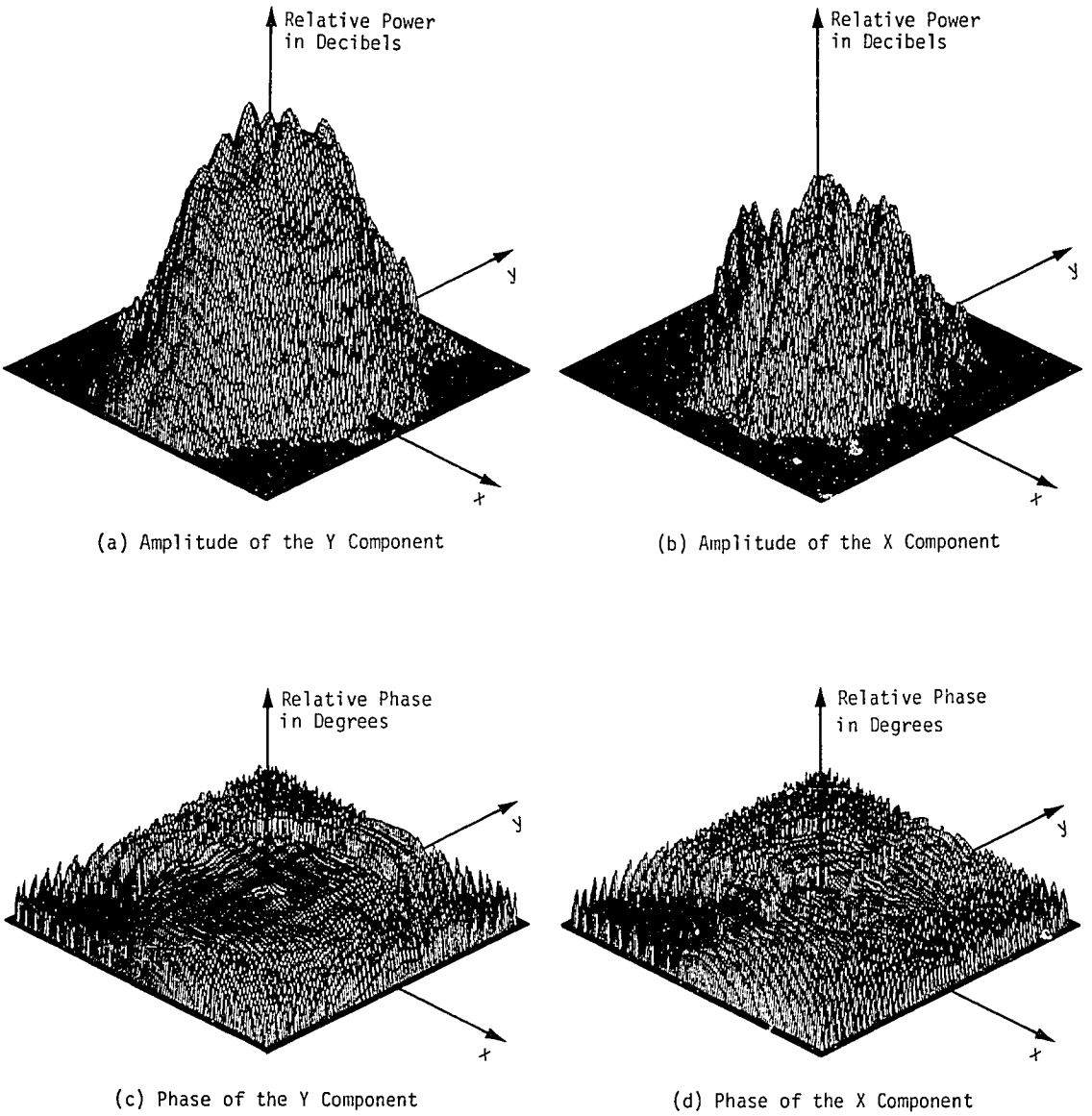

(a) Amplitude of the Y Component

(b) Amplitude of the X Component

(c) Phase of the Y Component

(d) Phase of the X Component

Figure 30. Near-field Amplitude and Phase Patterns of the Large Test Antenna as Measured with the Large Horn Probe

Reproduced with permission of the copyright owner. Further reproduction prohibited without permission.

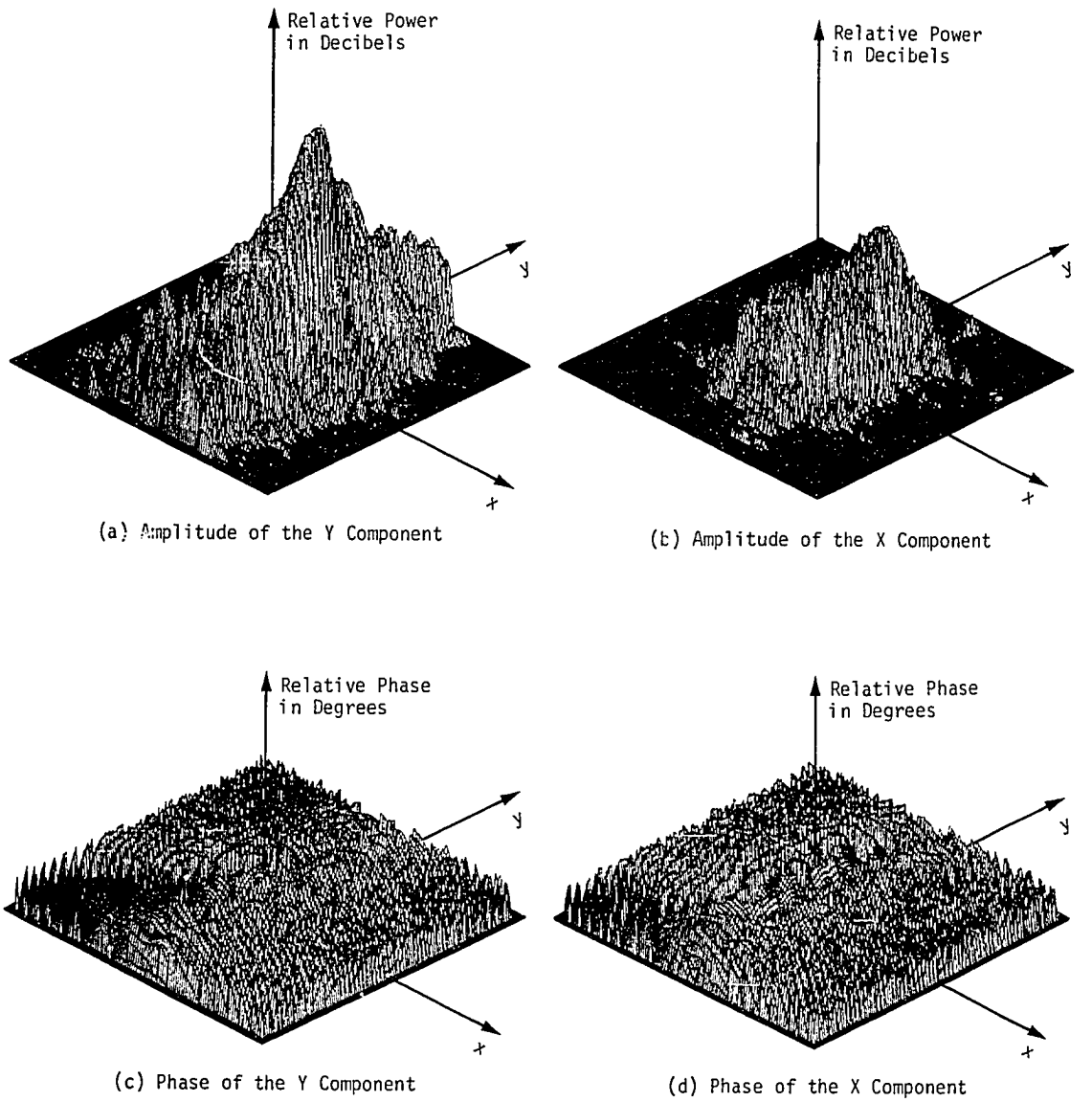

(a) Amplitude of the Y Component

(b) Amplitude of the X Component

(c) Phase of the Y Component

(d) Phase of the X Component

Figure 31. Near-field Amplitude and Phase Patterns of the Small Test Antenna as Measured with the Open-ended Waveguide Probe

Reproduced with permission of the copyright owner. Further reproduction prohibited without permission.

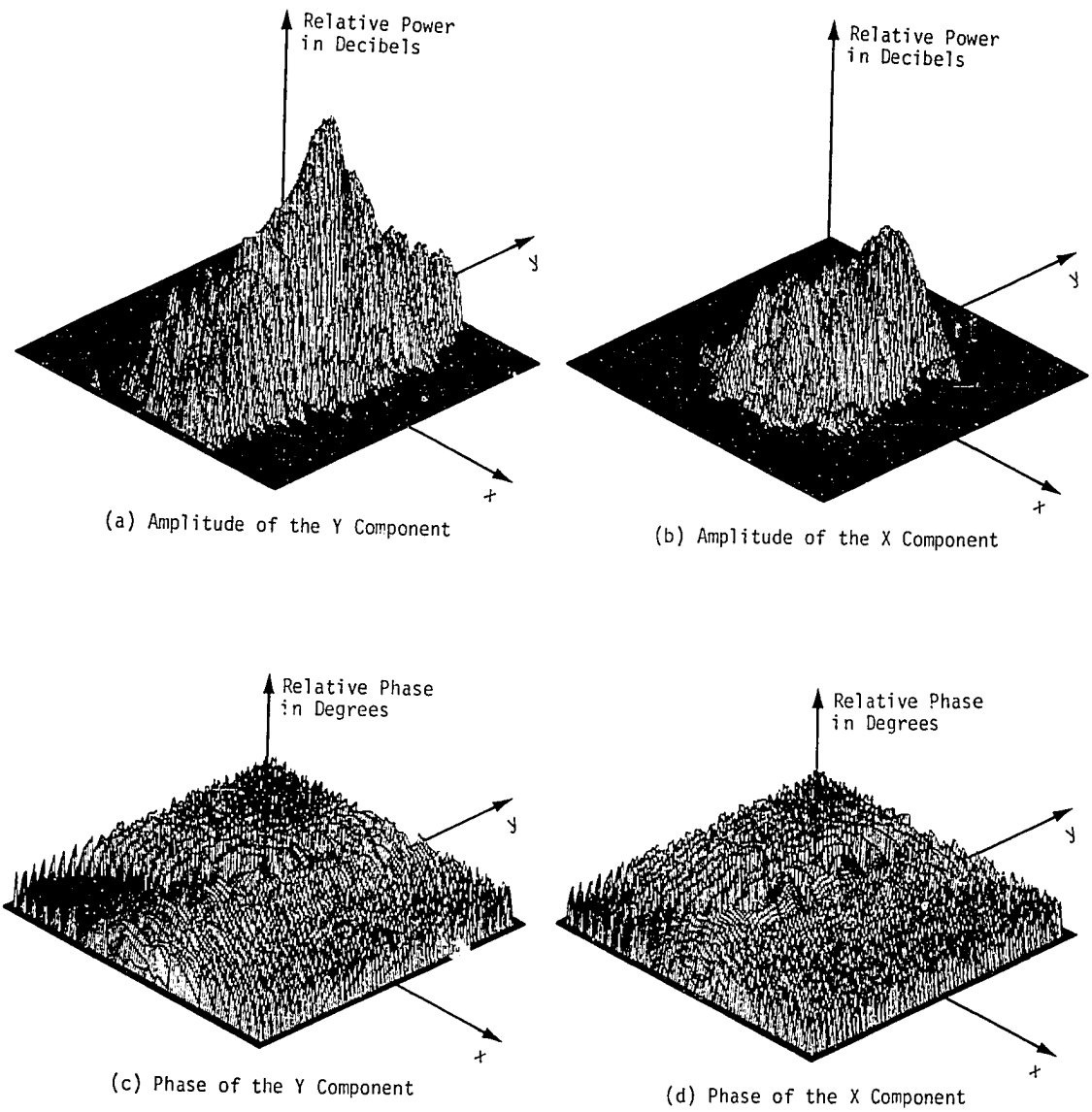

(a) Amplitude of the Y Component

(b) Amplitude of the X Component

(c) Phase of the Y Component

(d) Phase of the X Component

Figure 32. Near-field Amplitude and Phase Patterns of the Small Test Antenna as Measured with the Small Horn Probe

Reproduced with permission of the copyright owner. Further reproduction prohibited without permission.

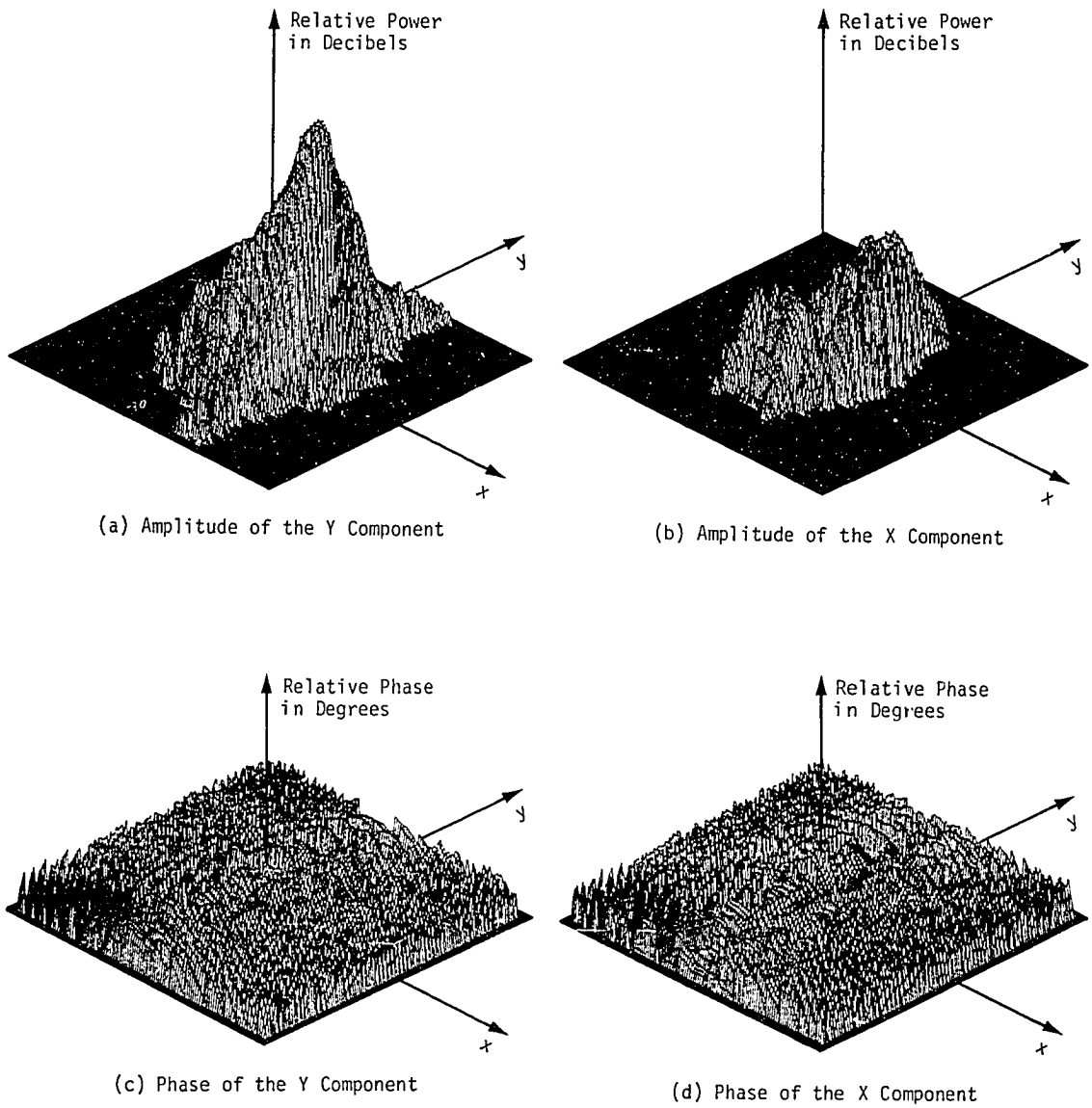

(a) Amplitude of the Y Component

(b) Amplitude of the X Component

(c) Phase of the Y Component

(d) Phase of the X Component

Figure 33. Near-field Amplitude and Phase Patterns of the Small Test Antenna as Measured with the Large Horn Probe

Reproduced with permission of the copyright owner. Further reproduction prohibited without permission.

antenna is adjusted for maximum received amplitude. The direction of the receiving antenna is then adjusted for maximum received amplitude and the entire adjustment process repeated until the true maximum is found.

Reference directions for the receiving antennas are established by optical alignment of the test antenna mount with the center of the transmitting antenna.

Other elevation angles are set using a bubble level mounted inside a graduated protractor to an accuracy of 0.3 degrees. The azimuth angle is varied continuously with the servo control and indicator unit.

Stray radiation due to ground reflection, tree and building reflection cannot be eliminated in the usual manner, as the cost of absorbing material to cover such an area is prohibitive.

The amplitude measurement accuracy of this system is dependent on the stray radiation level, the receiver accuracy, the klystron amplitude drift, and the change in the amplitude of the received signal as it passes through the rotary joint. The receiver is specified to have an amplitude measurement accuracy of 0.05 dB, and the specified amplitude variation of the rotary joint is 0.05 dB. The amplitude drift of the klystron was checked periodically throughout the measurements and found to be less than 0.3 dB.

To determine the level of stray radiation, each cut of the far-field pattern is repeated with the antenna upside-down. A difference in the two patterns indicates the presence of stray radiation. The difference between the two sets of measured patterns is shown as error bars on all measured far-field patterns.

The far-field amplitude patterns of the two test antennas are

Reproduced with permission of the copyright owner. Further reproduction prohibited without permission.

recorded for continuous azimuth angles from 30 degrees to 150 degrees and for fixed values of elevation angle. The elevation angle is varied in one-degree increments from 81 degrees to 99 degrees. At the beginning of every other azimuth sweep, the test antenna is positioned for maximum signal; an amplitude drift check is made, and the receiver is adjusted to compensate for the drift. To determine the repeatability of the measurement system, each pattern is recorded four times, twice in the normal configuration and twice in the upside-down configuration. From these measurements the repeatibility is determined to be 1 dB. Typical far-field amplitude patterns for the large test antenna are shown in Figure 34 and for the small test antenna in Figure 35.

Far-field Calculation

The calculation of the far-field power patterns of the two test antennas is performed on Georgia Tech's Univac 1108 digital computer. The input data for the computation process consists of the measured transverse vector near fields of the two test antennas, the measured far fields of the three probe antennas, the polarization ratio of the far-field probe antenna, the z position error of the xy-motion unit and x position versus time error of the x-motion of the xy-motion unit. The measured near-field data of the two test antennas and the measured far-field data of the three probe antennas are converted from their original analog form to digital form on a Radiation Model 5020 Analog to Digital Converter. The digital form of the near-field and far-field data is recorded on digital magnetic tape and stored in the computer tape library. The polarization ratio of the far-field probe, the x position error, and the z position error are in tabular form and are stored on computer cards.

Reproduced with permission of the copyright owner. Further reproduction prohibited without permission.

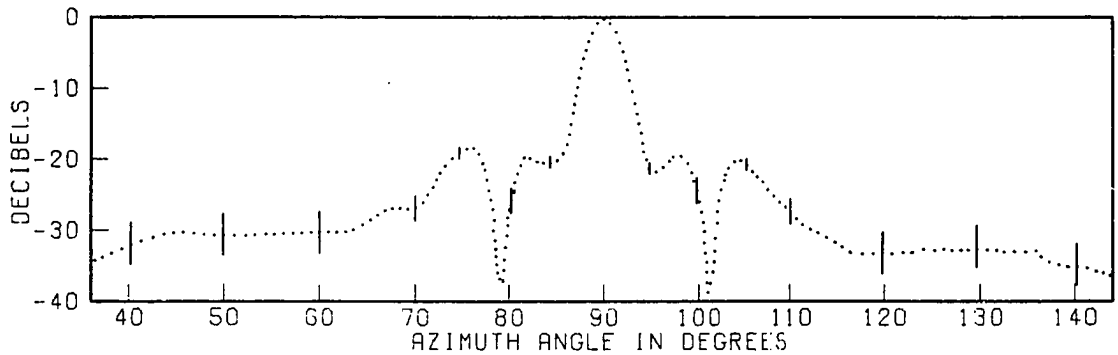

(a) 90 Degree Elevation Angle

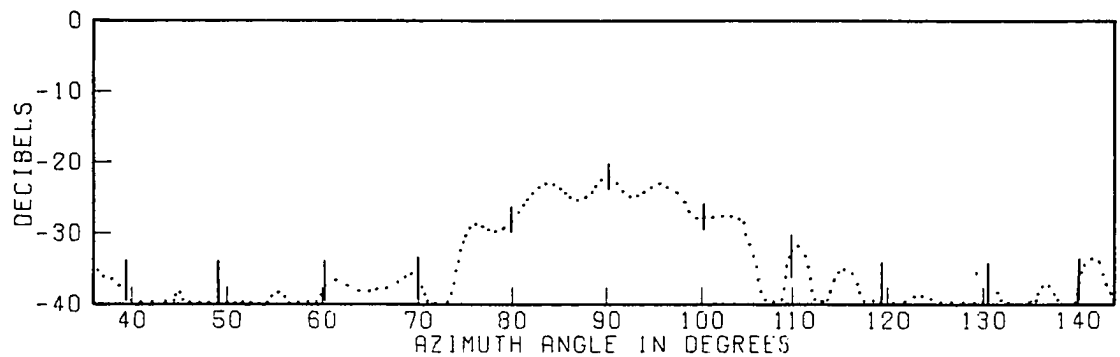

(b) 82 Degree Elevation Angle

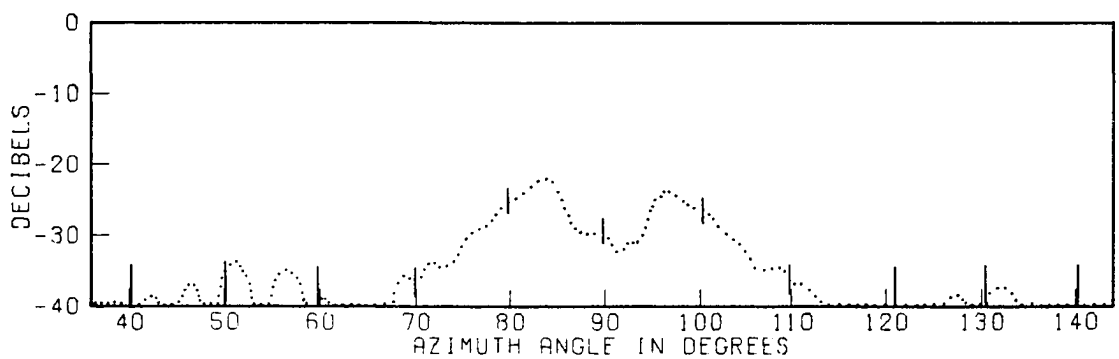

(c) 96 Degree Elevation Angle

Figure 34. Measured Far-field Amplitude Patterns of the Large Test Antenna

Reproduced with permission of the copyright owner. Further reproduction prohibited without permission.

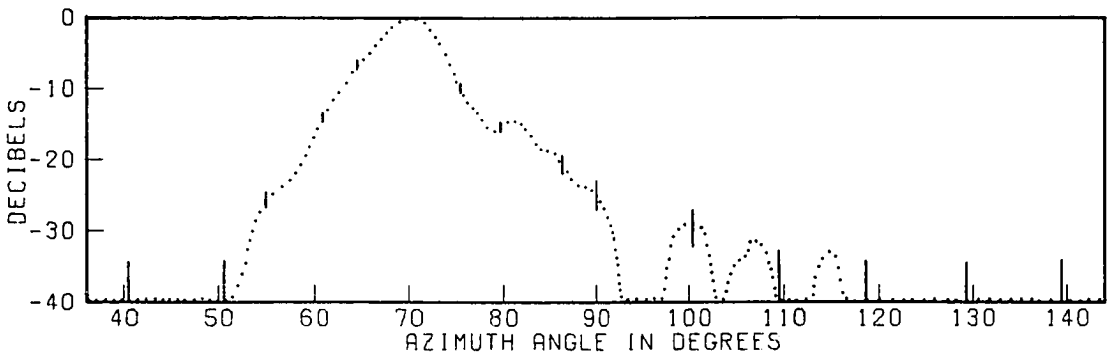

(a) 90 Degree Elevation Angle

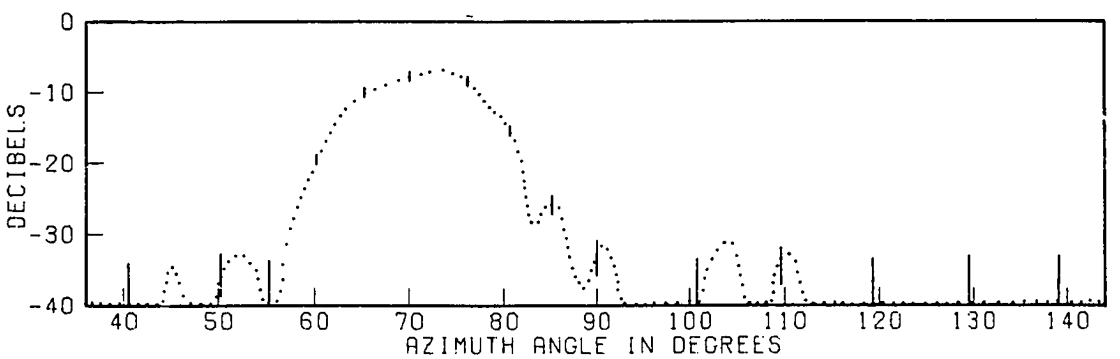

(b) 94 Degree Elevation Angle

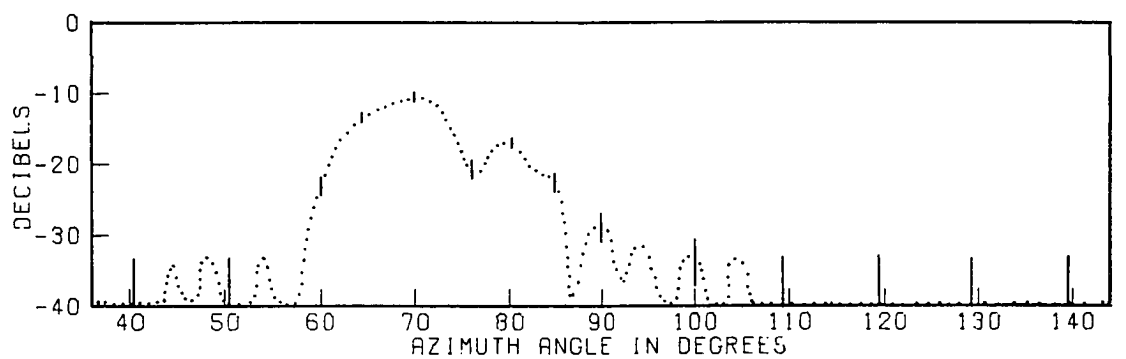

(c) 84 Degree Elevation Angle

Figure 35. Measured Far-field Amplitude Patterns of the Small Test Antenna

Reproduced with permission of the copyright owner. Further reproduction prohibited without permission.

The far-field computation process is shown in the block diagram of Figure 36. The computation process begins by reading into the computer the x-component of the near field of a particular test antenna as measured with a particular near-field probe. Using the read-in z position error table, the x-motion error table and x position voltage, the measured near field is corrected for the z position error of the near-field probe, and sampled every $\lambda/3$ across the 42.3λ measurement area for each x direction traverse of the measuring probe. The resulting corrected x-component of the near field is then stored in a 128 by 128 complex array. Each point in this array represents the amplitude and phase of the x component in the near field, sampled one-third of a wavelength in the x and y directions. Sample spacings larger than one-third of a wavelength may be employed by deleting samples from the original 128 by 128 array.

The sampled, near-field data is next wavenumber-shifted by any pre-selected amount. The wavenumber shifting is carried out in the space domain as a heterodyning operation, as implied by Equation (2-45). The heterodyned data then passes through a simulated Blackman low-pass filter with variable cutoff wavenumbers. The low-pass filtering is performed in the space domain as a two-dimensional convolution of the near-field data with the filter's impulse response, as shown by Equation (2-41). The output of the low-pass filter is re-sampled at a sample spacing corresponding to the cutoff wavenumbers of the low-pass filter.

Next, the minimized data is Fourier transformed with a two-dimensional version of the Fast Fourier transform computation technique. The wavenumber spectrum of the measured near-field data is then corrected for the non-ideal, low-pass characteristics of the Blackman filter, and

Reproduced with permission of the copyright owner. Further reproduction prohibited without permission.

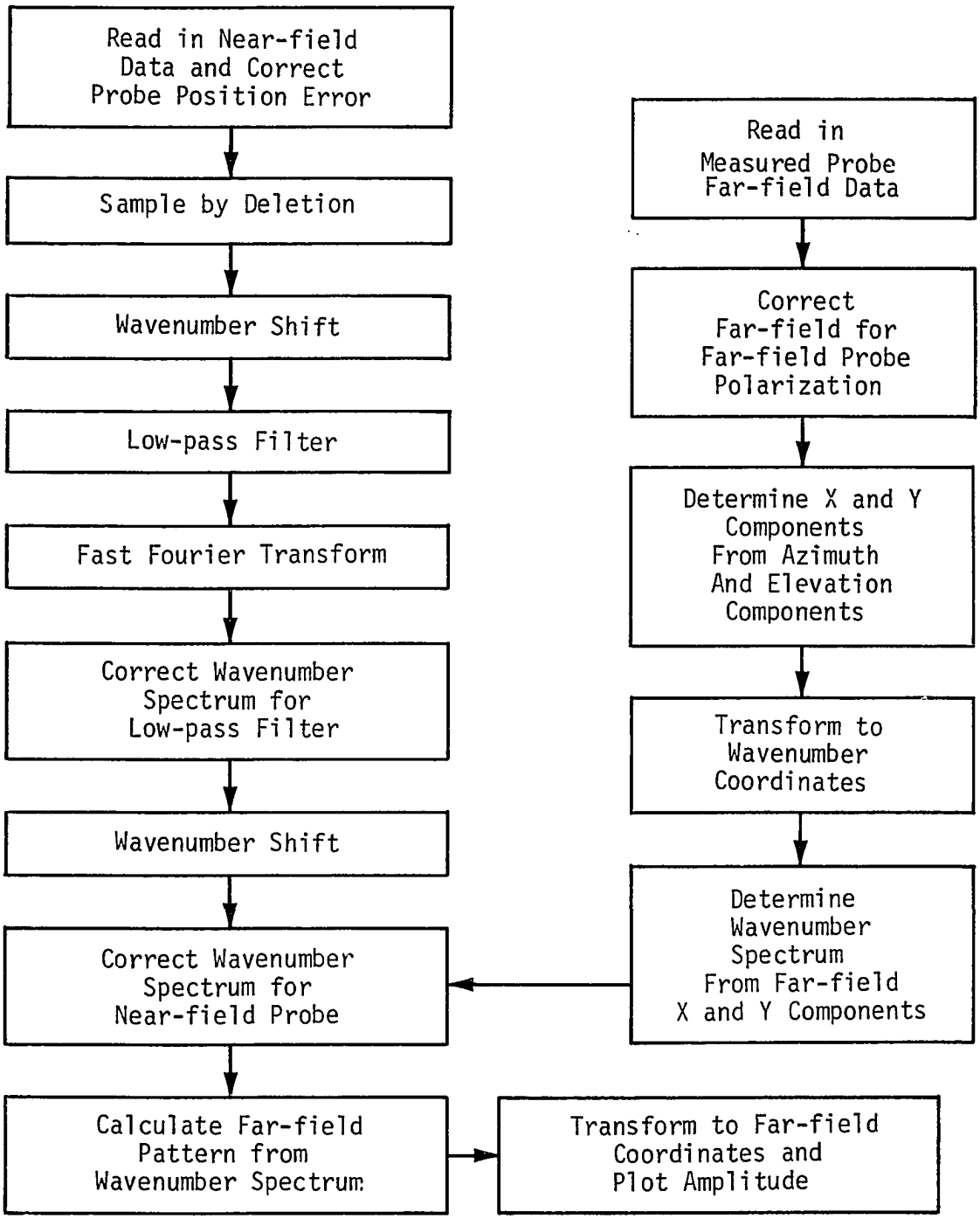

Figure 36. Block Diagram of the Far-field Computation Process

Reproduced with permission of the copyright owner. Further reproduction prohibited without permission.

wavenumber-shifted to correct for the pre-filtering wavenumber shift. Wavenumber shifting in wavenumber space is carried out as a two-dimensional translation of the wavenumber spectrum in wavenumber space.

The filtered wavenumber spectrum of the x component of the measured near field is stored while the same sampling, wavenumber shifting, low-pass filtering, Fast Fourier transforming, filter correcting, and wavenumber shift correcting processes are applied to the y component of the measured near field. With both x and y components of the wavenumber spectrum stored, the far-field patterns of the near-field probe are read into the computer.

The far-field patterns are first corrected for the presence of the far-field probe, as shown in Equations (2-89) and (2-90) using the read-in polarization ratio of the far-field probe. Next, the x and y components of the probe antenna's far-field are calculated from the elevation and azimuth components of the original far-field data, as the radial component of the far field is assumed to be zero. The far-field patterns are transformed from functions of azimuth and elevation to functions of the wavenumbers k_x and k_y, as implied by Equations (2-5) and (2-6). Next, the wavenumber spectrum of the near-field probe, given in Equation (2-12), is obtained from the transverse vector far-field data.

The stored wavenumber spectrum of the x and y components of the measured near field are corrected for the presence of the near-field probe, using the wavenumber spectrum of the probe. The true far-field patterns of the test antenna are then calculated from the true wavenumber spectrum of its near field.

To compare the calculated far-field patterns to those measured on

Reproduced with permission of the copyright owner. Further reproduction prohibited without permission.

the far-field range, the calculated far-field patterns are transformed from wavenumber coordinates to azimuth and elevation coordinates, and selected far-field patterns are plotted on standard size far-field graph paper with a Cal Comp Model 763 numerical drawing machine. Clearly, many parameters of the computation process may be varied.

Figure 37 shows three calculated far-field patterns of the large test antenna. Figure 38 shows three calculated far-field patterns of the small test antenna, each calculated using all 16,384 complex vector near-field samples.

Figure 39(a) shows a large portion of the calculated hemispherical far-field pattern of the large test antenna. The base coordinates in this figure are the wavenumbers k_x and k_y and the ordinate is the power in decibels. Figure 39(b) shows the calculated far-field pattern of the small test antenna.

Figure 40(a) shows a principal plane pattern of the large test antenna calculated from near-field data taken with each of the three near-field probes. Figure 40(b) shows the same principal plane pattern of the large antenna calculated from the same near-field data without correction for the wavenumber spectrum of the probes.

Calculated far-field patterns showing the results of variation in near-field sample spacing, the use of low-pass filtering, and the comparisons to measured far-field patterns are given in Chapter V.

Reproduced with permission of the copyright owner. Further reproduction prohibited without permission.

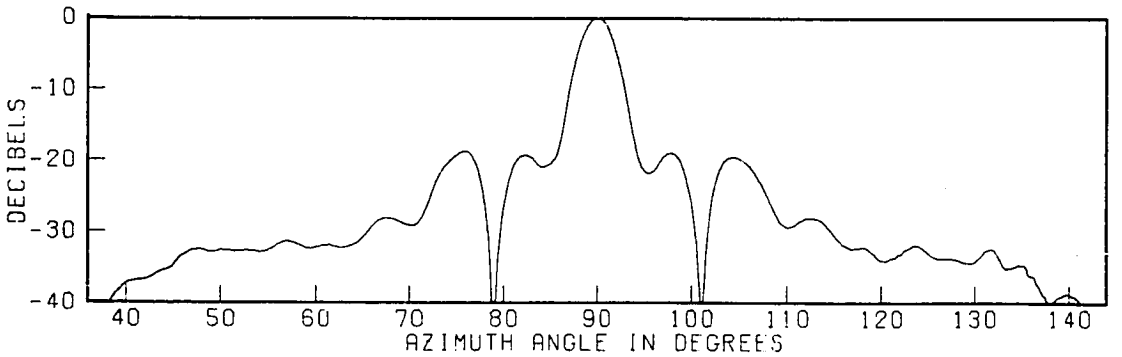

(a) 90 Degree Elevation Angle

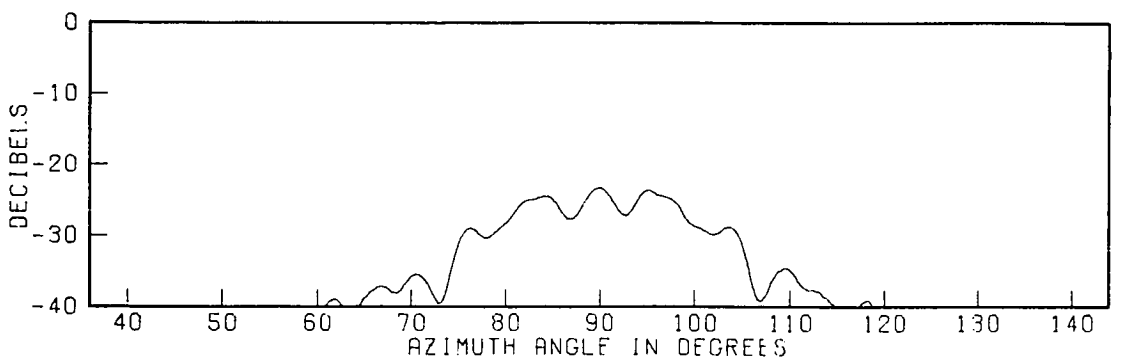

(b) 82 Degree Elevation Angle

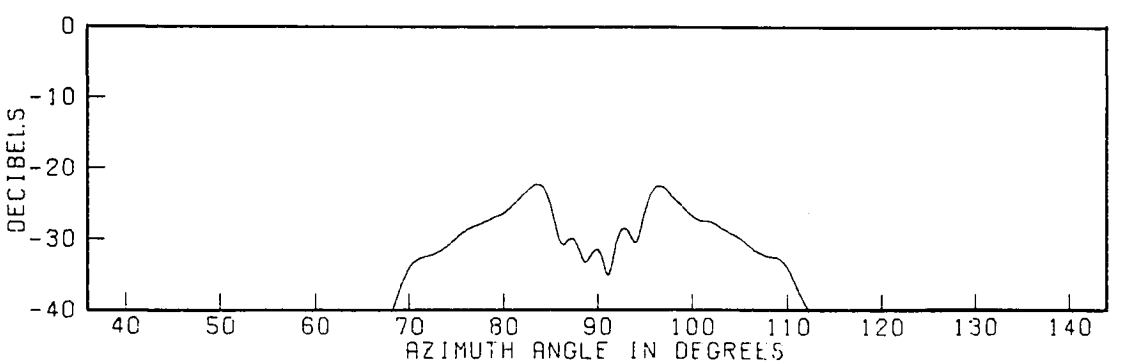

(c) 96 Degree Elevation Angle

Figure 37. Calculated Far-field Amplitude Patterns of the Large Test Antenna

Reproduced with permission of the copyright owner. Further reproduction prohibited without permission.

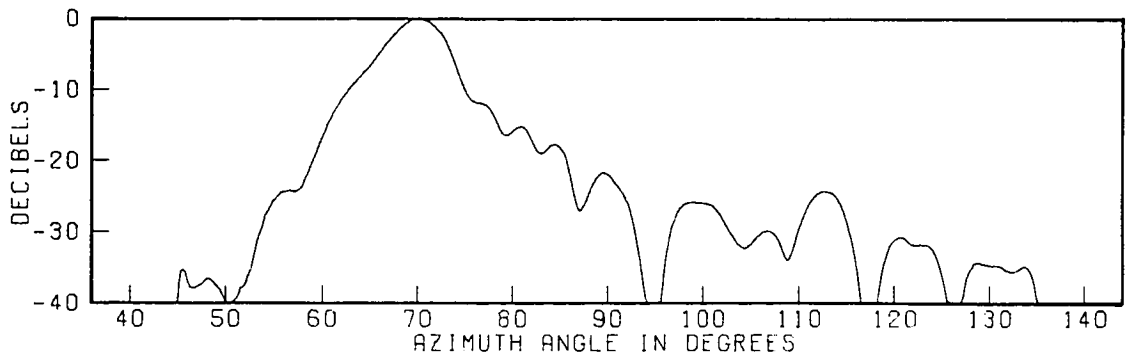

(a) 90 Degree Elevation Angle

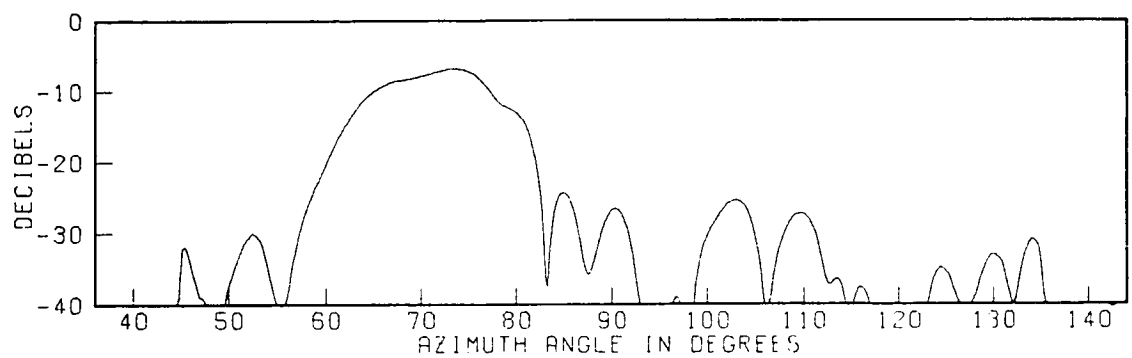

(b) 94 Degree Elevation Angle

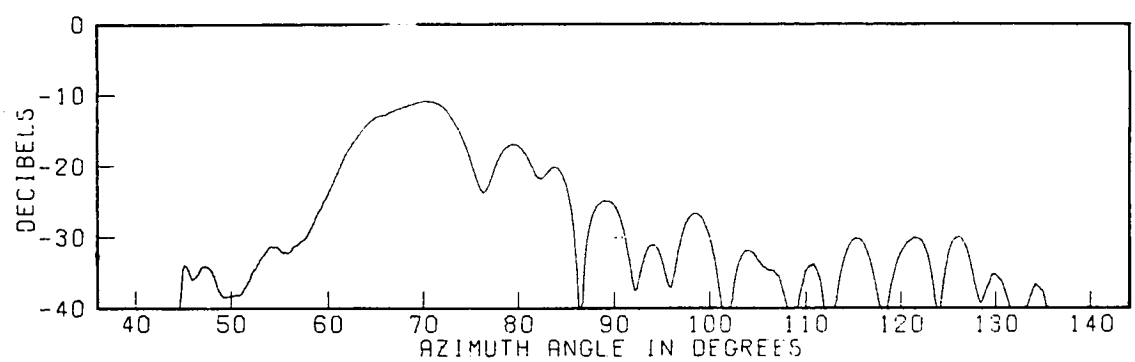

(c) 84 Degree Elevation Angle

Figure 38. Calculated Far-field Amplitude Patterns of the Small Test Antenna

Reproduced with permission of the copyright owner. Further reproduction prohibited without permission.

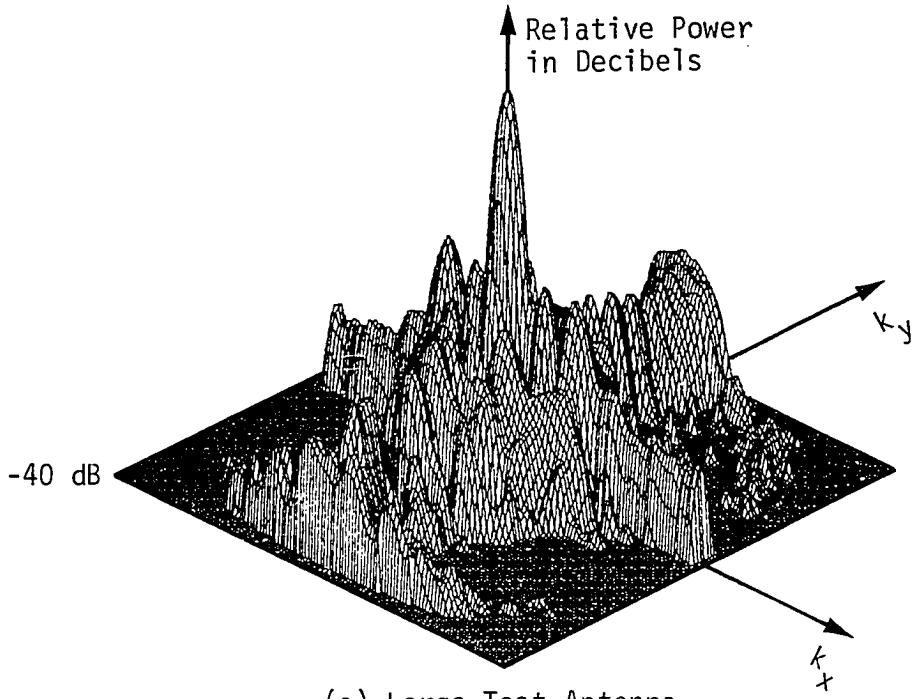

(a) Large Test Antenna

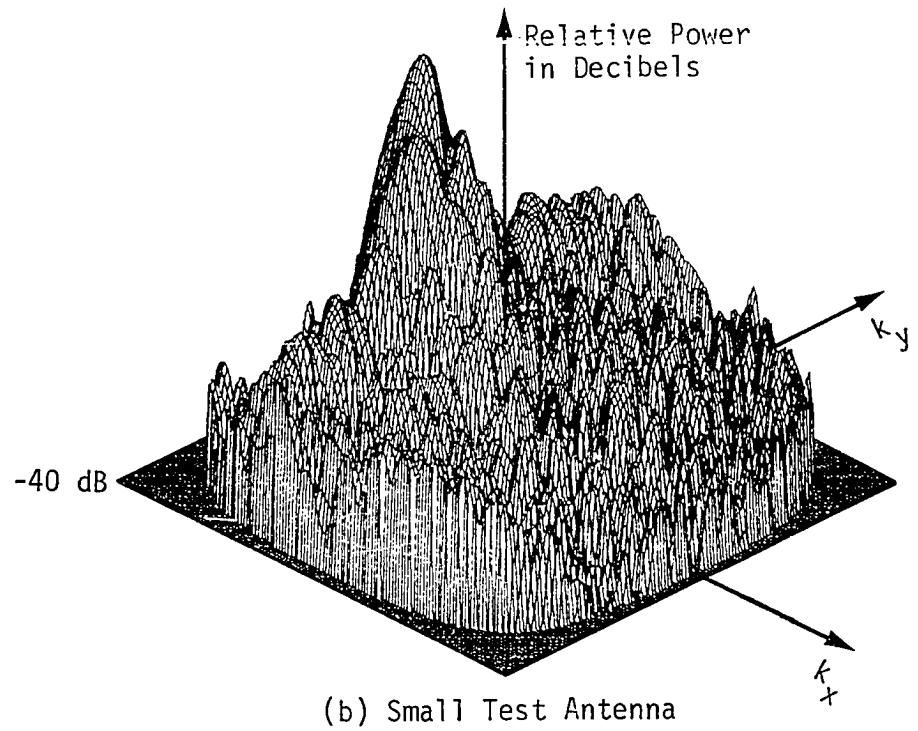

(b) Small Test Antenna

Figure 39. Calculated Two-dimensional Far-field Amplitude Patterns

Reproduced with permission of the copyright owner. Further reproduction prohibited without permission.

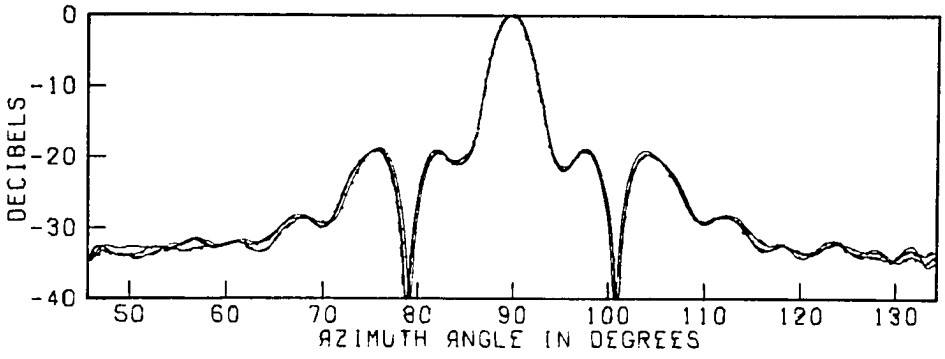

(a) With Probe Correction

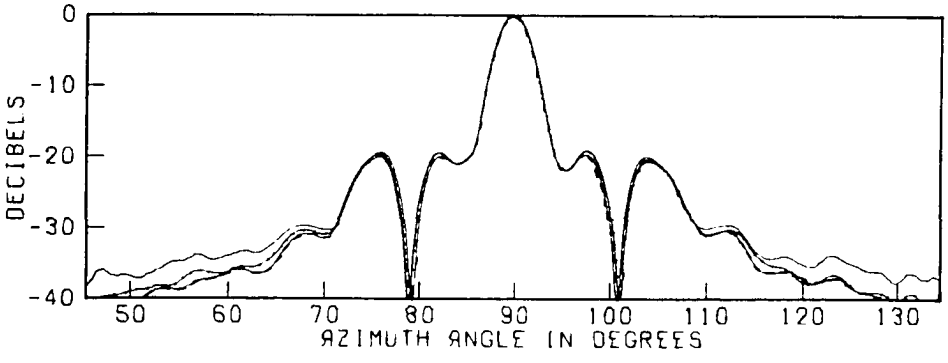

(b) Without Probe Correction

—— Open-ended Waveguide Probe
- - - - Small Horn Probe
— — — Large Horn Probe

Figure 40. Principal Plane Pattern of the Large Test Antenna, Calculated from Near-field Data Taken with Each of the Three Near-field Probes

Reproduced with permission of the copyright owner. Further reproduction prohibited without permission.

CHAPTER V

RESULTS

The results of this dissertation research are threefold.

First, a sample spacing criterion has been established which specifies the required sample spacing for near-field measurements taken on a planar surface. The sample spacing is a function of the distance from the antenna to the measurement plane and the desired level of attenuation of neglected evanescent waves. A sample spacing of $\lambda/3$ in each planar direction was required for the near-field measurements of the two test antennas.

Figure 41 shows the effect of increasing the sample spacings to λ and 2λ for three azimuth slices of the calculated far-field patterns of the large test antenna. Figure 42 shows the effect of increasing the sample spacings to λ and 2λ for three slices of the calculated far-field patterns of the small test antenna.

Second, a near-field data minimization technique was developed which utilizes two-dimensional, low-pass filtering to greatly reduce the amount of near-field data required to calculate small angular sectors of the far field. The amount of post filter data is directly proportional to the angular size of the far-field region to be calculated. The near fields of two test antennas were sampled at $\lambda/3$ spacings over a planar surface with area greater than seven times the aperture area of the antenna resulting in a near-field measurement matrix of $128 \times 128 = 16{,}384$ complex, transverse vector samples.

Reproduced with permission of the copyright owner. Further reproduction prohibited without permission.

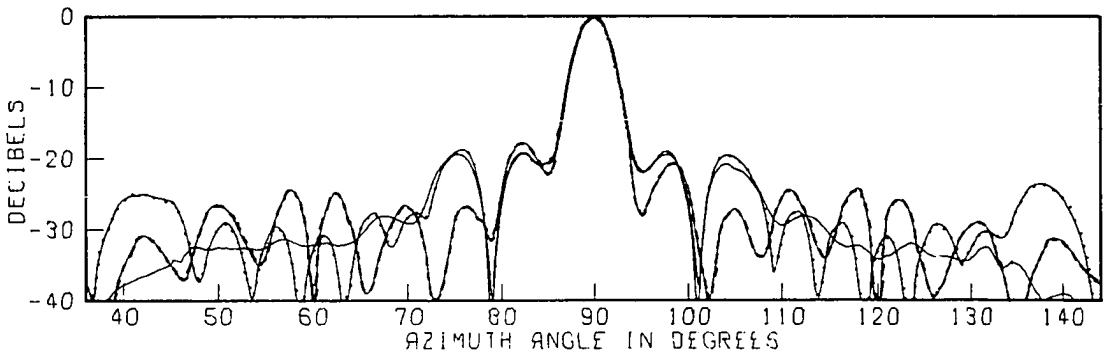

(a) 90 Degree Elevation Angle

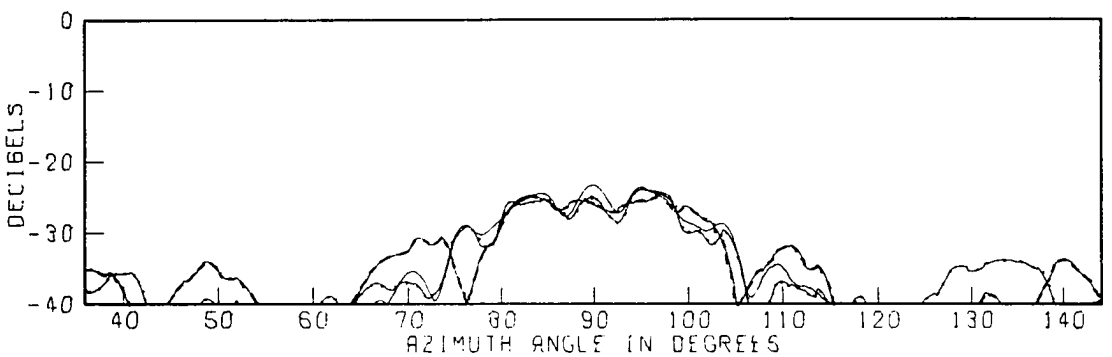

(b) 82 Degree Elevation Angle

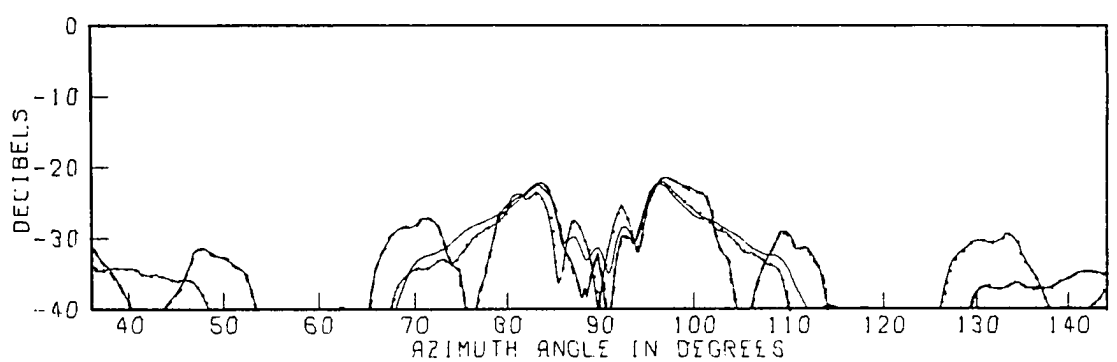

(c) 96 Degree Elevation Angle

—— λ/3 Spacing ---- λ Spacing —·— 2λ Spacing

Figure 41. Calculated Far-field Patterns of the Large Antenna for Near-field Sample Spacings of λ/3, λ, and 2λ

Reproduced with permission of the copyright owner. Further reproduction prohibited without permission.

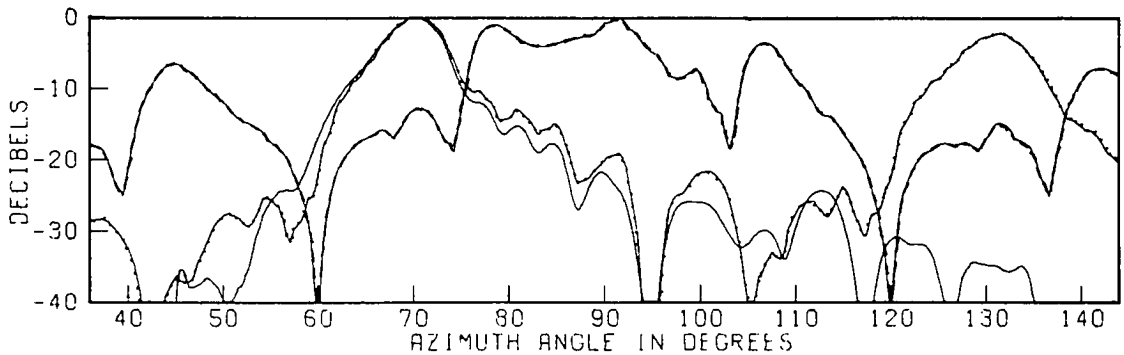

(a) 90 Degree Elevation Angle

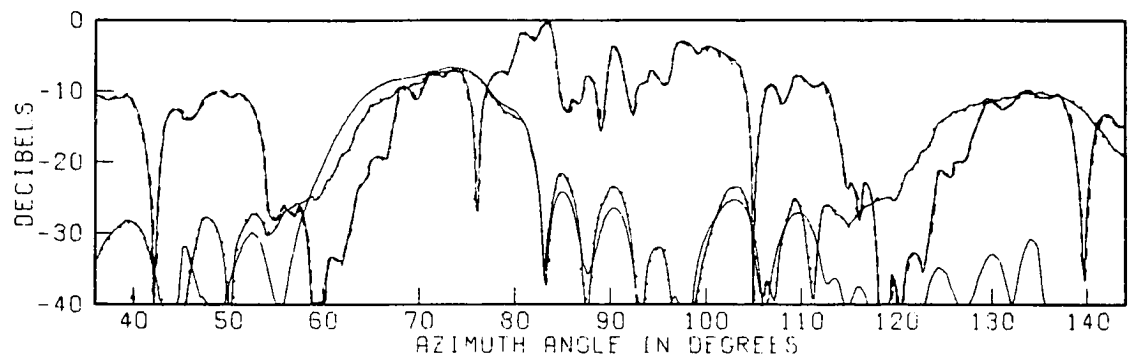

(b) 94 Degree Elevation Angle

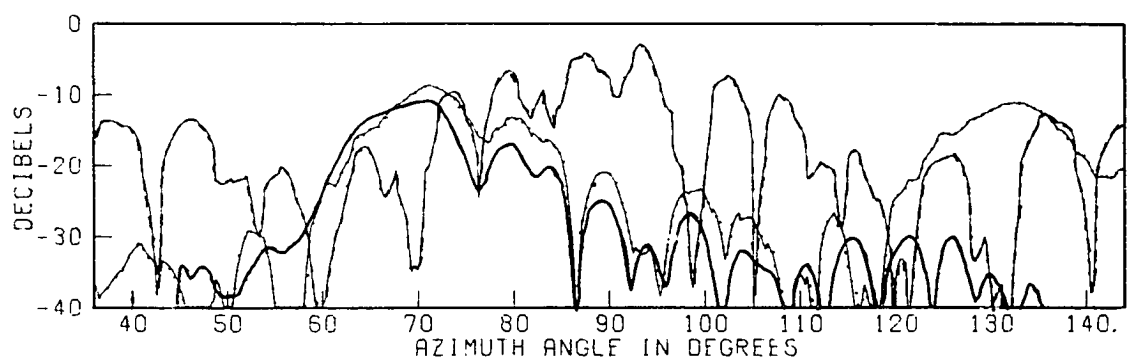

(c) 84 Degree Elevation Angle

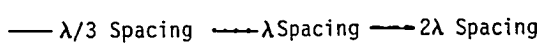

Figure 42. Calculated Far-field Patterns of the Small Antenna for Near-field Sample Spacings of λ/3, λ, and 2λ

Reproduced with permission of the copyright owner. Further reproduction prohibited without permission.

Figure 43 shows three calculated azimuth slices of the far-field pattern of the large test antenna in which all 16,384 near-field samples were used. Superimposed on these patterns are patterns calculated with 60 post-filter samples and 20 post-filter samples. Figure 44 shows similar results for the small test antenna.

Third, this research has demonstrated that it is both feasible and practical to determine far-field patterns of an antenna using the hybrid approach. When near-field data minimization is incorporated in the near-field data collecting process, selected sectors or slices of the far-field pattern of the two test antennas may be determined with a data storage requirement of only 91 (as shown in Figure 10) complex vector samples. The small, post-filter data storage requirement often eliminates the need for a digital computer. From a practical point of view, however, the cost of an adequate, far-field range must be compared, in the final analysis, to the cost of the near-field measuring apparatus and far-field calculation equipment.

Typical slices of the calculated far-field patterns of the large test antenna are compared to the same far-field slices measured on the Georgia Tech antenna range and are shown in Figure 45. A similar comparison for the small test antenna is shown in Figure 46. The calculated and measured patterns are seen to agree to within the measurement accuracy of the far-field range, as determined in Chapter IV.

Although 19 far-field slices of the far-field patterns of each test antenna were measured and calculated, only three have been displayed for the sake of brevity. The omitted far-field slices are in full agreement with the conclusions drawn from the representative far-field slices presented here.

Reproduced with permission of the copyright owner. Further reproduction prohibited without permission.

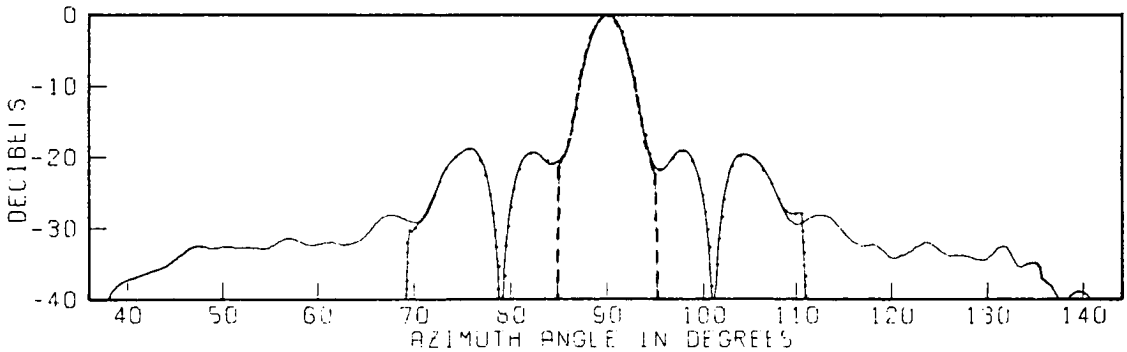

(a) 90 Degree Elevation Angle

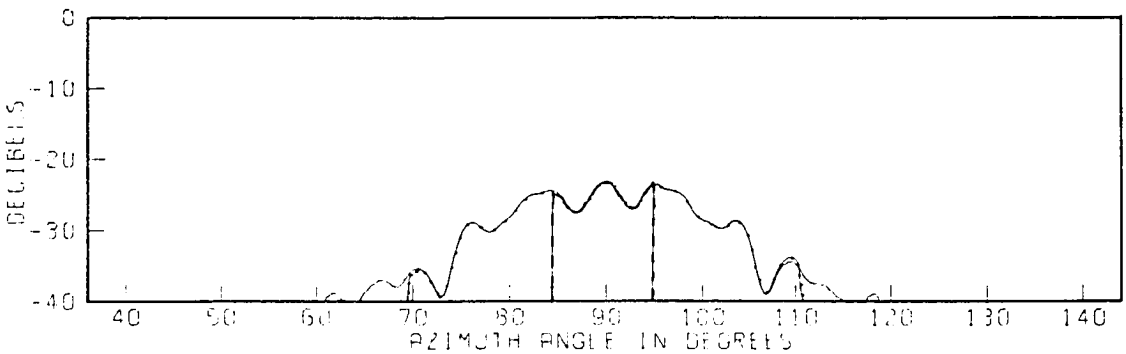

(b) 82 Degree Elevation Angle

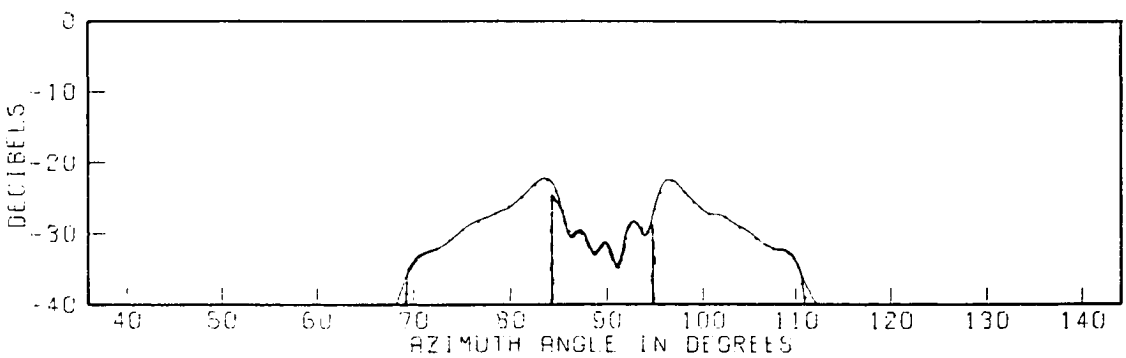

(c) 96 Degree Elevation Angle

——16,384 Samples - - - 60 Samples —— 20 Samples

Figure 43. Far-field Patterns of the Large Test Antenna Calculated with 16384, 60, and 20 Post-filter Samples

Reproduced with permission of the copyright owner. Further reproduction prohibited without permission.

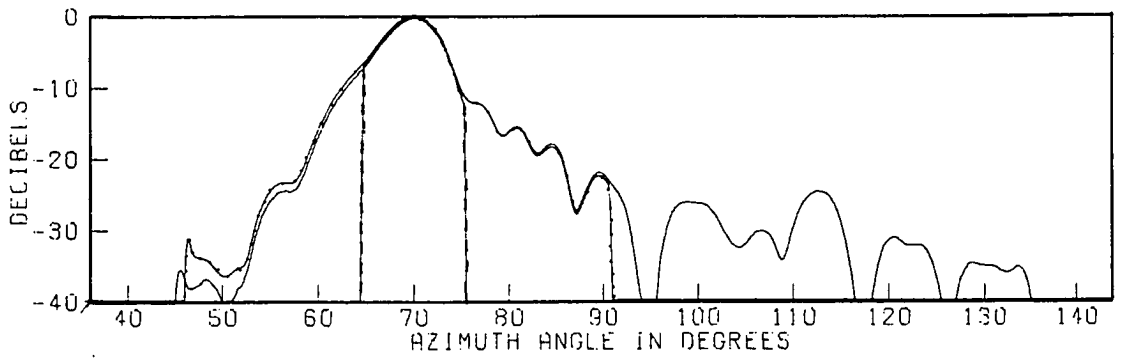

(a) 90 Degree Elevation Angle

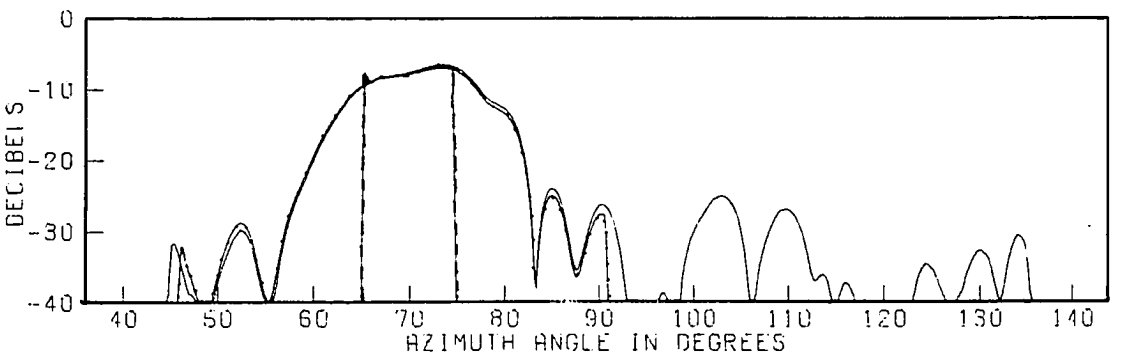

(b) 94 Degree Elevation Angle

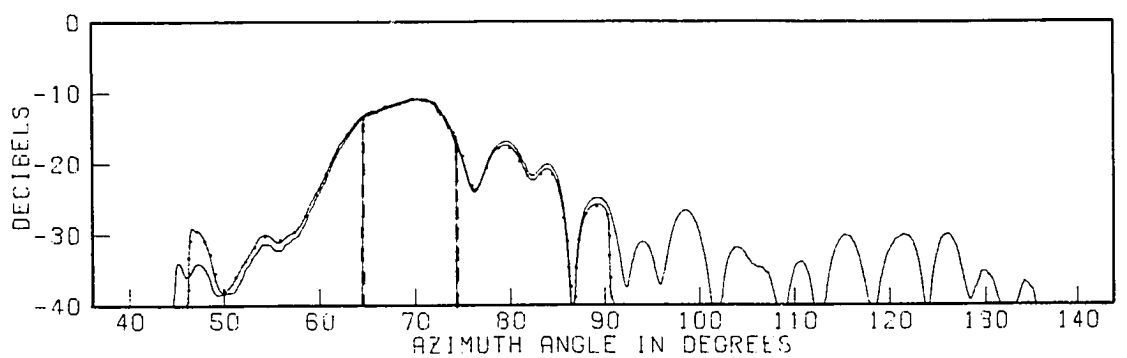

(c) 84 Degree Elevation Angle

——16,384 Samples - - - 60 Samples — — 20 Samples

Figure 44. Far-field Patterns of the Small Test Antenna Calculated with 16384, 60, and 20 Post-filter Samples

Reproduced with permission of the copyright owner. Further reproduction prohibited without permission.

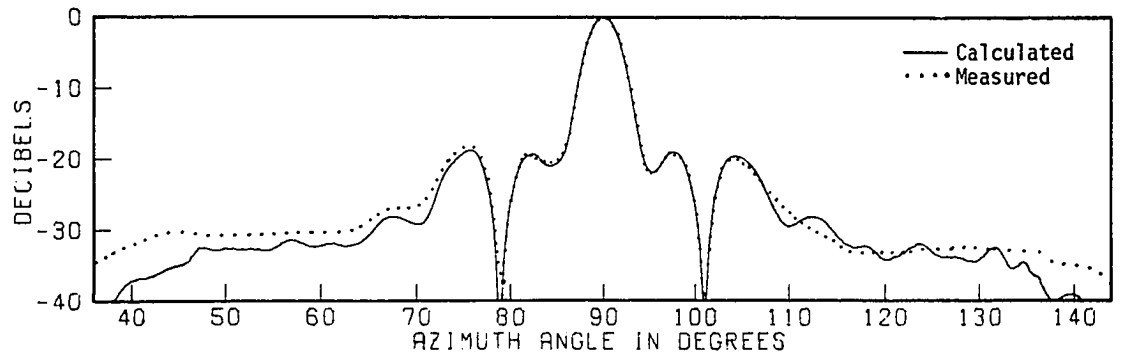

(a) 90 Degree Elevation Angle

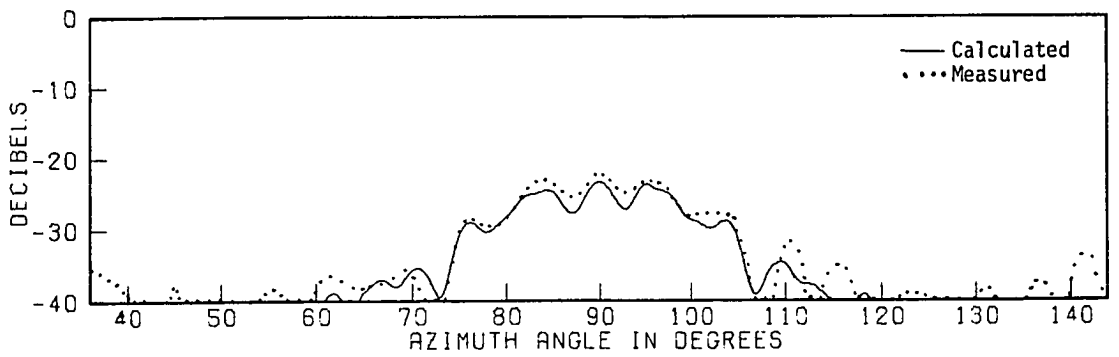

(b) 82 Degree Elevation Angle

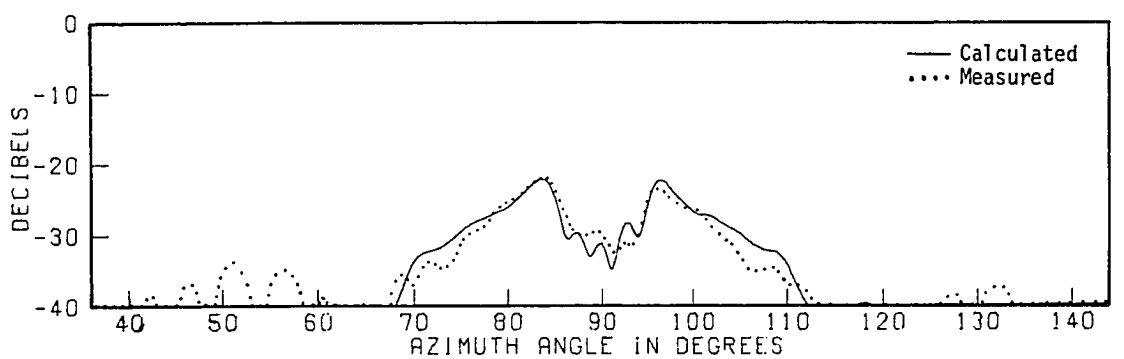

(c) 96 Degree Elevation Angle

Figure 45. Comparison of Calculated and Measured Far-field Patterns of the Large Test Antenna

Reproduced with permission of the copyright owner. Further reproduction prohibited without permission.

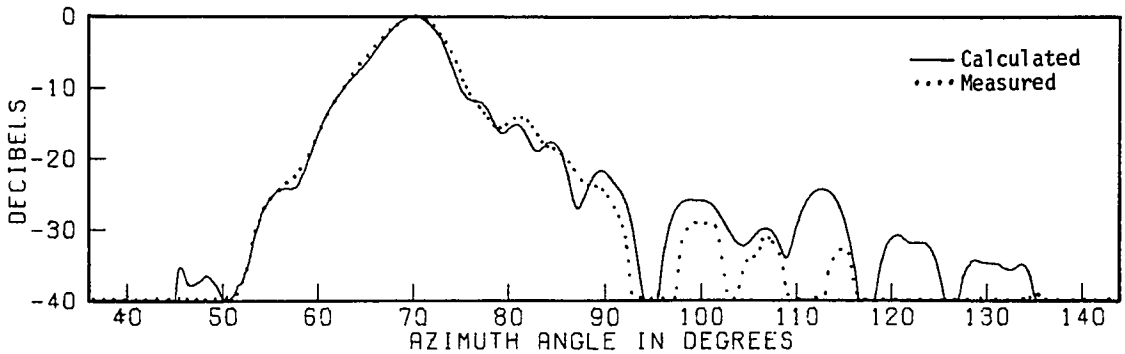

(a) 90 Degree Elevation Angle

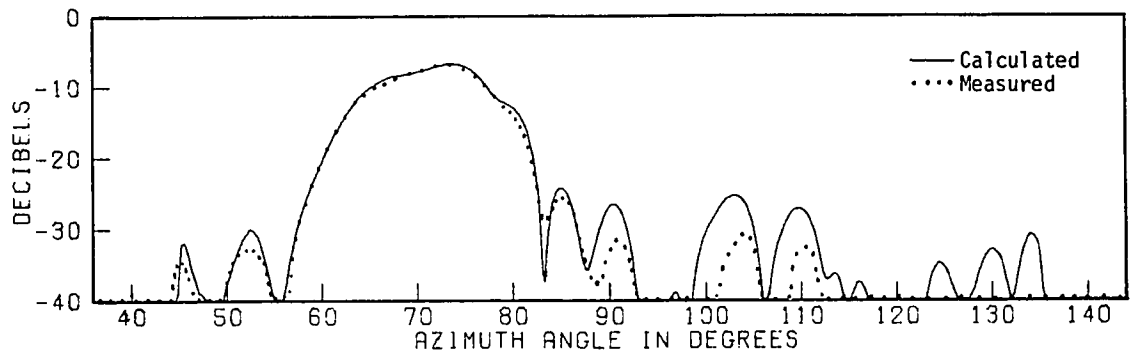

(b) 94 Degree Elevation Angle

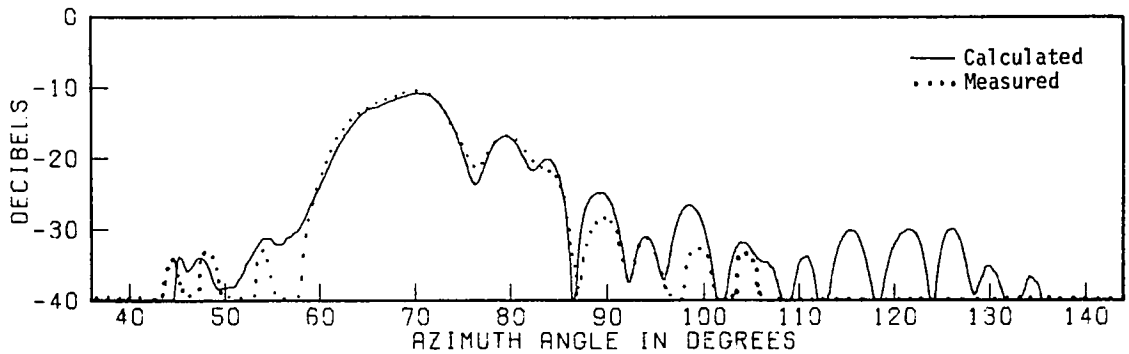

(c) 84 Degree Elevation Angle

Figure 46. Comparison of Calculated and Measured Far-field Patterns of the Small Test Antenna

Reproduced with permission of the copyright owner. Further reproduction prohibited without permission.

CHAPTER VI

CONCLUSIONS AND RECOMMENDATIONS

It is concluded that:

(1) The near-field sample spacing criterion developed in this research makes it possible to accurately determine the far-field pattern of an arbitrary antenna from measured data taken at preselected points on a planar surface in the near-field of the antenna. Also, a priori information concerning the "Q", direction of propagation and beam width of single beam antennas, can be used to increase the sample spacings.

(2) The near-field data minimization technique developed in this research can be used to greatly reduce the amount of near-field data required to calculate angular sectors of the far-field pattern of an arbitrary antenna. Principal plane patterns are typical of one-dimensional far-field patterns for which great reductions in the amount of near-field data are possible.

(3) The hybrid approach to far-field determination is feasible, accurate, and, for electrically large antennas, practical.

It is recommended that three areas of research be undertaken to further advance the hybrid approach to far-field determination.

(1) Determination of the required near-field measurement accuracy to accurately calculate the far-field pattern of an arbitrary antenna.

(2) Examination of the effect of multiple reflections between the near-field probe and the test antenna on the calculated far-field pattern.

Reproduced with permission of the copyright owner. Further reproduction prohibited without permission.

(3) Extension of this research to non-planar near-field measurement surfaces.

It is recommended that near-field measurement and scattering matrix theory be used to analyze other electromagnetic field problems such as:

(1) Determination of the scattering properties of passive devices, such as radomes, dielectric coverings, and antenna support structures.

(2) Calculation of the far-field pattern of an arbitrary antenna enclosed in an arbitrary radome, when both the wavenumber spectrum of the antenna and scattering parameters of the radome are known a priori.

(3) Synthesis of array antennas with arbitrary array elements whose wavenumber spectra are known a priori.

Reproduced with permission of the copyright owner. Further reproduction prohibited without permission.

BIBLIOGRAPHY

1. J. D. Dyson, "Antenna Near-field Measurements," pp. 57-114, of P. E. Mayes' book, Electromagnetics and Antennas, University of Illinois, Urbana, Illinois, 1967.

2. IEEE Test Procedure of Antennas, No. 149 (Revision of 48 IRE 252) January, 1965, IEEE Transactions on Antennas and Propagation, Vol. AP-13, No. 3, pp. 437-466, May, 1965.

3. J. T. Kenneday and J. W. Rosson, "The Use of Solar Radio Emission for the Measurement of Radar Angle Errors," The Bell System Technical Journal, 1799-1812, November, 1962.

4. H. Brueckmann, "Antenna Pattern Measurement by Satellite," IEEE Transactions on Antennas and Propagation, Vol. AP-11, pp. 143-147, March, 1963.

5. J. P. Shanklin, "Pattern Measurements of Large Fixed Antennas," IRE Transactions on Instrumentation, Vol. I-4, pp. 16-22, October, 1965.

6. S. Silver, Microwave Antenna Theory and Design, McGraw-Hill Book Company, New York, Chapters 5 and 6, 1949.

7. N. J. Gamara, "Pattern Predictability on the Basis of Aperture Phase and Amplitude Distribution Measurements," Tech. Rep. EDL-M247, Contract DA 36-039 SC-S5402, (DDC No. AD-236298) Electronic Defense Lab., Mountain View, California, March 25, 1960.

8. M. Hu, "Study of Near-zone Fields of Large Aperture Antennas," Final Report on Contract No. AF 30(602)-928, Syracuse University Research Institute, April, 1957.

9. D. T. Paris, "Digital Computer Analysis of Aperture Antennas," IEEE Transactions on Antennas and Propagation, Vol. AP-16, No. 2, pp. 262-264, March, 1968.

10. J. H. Richmond and T. E. Tice, "Probes for Near-field Measurements," IRE Transactions on Microwave Theory and Propagation, Vol. 3, No. 3, pp. 32-34, April, 1955.

11. H. Whiteside and R. W. P. King, "The Loop Antenna as a Probe," IEEE Transactions on Antennas and Propagation, Vol. AP-12, No. 3, pp. 291-297, May, 1964.

12. G. A. Woonton, "The Probe Antenna and the Diffraction Field," Technical Report 17, Eaton Elec. Res. Lab., McGill University, July, 1952.

Reproduced with permission of the copyright owner. Further reproduction prohibited without permission.

BIBLIOGRAPHY (Continued)

13. R. B. Borts and G. A. Woonton, "The Effect of the Directivity of the Probe Upon the Measurement of Aperture Fields," Technical Report 21, (DDC No. AD 28506) Eaton Elect. Res. Lab., McGill University, July, 1952.

14. R. Justice and V. H. Rumsey, "Measurement of Electric Field Distribution," IRE Transactions on Antennas and Propagation, Vol. AP-3, No. 4, pp. 177-180, October, 1955.

15. R. F. Harrington, "Small Resonant Scatterers and Their Uses for Field Measurements," IRE Transactions on Microwave Theory and Techniques, Vol. MTT-10, No. 3, pp. 166-174, May, 1962.

16. R. Plonsey, "Surface Current Measurements with an Electric Probe," IRE Transactions on Microwave Theory and Techniques, Vol. MTT-10, No. 3, pp. 214-217, May 1962.

17. H. G. Booker and P. C. Clemmow, "The Concept of an Angular Spectrum of Plane Waves, and its Relation to that of Polar Diagram and Aperture Distribution," Proceedings IEE, Vol. 97, Part 3, pp. 11-17, January, 1950.

18. P. C. Clemmow, The Plane Wave Spectrum Representation of Electromagnetic Fields, Pergamon Press, Ltd., London, 1966.

19. J. Brown, "A Theoretical Analysis of Some Erros in Aerial Measurements," Proceedings IEE, Vol. 105, Part C, pp. 343-351, February, 1959.

20. E. V. Jull, "An Investigation of Near-field Radiation Patterns Measured with Large Antennas," IRE Transactions on Antennas and Propagation, Vol. AP-10, No. 4, pp. 363-369, July, 1962.

21. E. V. Jull, "The Estimation of Aerial Radiation Patterns from Limited Near-field Measurements," Proceedings IEE, Vol. 110, No. 3, pp. 501-506, March, 1963.

22. J. Brown and E. V. Jull, "The Prediction of Aerial Radiation Patterns from Near-field Measurements," Proceedings IEE, Vol. 105, Part B, No. 42, pp. 635-644, November, 1961.

23. D. M. Kerns, "Antenna Measurements with Arbitrary Measuring Antennas at Arbitrary Distances," High Frequency and Microwave Field Strength Precision Measurements Seminar, National Bureau of Standards, Boulder, Colorado, Session 3, Lecture 1, 1966.

24. D. M. Kerns and E. S. Dayhoff, "Theory of Diffraction in Microwave Interferometry," Journal of Research of the National Bureau of Standards - B. Mathematics and Mathematical Physics, Vol. 64B, No. 1, January-March, 1960.

Reproduced with permission of the copyright owner. Further reproduction prohibited without permission.

BIBLIOGRAPHY (Continued)

25. J. A. Stratton, Electromagnetic Theory, John Wiley and Sons, Inc., New York, pp. 361-369, 1962.

26. B. Gold and C. M. Rader, Digital Processing of Signals, McGraw-Hill Book Company, Inc., New York, 1969.

27. A. Papoulis, The Fourier Integral and its Applications, McGraw-Hill Book Company, Inc., New York, 1962.

28. A. Papoulis, Systems and Transforms with Applications in Optics, McGraw-Hill Book Company, Inc., New York, 1968.

29. D. P. Petersen and D. Middleton, "Sampling and Reconstruction of Wavenumber-limited Functions in N-dimensional Euclidean Spaces," Information and Control, Vol. 5, pp. 279-323, 1962.

30. G. Borgiotti, "A General Way of Representing the Electromagnetic Field," Alta Frequenza, Vol. 31, No. 5, pp. 285-293, March, 1962.

31. G. Borgiotti, "Fourier Transform Methods in Aperture Antenna Problems," Alta Frequenza, Vol. 32, No. 11, pp. 811-816, November, 1963.

32. D. R. Rhodes, "On a Fundamental Principle in the Theory of Planar Apertures," Proceedings IEEE, Vol. 52, pp. 1013-1021, September 1964.

33. R. B. Blackman and J. W. Tukey, The Measurement of Power Spectra, Dover Publications, Inc., New York, 1958.

34. J. S. Hollis, T. J. Lyon, and L. Clayton, Jr., Microwave Antenna Measurements, Scientific Atlanta, Inc., Atlanta, Georgia, 1970.

Reproduced with permission of the copyright owner. Further reproduction prohibited without permission.

VITA

Edward Bennett Joy was born in Troy, New York, on November 15, 1941. He is the son of Herman Johnston Joy and Elizabeth Bennett Joy. He was married to Patricia Huddleston of Jacksonville, Florida, on August 27, 1966.

He attended elementary schools in Hoosick Falls, New York, and Athens, Georgia, and graduated from Athens High School in June, 1959. In September of 1959, he entered the Georgia Institute of Technology and in June of 1963, received a Bachelor of Electrical Engineering and a commission as Ensign in the United States Navy. He was elected to membership in Eta Kappa Nu and Pi Delta Epsilon and was selected to appear in Who's Who Among Students in American Colleges and Universities, 1963-64.

From July, 1963, to July, 1965, he served as an engineering officer aboard the aircraft carrier U.S.S. HANCOCK CVA-19, home-ported in San Francisco, California.

In September, 1965, he entered the Graduate Division of the Georgia Institute of Technology and in June, 1967, received an M.S.E.E. Degree.

He held summer jobs at Advanced Research, Inc., Atlanta, Georgia, and at Jacksonville Shipyards, Inc., Jacksonville, Florida, in 1965 and 1966, respectively.

He held a Schlumberger Fellowship from September, 1966, to September, 1967, a NASA Traineeship from September, 1967, to June, 1967, and a Scientific Atlanta, Inc. research grant from June, 1967, to

Reproduced with permission of the copyright owner. Further reproduction prohibited without permission.

September, 1970. He also held a Graduate Teaching Assistantship from September, 1967, to September, 1970.

Reproduced with permission of the copyright owner. Further reproduction prohibited without permission.